5-3-2018

A New Graphene Quantum Dot Sensor for Estimating an Antibiotic Concentration

Nuzhet Nihaar Nasir Ahamed
nn5878@rit.edu

R.I.T.

A New Graphene Quantum Dot Sensor for Estimating an Antibiotic Concentration

by

Nuzhet Nihaar Nasir Ahamed

A Thesis Submitted in Partial Fulfillment of the
Requirements for the Degree of

Master of Science

in

Materials Science and Engineering.

School of Chemistry and Materials Science
College of Science
Rochester Institute of Technology
Rochester, NY

May 3rd 2018

School of Chemistry and Materials Science
College of Science
Rochester Institute of Technology
Rochester, New York

CERTIFICATE OF APPROVAL

The M.S. degree thesis of Nuzhet Nihaar Nasir Ahamed has been examined and approved by the thesis committee as satisfactory for the thesis required for the M.S. degree in Materials Science and Engineering.

Dr. K.S.V Santhanam Date
Professor, School of Chemistry and Materials Science. ***(Advisor)***

Dr. Gerald Takacs Date
Professor, School of Chemistry and Materials Science.

Dr. Massoud Miri Date
Associate Professor, School of Chemistry and Materials Science.

Dr. Michael S Pierce ***(MSE Graduate Program Director)*** Date
Associate Professor of Physics, School of Physics and Astronomy.

ABSTRACT

The antibiotics have impacted the human ailments by curtailing the growth of microbes and by providing relief from microbial diseases. While there are a large number of analytical methods available for the determination of antibiotics concentration, they are time consuming and impractical for usage in the fields. This thesis is aimed at overcoming the deficiencies of those methods in developing a new sensor. It reports a study of graphene quantum dots (GQD) bound ferric ion for sensing an antibiotic, ciprofloxacin (CP). The interaction of ferric ion with CP was used as a probe for the analytical estimation of CP using differential pulse voltammetry (DPV). A solution containing ferric ion exhibits a well-defined cathodic peak at E_{pc}=0.310 V vs saturated calomel electrode (SCE) with a peak width of 0.100V. When nanomolar to micromolar concentration of CP is present in the solution, along with ferric ion, three new peaks at E_{pc}^{I}=0.200V, E_{pc}^{II}=0.050 V and E_{pc}^{III}=-0.085V are observed due to the binding of CP to ferric ion. The decrease in peak current of E_{pc} at 0.310 V is proportional to the concentration of CP in the solution. The peak current at 0.200 V shows an increase corresponding to the CP concentration in solution. These results paved the way for examining the prospectus for developing a portable resistive sensor using interdigitated gold electrodes on alumina substrate. The principle of this sensor is based on that ferric ion bound to GQD will have a finite resistance and when it is bound to CP the resistance will increase as the charge transport faces a barrier due to bulky CP molecules. With a view to establish that ferric ion is binding to GQD, fluorescence of GQD has been recorded with ferric ion in solution.

The approach adopted in developing resistive sensor is shown below.

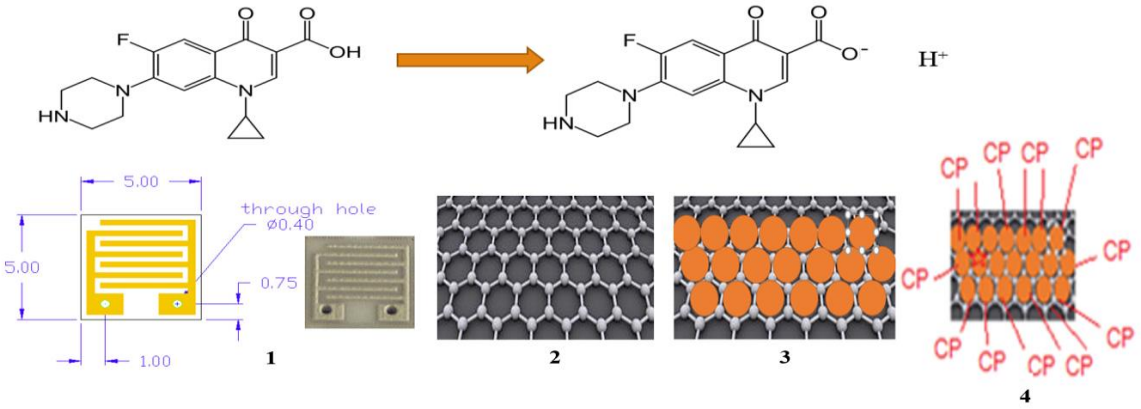

CP (μM)	1.31	3.62	7.34	14.68	29.36
ΔR/Ri (no units)	1.6	2.62	2.85	3.08	3.19

Approach towards making the sensor

The numbers in the above picture denotes

1. Interdigitated gold electrodes

2. GQD bound interdigitated gold electrodes

3. Ferric ion bound to GQD

4. Attachment of CP to ferric ion.

The sensor response is found to be dependent on the activity of the availability of ferric ion on GQD resulting in the usage of it as a disposable sensor. The interference of urea in the measurement of CP was examined for the practical usage of it in urine analysis.

ACKNOWLEDGEMENTS

Foremost, I would like to express my sincere gratitude to my advisor, Dr. K.S.V Santhanam, for his continuous support, patience, motivation, and guidance. As my teacher and mentor, he has extensively taught me more than I could ever give him credit for here. The door to his office was always open whenever I ran into a trouble spot or had a question about my research or writing. He has shown me, by his example, what a good scientist (and person) should be. I will be always grateful to him for steering me in the right direction towards becoming a better researcher.

I am also indebted to my thesis committee members, Dr. Gerald Takacs and Dr. Massoud Miri for their passionate participation, valuable suggestions and feedback for my master's research. This work would not have been complete without their sound advice.

I genuinely thank all my teachers, Dr. Nathan Eddingsaas, Dr. Karl Hirschman and Dr. Santosh Kurinec for their teachings which helped me immensely during research work. Many thanks to Mrs. Komalavalli Santhanam for donating ciprofloxacin drug for our initial studies. I am thankful to Dr. Michael Schrlau for the CNT pipette electrodes which were used in the study. I also thank Mr. Michael Cross, Mr. Tom Allston, Miss. Autumn Madden for their constant help and support.

I am grateful to Dr. Paul Craig, Dr. Michael S Pierce and Dr. Casey Miller for the opportunity to study Materials Science and Engineering at School of Chemistry and Materials Science, RIT. I am thankful for the financial support of the National Science Foundation (NSF), without which this work would not have been possible.

Special thanks to my roommate, Anjali Jogeshwar for keeping me happily positive, sane and well-fed during the course of my master's study. I also thank my friends Kris Wong, Wenxuan Fan, David Hurley, Martin Dann and Logan Robart for the stimulating discussions and all the fun during classes and in the lab.

Last but not the least, I would like to express my gratitude to my family and friends back in India. My heartfelt thanks to my parents, whose blessing and guidance are with me in whatever I pursue. Let alone this thesis, my coming to RIT would not have been possible without their love and support. Thanks for all your encouragement!

PUBLICATION

N.N.N. Ahamed, W. Fan, M. Schrlau and K.S.V. Santhanam, A New Graphene Quantum Dot Sensor for Estimating an Antibiotic Concentration, *MRS Advances Nanomaterials*, 3 (15), 825 **(2018)**, DOI:10.1557/adv.2018.29.

PRESENTATIONS

Interdigitated Gold Electrodes Coated with Graphene Quantum Dots For Sensing Ciprofloxacin Antibiotic, N.N.N. Ahamed, W. Fan, M. Schrlau and K.S.V. Santhanam, 44th Annual Fall Scientific Paper Session, Rochester Academy of Science, October 2017.

A New Graphene Quantum Dot Sensor for Estimating an Antibiotic Concentration, N.N.N. Ahamed, W. Fan, M. Schrlau and K.S.V. Santhanam, RIT-Graduate Showcase, November 3rd, 2017.

Interdigitated Gold electrodes with Graphene Quantum Dot Platform For Ciprofloxacin Sensor, N.N.N. Ahamed, W. Fan, M. Schrlau and K.S.V. Santhanam, 41st IEEE EDS Activities in Western New York Conference, November 10th, 2017.

A New Graphene Quantum Dot Sensor for Estimating Antibiotic Concentration, N.N.N. Ahamed, W. Fan, M. Schrlau and K.S.V. Santhanam, Materials Research Society (MRS) Fall 2017 Conference in Boston, November 28th, 2017.

TABLE OF CONTENTS

LIST OF ABBREVIATIONS

2D	Two-dimensional
3D	Three-dimensional
BDD	Boron doped diamond
BiOBr	Bismuth oxybromide
CB	Conduction band
CE	Counter electrode
CL	Chemiluminescent or chemiluminescence
CNT	Carbon nanotubes
CP	Ciprofloxacin
CPS	Counts per second
CV	Cyclic Voltammetry
DPV	Differential Pulse Voltammetry
ECL	Electro-chemiluminescent or Electro-chemiluminescence
EG	Ethylene glycol
ELISA	Enzyme-Linked Immunosorbent Assay
FTIR	Fourier transform infra-red
GC	Glassy carbon
GCE	Glassy Carbon Electrode
GQD	Graphene Quantum Dots
HCT	Hydrochlorothiazide
HILIC – MS	Hydrophilic Interaction Liquid Chromatography – Tandem Mass Spectrometry
HPLC	High-Performance Liquid Chromatography
IPA	Isopropyl alcohol
ITO	Indium tin oxide
ITP-CZE	Isotachophoresis–Capillary Zone Electrophoresis
IUPAC	International Union of Pure and Applied Chemistry
LCMS	Liquid Chromatography−Mass Spectroscopy
MWCNT	Multi-walled carbon nanotubes
MWCNT/GCE	Multi-walled carbon nanotubes film-modified glassy carbon electrode

NBIL	Nano Bio-Interface Laboratory
NMR	Nuclear Magnetic Resonance
PAP	Para-amino-phenol
PAR/EGR	Poly(alizarin red)/electrodeposited graphene
PL	Photo-luminescent or Photoluminescence
QD	Quantum Dots
QHE	Quantum Hall Effect
REF	Reference electrode
R_f	Resistance of the sensor after exposure to CP or Argon or Oxygen
R_i	Resistance of the sensor before exposure to CP or Argon or Oxygen
SCE	Standard Calomel electrode
SEM	Scanning Electron Microscopy
SET	Single Electron Transistor
SiC	Silicon carbide
SPE	Screen Printed electrode
TEM	Transmission Electron Microscopy
UV	Ultra-Violet
VB	Valence band
WE	Working electrode
WHO	World health organization

LIST OF FIGURES

LIST OF TABLES

CHAPTER– 1

INTRODUCTION AND MOTIVATION

The discovery of antibiotics has impacted the human ailments by providing relief from microbial diseases. Prior to the evolution of antibiotics, the human sufferings from microbial diseases ranged from discomfort to death. The antibiotics acted on the microbial by either curtailing their growth or destroying them. A scientific approach to control the bacterial infections was initiated in the 19th century by Nobel laureate P. Ehrlich[1]. He discovered the selectivity of dyes in binding to bacteria and the destruction of the bacteria by dyes which were used as coloring agents with bacterial selectivity that provided a protection for the healthy bacteria. His research on bacterial infections led to the discovery of a chemical, arsephenamine, that cured the disease "syphilis" which resulted in the treatment procedure to be called as "chemotherapy". Stimulated by Ehrlich's work, several other drugs for bacterial infections were discovered by Nobel laureates Selman Waksman [2] and Alexander Fleming [3]. The most notable one was the discovery of penicillin as a wonder drug for curing many bacterial diseases. A mass scale production of this drug was initiated to cure soldiers infected with bacterial diseases during the Second World War. Over the past century, a number of antibiotics were discovered for curing bacterial diseases; they can be divided into two types. The first type is bactericidal, which is aimed at killing the bacteria. The second type is bacteriostatic which is to prevent the bacterial growth. World Health Organization (WHO) introduced a safe antibiotic, ciprofloxacin (CP) for a wide range of bacterial infections starting from bone joint infections, diarrhea, typhoid fever, urinary and respiratory infections in 1987. It is a wide spectrum antibiotic and has been used in humans and animals. Consequently, it enters the soil through several different pathways and introduces immunity in the humans and animals.

A rapid and convenient method of determining CP would be desirable for avoiding over dosage of it and to control its immunity. Electrochemical methods [2] have been developed based on the electrochemical activity of CP with all of them having limitations and interferences. This thesis is directed towards overcoming the limitations that will lead to the development of a portable sensor for ciprofloxacin. Graphene quantum dots have been used as a platform for this development as it has been shown to have a larger surface area than the materials used earlier in the literature [4-6].

1.1 Graphene

Graphene is a two-dimensional (2D) flat monolayer made up of carbon atoms tightly packed into a honeycomb lattice [7]. Graphene is a 2010 Nobel Prize invention by Drs. Andre Geim and Konstantin Novoselov, of the University of Manchester, United Kingdom. It has exceptionally unique properties and is considered as a wonder material [7]. Graphene is the strongest and thinnest material ever known and has the smallest effective mass. Despite being the thinnest material, graphene is perfectly transparent. It is ultra-light, immensely tough and is 200 times stronger than steel but still incredibly flexible. It is an awesome conductor with giant intrinsic mobility but also a perfect barrier for penetration of liquids and gases. The charge carriers of graphene can travel micrometer-long distances without undergoing room temperature scattering. In addition to high stiffness, large electrical and thermal conductivities, graphene can sustain very high current densities (almost 6 orders higher than copper). All these exceptionally outstanding properties of Graphene make it an active material for research and investigation.

Figure 1.1 below shows the schematic structure of Graphene and its ability to behave as a building block for all graphite forms.

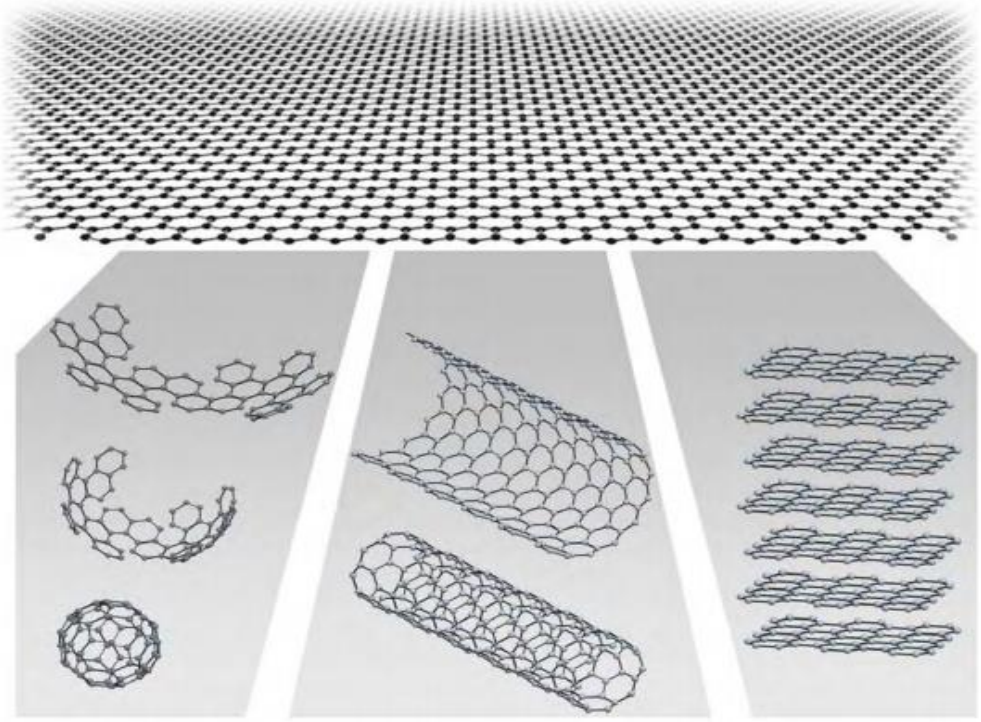

Figure 1.1 Graphene – Mother of all graphitic forms [7].

Graphene can be grown in several ways. *Figure 1.2* below shows four different routes of growing 2D graphite or graphene.

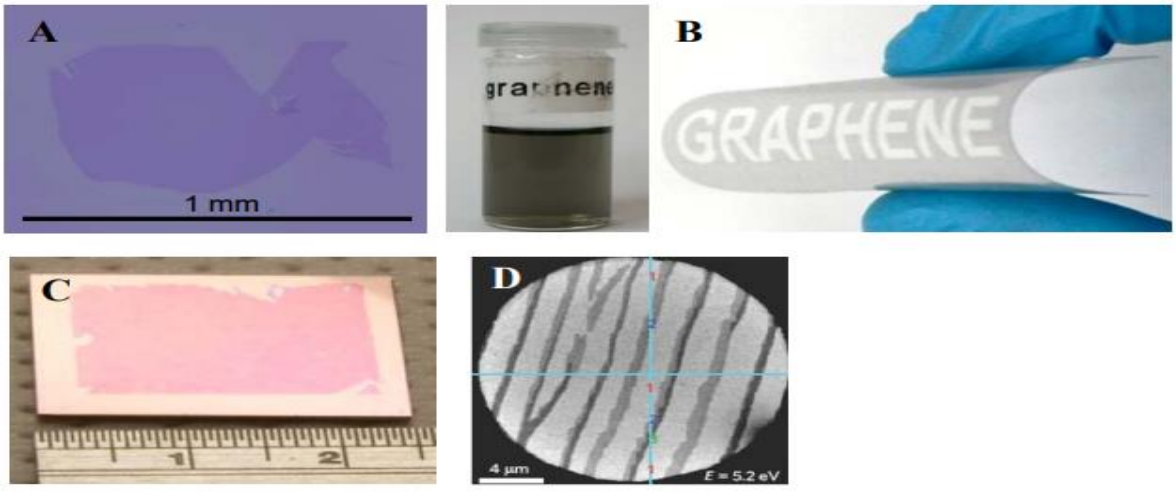

Figure 1.2. Four different ways of making Graphene [7], [8], [9] and [10].

Figure 1.2A, also referred to as the scotch-tape technique involves the mechanical splitting of strong layered materials such as graphite into individual single layered atomic planes also called graphene monolayers [7]. By this technique, crystals of strong structural and electronic quality are produced with sizes of a few millimeters. *Figure 1.2B* indicates the process of ultrasonic cleavage in which graphene atomic planes are partially detached first by intercalation and then by ultrasonic cleavage of chemically loosened graphite [8]. This sonification method is highly efficient and has been used to largely produce graphene on an industrial scale. *Figure 1.2C* refers to the 3D epitaxial growth of graphitic layers on top of other crystals [9]. During the 3D growth, the epitaxial layers remain bound to the underlying substrate with minimal bond breaking fluctuations. *Figure 1.2D* represents one of the routes to grow graphene wafers on silicon carbide (SiC) [10]. With recent advances in growth, transfer and cleavage techniques [8] - [10], the production of graphene in bulk and wafer-scale is not very challenging.

The optical and electrical properties of graphene are very unique [11]. Graphene exhibits a half-integer Quantum Hall Effect (QHE) relating the charge, density and velocity of charge carriers [12]. A single sheet of graphene is highly transparent yet each layer absorbs white light up to 2.3% and has less than 0.1% reflectance [13]. The exceptional optical properties of graphene, arising from the reflectance and transmittance of graphene in the optical region, are largely determined by the direct inter-band electron transitions. Its linear absorbance increases with respect to the number of layers stacked on top of each other.

Graphene also exhibits excellent thermal and mechanical properties. In free-standing graphene, the path of phonon scattering is uninterrupted and hence it has a very high thermal conductivity of 3000-5000 W m^{-1} K^{-1} [14]. The thermal conductivity, however, drops to 600 W m^{-1} K^{-1} if graphene is attached to a substrate. The drop in thermal conductivity is attributed

to the interference of phonon movement at the interface. The high thermal conductivity of graphene is mainly because of the presence of holes in its structure, which allow phonons to pass through unimpeded. In addition, graphene is specified by extremely high Young's modulus (1.0 TPa), in-plane stiffness (42 N m^{-1}) and highest strength (130GPa) [15]. The exceptionally good mechanical properties of graphene are of utmost importance because of their applications to use graphene as a structural material and understand durability of graphene in electronics and energy storage.

The remarkable properties of graphene hence make it a subject of explosively growing research whose trends and key results are very fascinating and significant.

1.2 Graphene Quantum Dots

Development of quantum mechanics has driven many investigations for solving the puzzle of atomic spectra [16]. The developments in semiconductor technology has enabled the fabrication of really small structures with a highly resolvable discrete quantum level structure. Several powerful new spectroscopic methods and probes have been used to study these small structures called "artificial atoms". In a semiconductor, artificial atoms are small boxes of 100nm, capable of holding number of electrons that can be varied as required [16]. By controllably varying the number of electrons in the artificial atoms of a semiconductor, many exciting atomic physics experiments have been conducted in a regime which is inaccessible to those performed on real atoms. The electrons of the artificial atoms are confined to a quantum well and are called quantum dots (QDs) [17]. QDs have highly tunable optical and electronic properties, which differ significantly from those of large particles. Their potential applications include solar cells, transistors, quantum computing, medical imaging and much more [17].

Graphene Quantum Dots (GQD) or Graphene Quantum Discs (GQD) exhibit the characteristics of both graphene and quantum dots [18]. Because of incredibly small pieces of graphene of size less than 30nm, GQDs possess highly superior properties like large diameter, high surface area and better surface grafting.

GQDs belong to the class of recently discovered Nano-carbons comprising of discrete, quasi-spherical nanoparticles with sizes below 50nm [19]. In comparison with conventional semiconductor QDs, GQDs are superior because of their low toxicity, chemical luminescence, chemical stability, excellent biocompatibility and many more special physical properties [20]. A structural schematic of GQD is shown in *Figure 1.3* below.

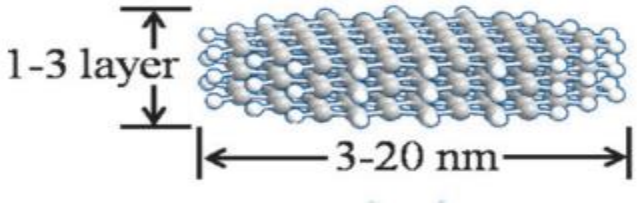

Figure 1.3. Structural depiction of GQD [20].

The sizes of most GQDs are mostly in the range of 3-20 nm consisting of no more than 5 graphene sheet layers. The shape of most GQDs is circular or elliptical, however, some GQDs in the shape of triangular, quadrate and hexagonal dots also exist. The behavior of composite elements (C, O and H) and the surface groups (carbonyl, carboxyl, hydroxyl and epoxy groups) of GQDs is similar to graphene [18]. The crystalline nature of graphene in GQD has been experimentally verified by many techniques like Raman spectroscopy, X-Ray diffraction patterns and high resolution transmission electron microscopy.

A variety of methods have been developed to produce GQDs [18]. Major methods of producing GQD include both top-down and bottom-up approaches. The methodology in top-down techniques is cutting down large graphene sheets, graphite, carbon fibers or carbon nanotubes into small pieces of graphene sheets [21], whereas, bottom-up approaches use small molecules as starting material to build GQDs. The synthesis of GQD by bottom-up techniques is complex requiring stringent conditions [22], however, these techniques have the ability to control the band gap and produce GQD with a controlled size. Though the production of GQD by top-down methods is still being researched upon, the top-down approaches are comparatively cheaper and simpler than bottom-up methods [22].

The schematic of top-down and bottom-up approaches of synthesizing GQD is shown in *Figure 1.4* below.

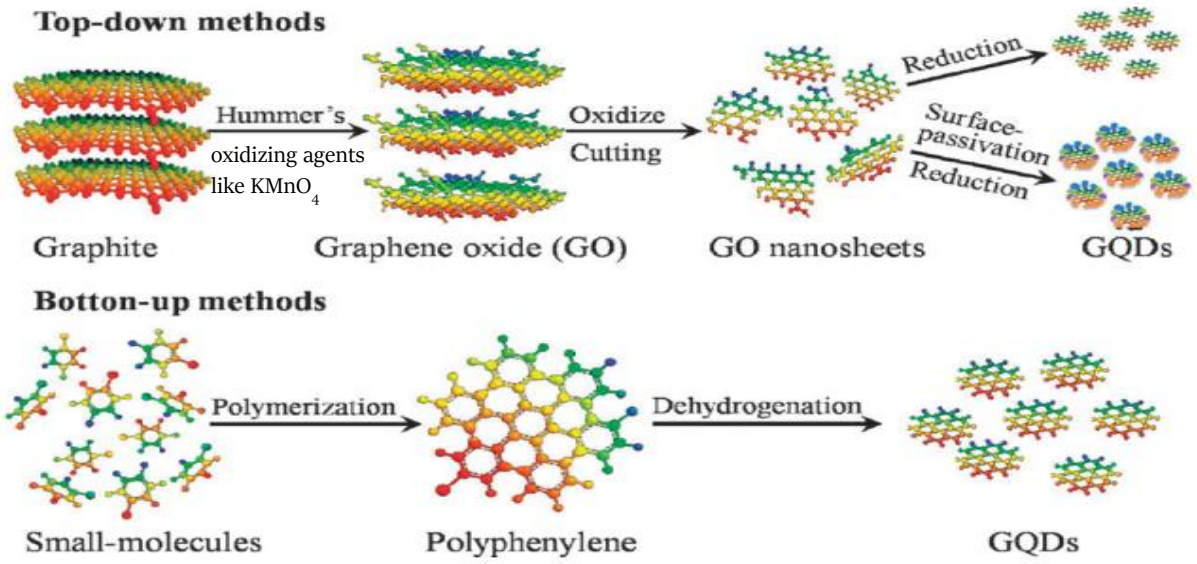

Figure 1.4. Schematic for top-down and bottom-up strategies for GQD synthesis [18].

GQD synthesis by top-down approaches can be done by techniques like laser ablation of graphite [23], electrochemical oxidation of graphite [24], electrochemical soaking of carbon

nanotubes [25], thermal oxidation of suitable molecular precursors [26] and microwave synthesis [27]. GQD is synthesized by bottom-up strategy by using carbonization as starting materials through microwave-assisted hydrothermal method [28], benzene derivatives as starting materials through stepwise solution chemistry methods [29], fullerenes as starting materials through ruthenium-catalyzed cage-opening [30]. The main research breakthrough in GQD production, by both top-down and bottom-up approaches is finding an efficient process that can take GQD synthesis to an industrial level and making efficient use of the exceptionally outstanding properties of GQD.

The unique properties of GQDs which are a result of the combination of graphene structure with quantum confinement and edge effects of QDs have found many exciting applications [31]. GQDs have potential applications in the fields of bio-imaging, sensors, photovoltaics, catalysis, opto-electronics, energy and environment. GQDs are used as a key component in many sensors and analytical systems because of their novel properties and high level of performance [31]. GQDs have been investigated to develop electronic, photo-luminescent (PL), electrochemical and electro-chemiluminescent (ECL) sensors. *Figure 1.5*. below shows the illustration of GQD application in the field of sensors [31].

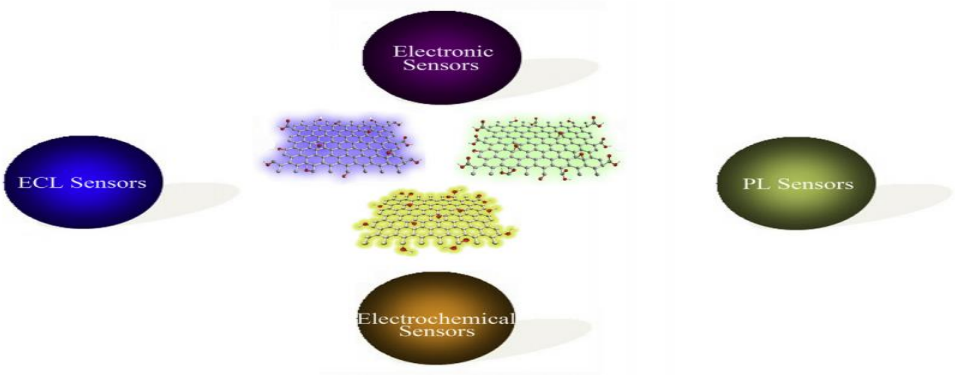

Figure 1.5. Application of GQDs in the field of sensors [31].

Because of an extremely high electrical conductivity of graphene, GQDs can be used to build electronic sensors and are used mainly in single electron transistor (SET) based charge sensors. SETs are a new type of switching device that used controlled electron tunneling to amplify current [32]. The large surface area of graphene enhances the exterior loading of the desired analyte on the sensor surface. High carrier mobility and density help in conduction of electrons between the analyte and the electrode surface. In addition to detecting charge in SETs, humidity and pressure [32] can also be detected by the electronic sensors built using GQD.

Photoluminescence (PL) of GQD depends on many factors like size, shape, excitation wavelength, pH, concentration, surface oxidation degree, surface functionalization, N-doping and S-doping [31]. GQDs are used to develop PL based sensors and the first PL based sensor was developed in 2012 where the fluorescence of GQD was selectively quenched by Fe^{3+} ions sensitively and selectively through the charge transfer process [33]. Both cations and anions are selectively detected by GQD based PL sensors.

Due to the electro-chemiluminescence (ECL) property of GQDs, which is a combination of electrochemistry and chemiluminescence, ECL sensors have been developed using GQD because of its simplified set-up, label-free nature, low background signal and high sensitivity [34].

GQDs are used as a novel electrode material not only in fuel cells, super-capacitors, photovoltaic cells, etc. but also in the field of electrochemical sensors [31]. One of the exciting applications of GQDs is the development of electrochemical sensors which overcome the poor selectivity and repeatability of enzyme based biosensors [35]. GQDs of tunable sizes 2.2 ± 0.3, 2.6 ± 0.2, and 3 ± 0.3 nm can act as multivalent redox species using cyclic voltammetry (CV) and differential pulse voltammetry (DPV) measurements, hence presenting potential opportunities for building electrochemical sensors by utilizing GQDs as probes [36]. GQDs have also been used to

develop electrochemical biosensors to sense biomolecules or molecules of biological importance with high efficiency and sensitivity [37]. The high performance of the GQD electrochemical sensors is attributed to the large surface-volume ratio and excellent biocompatibility of GQDs. These unique and novel properties of GQD have attracted tremendous research interest for the development of sensitive, reliable, selective sensors using GQD.

1.3 Ciprofloxacin – Structure and significance

Antibiotics are regarded as clinically safe and well-tolerated class of antimicrobials [38], however, they may have very serious negative side-effects. Depending on the type of microbes targeted, the patient's individual health and the class of antibiotics taken, the extent of side effects ranges from mild to very severe. Common side effects of antibiotic overdose include severe watery diarrhea, white patches on tongue, vomiting, allergic reactions like rash, swelling of tongue or lips and shortness of breath [38]. In order to prevent adverse side effects due to antibiotic administration, it is important to measure the antibiotic's concentration by developing an antibiotic sensor. Researchers have been actively trying to develop antibiotic sensors which can detect minute traces of the antibiotics ranging as low as micro-molar and nano-molar [39]. In this study, an antibiotic named Ciprofloxacin (CP) has been extensively studied for developing an electrochemical sensor to trace minute levels of CP.

Ciprofloxacin (CP) is a second generation fluoroquinolone antibiotic which has a broad activity spectrum for killing the bacteria [40]. Quinolones have evolved from a class of antibacterial agents to become really important and effective agents in the treatment of bacterial infections. The evolutionary pattern of quinolones has resulted in associated developments in activity, tolerability and pharmacokinetics through selection of useful and well-tolerated molecules [40]. The development of quinolone structures has been described along two parallel

pathways, the naphthyridones and fluoroquinolones [40]. Naphthyridones have the original naphthyridine core of nalidixic acid. Fluoroquinolones have a carbon atom which is substituted by nitrogen at the 8th position of the naphthyridine nucleus [40].

Table 1.1 shows the development of quinolone structures for the first two generations of quinolones.

Table 1.1. Development of structures for first two generations of quinolones [40].

	Core structure	
Generation	fluoroquinolone	naphthyridone
I	flumequine	nalidixic acid
IIa	ciprofloxacin, ofloxacin, (levofloxacin)	enoxacin
IIb	grepafloxacin, sparfloxacin	tosufloxacin
IIIa	moxifloxacin, gatifloxacin, sitafloxacin, clinafloxacin	trovafloxacin
IIIb	none yet developed	gemifloxacin

Second generation fluoroquinolones (IIa) have been investigated since mid-1980s for bringing about enormous changes in the clinical treatment of important bacterial infections [40]. CP has been effectively used to treat respiratory infections for adults and children suffering from cystic fibrosis, enteric fever, salmonellosis and infections like pyelonephritis, prostatitis, osteomyelitis, etc. with short course oral therapies.

The systematic International Union of Pure and Applied Chemistry (IUPAC) name of CP is 1-cyclopropyl-6-fluoro-4-oxo-7-(piperazin-1-yl)-quinoline-3-carboxylic acid [41] (*Figure 1.6.*). The molar mass of CP is 337.341 g/mol and generally exists in crystalline powder form generally [41]. The melting point of CP is about 255-257ºC and has low solubility in water at room

temperature. It can exist freely as CP or in bound forms like anhydrous ciprofloxacin hydrochloride, ciprofloxacin monohydrochloride monohydrate and ciprinol.

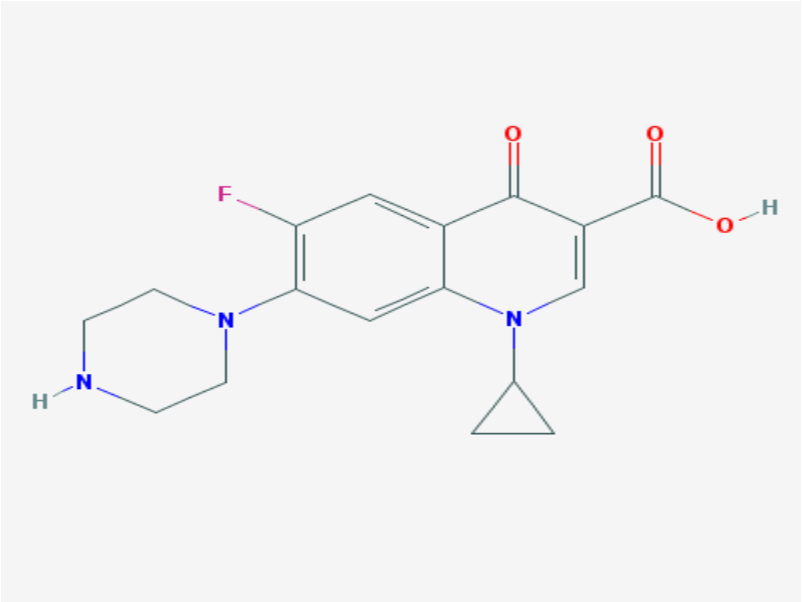

Figure 1.6. Structure of CP [40].

The solubility of CP extremely depends on the pH value of the medium in which it is present [40]. At pH 4-5, it shows the highest solubility (>40mg/ml) [40] because of the formation of hydrochloride when the solution pH is altered using hydrochloric acid. CP is almost insoluble in neutral pH range [40]. However, its solubility decreases with increasing pH showing a solubility of approximately 30mg/ml at pH 11.

CP has two ionization states coexisting at physiological pH: a zwitterionic form with a significant dipole, and an uncharged neutral form (with negligible/minor dipole), with the latter being predominant [41]. The molecular structures of neutral and zwitterionic CP are shown in Figure 1.7.

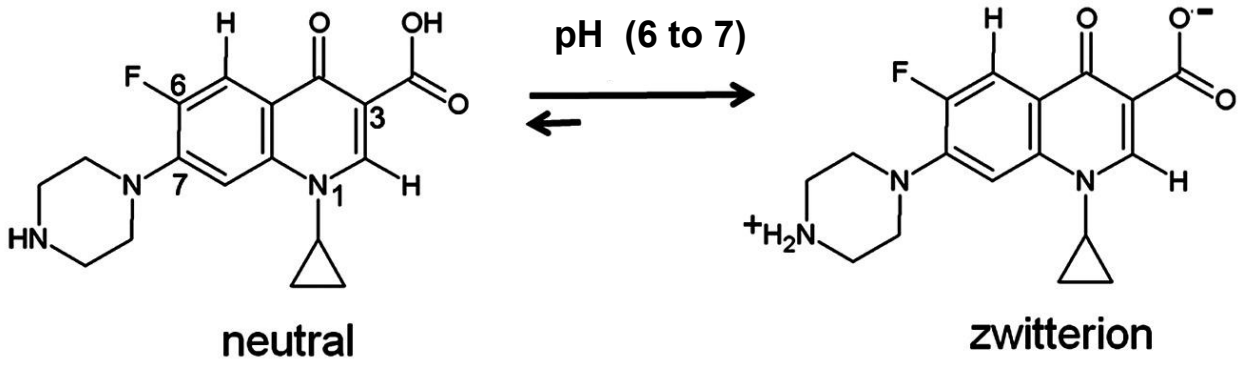

Figure 1.7. Molecular structures of neutral and zwitterionic CP [41].

Figure 1.7 shows that the central structural unit of CP is a quinolone ring with the fluorine atom at C-6, a piperazine moiety at C-7, a cyclopropyl ring at position 1 and a carboxyl group at position 3 [41]. Zwitterionic structure of CP shows that CP exists in anionic form in the neutral pH range, which is used in the studies here.

CP is widely administered to humans and livestock for treatment of a number of bacterial infections [40]. Major infections that can be treated by taking the prescribed dosage of CP include bone and joint infections, respiratory tract infections, skin infections, urinary tract infections, intra-abdominal infections, typhoid fever, and few types of infectious diarrhea. However, CP has serious side effects [42]. Overdose of CP may result in risk of worsening muscle weakness, tendon rupture, renal toxicity, cerebral thrombosis, chest pain, myocardial infarction, cardiopulmonary arrest, etc.

An important environmental reservoir of antibiotic-tolerant bacteria is wastewater [43]. Antibiotic-tolerant populations include both intrinsically resistant organisms and bacteria that acquired genetic determinants able to confer resistance [44]. CP is one of those antibiotics which is found in surface waters because of incomplete metabolization of the drug [45]. When CP is present in waste waters, it highly impacts agricultural runoff and domestic waste water effluents by creating potential for antibiotic resistant bacteria. Because of its significance on human health

and the environment, monitoring and sensing the concentration of CP is causing increasing concern among scientists, pharmacologists, environmentalists and researchers.

1.4 Analyte detection and sensing methods

A specific ion, molecule or compound that is being tested in a study is called as an analyte and there are numerous techniques for identification of analytes called elemental/molecular analysis [46]. Some of the techniques used for organic and inorganic elemental/molecular analysis include the following [46]:

- Electrochemical methods
- Photometry and spectrophotometry
- Atomic emission/absorption spectroscopy
- Neutron activation analysis
- Nuclear magnetic resonance (NMR) spectroscopy
- Fourier transform infra-red (FTIR) spectroscopy
- Inductively coupled plasma mass spectroscopy
- X-ray fluorescence analysis
- Ion chromatography
- Spectrofluorimetry
- Immunoassay
- Chemiluminescence
- Mass spectroscopy coupled with chromatography
- X-ray diffraction/fluorescence
- Titrimetry

- Capillary electrophoresis

Some of the above mentioned techniques are used for detecting and measuring CP concentration. The analytical techniques used to study CP include liquid chromatography−mass spectroscopy (LCMS) [47], high-performance liquid chromatography (HPLC) [48], spectrophotometry [49], spectrofluorimetry [50], capillary electrophoresis [51], immunoassay [52], chemiluminescence [53] and electrochemical techniques [54]. Most of these techniques are very effective in CP determination but may have disadvantages like being very expensive and time consuming.

In a study, to determine second class fluoroquinolones in human plasma [47], LCMS was used. A rapid, sensitive and selective method called hydrophilic interaction liquid chromatography – tandem mass spectrometric (HILIC – MS/MS) was developed. Levofloxacin and CP were extracted from human plasma with dichloromethane and analyzed. For a 20µL plasma sample, the lower limit of quantification was 10 ng/ml and recoveries of CP and levofloxacin were 77.3% and 55.2% respectively. The retention of zwitter- ionic CP and levofloxacin was also successfully demonstrated by this method.

Samanidou et al [48], developed a direct method for the determination of four fluoroquinolones like CP, norfloxacin, ofloxacin and enoxacin in human blood serum samples by using HPLC technique. The limits of detection values that were obtained as a result of this study were 0.02 ng per 20 µL injection for enoxacin and 0.01 ng for CP, ofloxacin and norfloxacin. At a concentration of 2 ng µL–1, the internal standard that was used was Hydrochlorothiazide (HCT). Statistical evaluation of this method gave satisfactory results with high precision and accuracy. Recovery of analytes in spiked samples was 97±6% over the range 0.1–0.5 ng μL^{-1} for this method.

In a study utilizing the solid phase spectrophotometry technique [49], a simple flow injection UV spectrophotometric sensing device was developed for CP determination. No derivatization was involved in this technique. The carrier solution used was formic acid/NaOH 1.75M at a pH of 2.2. This method involved packing of Sephadex SP C-25 cation-exchange gel beads in a flow cell and continuous monitoring of its native absorbance on the solid phase at 277 nm. When the analytical signal reached the maximum value, CP was eluted from the solid support by the carrier solution and its spectrophotometric response was monitored. In the concentration range 0.5–10 μg ml^{-1}, the response of the sensor was linear with a standard deviation of 0.79 percent.

Similar to the above mentioned study [49], in another study [50], a method for determining traces amounts of CP was developed using solid phase spectrofluorimetry. Analogous to the study previously mentioned [49], Sephadex SP C-25 gel beads were packed on a 1mm silica cell. The relative fluorescence intensity of CP was measured using a solid phase attachment. This method was applied to determine CP concentration in human and urine samples. The sample volume used was 1000 ml and the excitation and emission wavelengths used were 272 nm and 448 nm respectively. The detection limit obtained by this method was 0.1 ng ml^{-1} and the linear concentration range was 0.3-10 ng ml^{-1}. This method resulted in 100% recovery in all cases when it was validated by using HPLC as the reference method by applying standard addition methodology.

Hernandez et al. [51], used capillary isotachophoresis–capillary zone electrophoresis (ITP-CZE) to analyze three quinolones like CP, enrofloxacin and flumequine in pig plasma samples. Solid-phase extraction with Oasis HLB cartridges was used as a step up for sample pretreatment and cleaning. The sensitivity and sample loadability of CZE was increased by usage of ITP-CZE.

The detection limits of CP, enrofloxacin, flumequine were 70, 85, 50 µg L^{-1}. This method increased the sensitivity of the system by 40 times and hence has been used as an alternative to HPLC in the analysis of quinolones residuals in biological samples.

Huet et al [52], developed an enzyme-linked immunosorbent assay (ELISA) to directly detect broad range of fluoroquinolones in various matrices. This method involved a simple, rapid extraction of this class of antibiotics, which was carried out with a 1:1 mixture of methanol and phosphate-buffered saline adjusted to pH 7.4. By this common extraction, 15 fluoroquinolone residues was detected in samples from pig kidney, poultry muscle, egg, fish, and shrimp. This method had advantages like direct and simultaneous determination of fluoroquinolones and for most of these compounds, the assay's detection capabilities were <10µg kg^{-1}.

In a study [53], utilizing chemiluminescence (CL) for CP determination, CP in biological fluids and in CP hydrochloride tablet and injection has been determined by a novel, rapid, sensitive and analytical method. This method utilized enhanced CL with flow-injection sampling and is based on the chemiluminescence reaction of the potassium permanganate–sodium thiosulfate–CP system. The optimum conditions of chemiluminescence and the development of enhanced chemiluminescence reaction were investigated in this study. When the concentration of CP was in the range from $1x10^{-8}$ to $1x10^{-5}$ g ml^{-1}, the chemiluminescence intensity was linearly dependent on CP concentration. The detection limit of this technique was $4x10^{-9}$ g ml^{-1}. The standard deviation of this method was 1.8% and because of the simple and sensitive determination of CP, this method has been successfully used in pharmaceutical analysis.

Although, a variety of techniques have been used successfully by many researchers for determination of CP, there are several disadvantages associated with these techniques. Some of the disadvantages are listed below [53]:

- Methods used for sample processing are complicated.
- Sensitivity is low.
- The analytical conditions are harsh.
- Instrumentation is very expensive.
- One complete trial of the experiment requires a lot of time.

Due to the disadvantages of these techniques, a new, simple, fast, rapid and highly sensitive technique with simple instrumentation is required for quick and effective analyte detection. The advantages of electrochemical techniques have made them an effective alternative tool for analyte (CP) detection [46].

1.5 Electrochemical sensing methods

Identification of analytes and determination of organic and inorganic compounds by electroanalytical techniques has been very popular among scientists and researchers [46]. The most popular electroanalytical methods are polarographic and voltammetric techniques. The techniques are applicable for identification of electrochemically oxidizable compounds (e.g., aromatic amines, phenols) and electrochemically reducible compounds (e.g., nitro, nitroso, and azo). Voltammetric peak potentials are measured for identification. Voltammetric peak currents are related to concentration of the species under investigation. Electrochemical techniques have many advantages over the other conventional analytical techniques [46]. Some of the advantages of electrochemical techniques are listed below:

- Low energy requirement
- Minimal or no requirement for sample preparation
- Low cost

- Simple instrumentation
- High sensitivity
- Short time requirement
- Ease of use

Many researchers have actively used electrochemical techniques for elemental/ molecular analysis as well as for advanced chemical analysis. A short review of some of the electrochemical research studies for CP determination and analysis is given below.

Yan et al. [54], developed a photo-electrochemical detecting platform for CP detection in their study. The detection platform was constructed using metallic Bismuth (Bi) self-doping bismuth oxybromide, BiOBr (Bi/BiOBr) composites on Indium tin oxide (ITO). The Bi/BiOBr composites was fabricated by ethylene glycol (EG)- assisted solvo-thermal method. The metallic nanoparticles of Bi were evenly distribute on the surface of BiOBr microspheres. Excellent photo-absorption property and photoelectric conversion efficiency in visible region was exhibited by the Bi/BiOBr composites. A photo-electrochemical detection mechanism based on valence band (VB) and conduction band (CB) of the photo-electrochemical detecting platform using this technique is shown in *Figure 1.8.*.

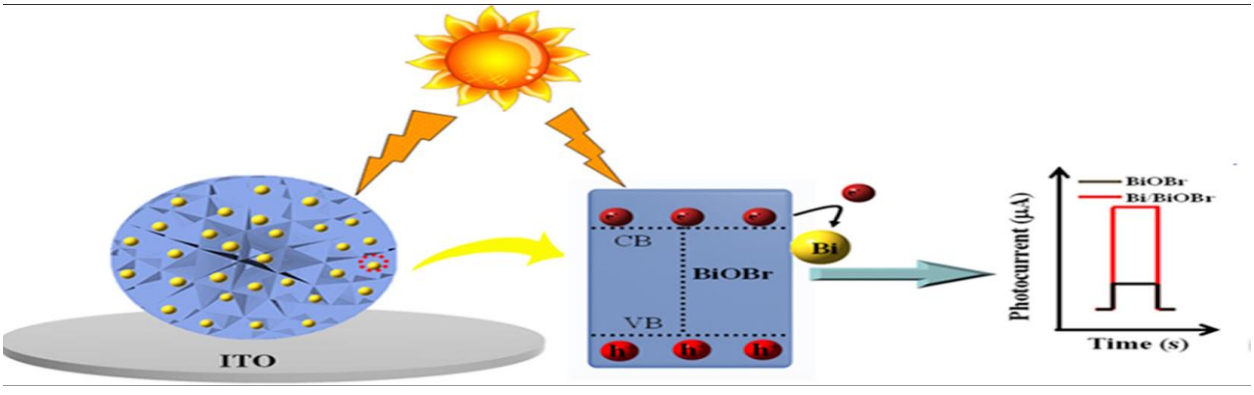

Figure 1.8. Photo-electrochemical detection mechanism [54].

As a result of the study, it was found that, the photocurrent density of Bi/ BiOBr composites is superior to pure BiOBr. The increased photoelectrochemical properties of Bi/BiOBr were used to develop a photo-electrochemical sensor for CP. The photo-electrochemical sensor exhibits a good linear relationship, a low detect limitation and relatively stability.

In a study to develop a simple, rapid and applicable electrochemical method for sensing CP in urine and serum samples, Fotouhi et al. [45], used a system of multi-walled carbon nanotubes film-modified glassy carbon electrode (MWCNT/GCE). The constructed system exhibited excellent direct electro-catalytic behavior in the oxidation of CP. This was further evidenced in the study by the enhancement of the oxidation peak current and the shift in the oxidation potential to lower values (by 130 mV) in comparison with the bare GCE. The results of this study indicated a detection limit of 6 µmol/L.

In another study, Zhang et al., developed an electrochemical method to detect CP in the presence of ascorbic acid, dopamine and uric acid [55]. Glassy carbon electrode modified with poly(alizarin red)/electrodeposited graphene (PAR/EGR) composite film was used in the study. The direct electro catalytic oxidation of CP on AR/EGR was investigated by two electrochemical techniques called as cyclic voltammetry (CV) and differential pulse voltammetry (DPV). A schematic representation of this method is given in the *Figure 1.9.* below.

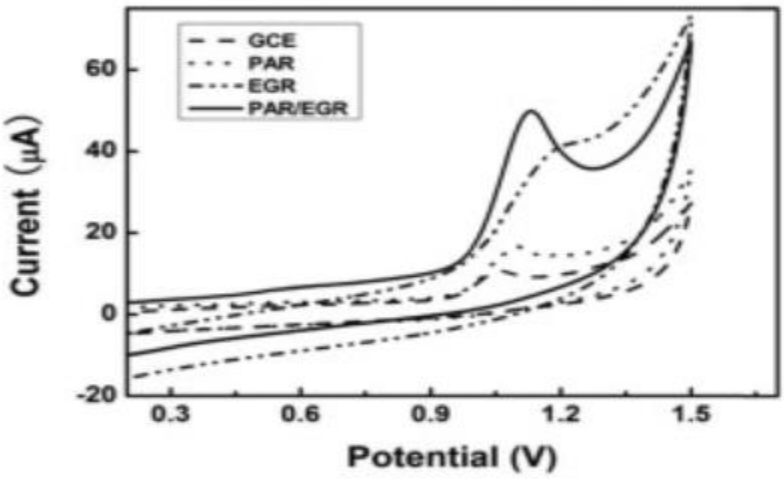

Figure 1.9. An electrochemical sensor based on direct electrochemical oxidation of CP. [55].

The detection limit of CP using this technique was observed to be 0.01M and the linearity of CP concentration ranged from $4x10^{-8}$ to $1.2x10^{-4}$ M.

Ensafi et al. [56], investigated the electrochemical behavior of $MgFe_2O_4$ nanoparticles in modified multiwalled carbon nanotubes ($MgFe_2O_4$-MWCNTs). A voltammetric sensor was developed using the $MgFe_2O_4$-MWCNTs for the direct electro catalytic determination of CP. The $MgFe_2O_4$-MWCNTs electrodes showed an oxidation peak potential at around 250 mV as shown in *Figure 1.10.* below.

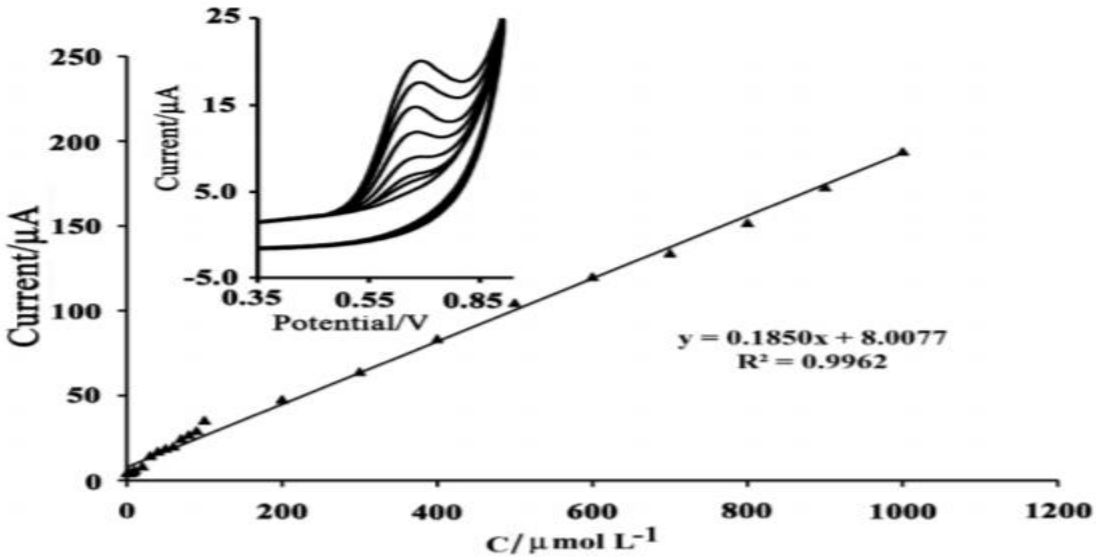

Figure 1.10. Calibration plot and voltammograms of CP based on direct electrochemical oxidation of CP in 0.1 M L^{-1} at pH 3.0 and scan rate of 100 mV s^{-1} [56].

The oxidation peak current was dependent on the CP concentration, which was linear over the range of 0.10 – 1000 µmol L^{-1}. The detection and quantification limits obtained in this study are 0.01 and 0.08 µmol L^{-1} respectively.

In a study [57] where, the voltammetric behavior of CP was investigated using cyclic voltammetry and differential-pulse anodic stripping voltammetry at bare glassy carbon (GC) and DNA modified glassy carbon (DNA-GC) electrodes, only one anodic irreversible wave was observed in both the techniques in this study. The detection limit of CP in this technique was 0.117 µM. The peak current and CP concentrations showed a linear relationship which was observed in the range 1.0–10.0 µM. The DNA-modified electrode exhibited increased sensitivity towards the direct electrochemical oxidation of CP as compared with the unmodified electrode.

Gayen et al. [58], carried out electrochemical studies to develop electrochemical sensors for the detection of CP in natural waters and wastewater effluents. The sensors were developed using multiwalled carbon nanotubes (MWCNTs) dispersed in a porous Nafion film on to a boron-doped diamond (BDD) electrode substrate. The porous-Nafion-MWCNT/BDD electrode were more favourable for CP detection due to selective adsorption, which was accomplished by a combination of electrostatic attraction at $-SO_3^{(-)}$ sites in the porous Nafion film and the formation of charge assisted hydrogen bonding between CP and -COOH MWCNT surface functional groups. A limit of detection of 5 nM was obtained using differential pulse voltammetry.

All the above mentioned studies [45], [55]-[58], have a limitation of reproducibility due to the direct electrochemical oxidation of CP. This is an irreversible process and hence the location of the oxidation peak will shift with the concentration of CP. Another problem is that background electrolytes like ascorbic acid undergoes oxidation at an earlier potential. The direct oxidation of CP which occurs at positive potentials where the concurrent oxidation of the background electrolyte occurs. These limitations develop the need to study CP in an approach that does not utilize direct oxidation of CP.

1.6 Aim and scope of the thesis

As described in the above literature review [6]-[37], the novel materials graphene and GQDs have exceptionally outstanding properties and attributes useful for sensor functioning. CP significantly impacts the human health and the environment and is important for determining the concentration [45]. Electrochemical studies are advantageous over other analytical techniques in determining an analyte's concentration [46]. However, the electrochemical methods used for CP concentration determination [45], [55]-[58], use direct oxidation of CP which occurs close to

background electrolysis, thereby causing sensitive detection problems. All these concepts have been the basis for the motivation of this study.

In this study, GQD was used to develop a sensor methodology for CP with ferric ion as a probe and the unique properties of GQD. Two sensor methodologies for CP concentration determination were formulated:

1. Electrochemical sensor (formulated by an electrochemical technique called Differential Pulse Voltammetry (DPV)); and
2. Resistive sensor (formulated by resistance measurement technique)

The unique and novel properties of GQD were utilized in each of the two sensor methodologies developed. The mechanism by which the above methodologies work to determine the concentration of CP and the effect of interferences in CP concentration determination is also described.

The unique component in this research is the use of a probe (ferric ion – Fe^{3+}) which gets attached to CP and helps in the CP concentration determination. There has been no study so far that has proposed a method to bind CP to ferric ion and to determine CP concentration by monitoring the electro-reduction behavior of the bound species, thus making the research unique. The working electrodes used during electrochemical investigation of CP include bare unmodified Glassy Carbon Electrode (GCE) and GCE modified by GQD. The performance of the two different electrodes have been studied and compared by employing ferric ion as a probe to sense CP. The determination of detection limit, sensitivity and reproducibility of this technique are presented. The challenges faced in CP concentration determination while using electrolyte of different pH ranges and carbon nanotubes (CNT) pipette electrodes as working electrodes are also discussed.

The mechanism for the resistive sensor developed for CP is formulated by measuring the resistance of an inter-digitated gold electrode sensor. The resistance of the sensor in air and in solutions of different CP concentrations were measured. The sensor mechanism is developed based on the change in resistance of the sensor with respect to the concentration of CP. The photoluminescence property of CP [40], [54] was utilized to establish binding of ferric ion to CP. The determination of CP concentration and the effect of interferences on CP concentration measurement was investigated for the sensor and described in detail in the forth-coming chapters of the thesis.

The entire thesis is divided into five chapters and each chapter is divided into several sections based on the content and idea that is presented. The first chapter is an introduction to review the scientific developments and to provide the motivation of this study. The second chapter provides details about experimentation involved. The third chapter is a presentation of results of the experiments performed. The fourth chapter provides the conclusion with emphasis on the merits and demerits of the study. The scope of future work and developments has also been briefly given in the last chapter.

CHAPTER – 2

EXPERIMENTAL DETAILS

2.1 Chemicals

The following *Table 2.1.* provides the details about the different chemicals used in the study.

Table 2.1. Details about chemicals used

Chemical name	**Chemical formula**	**Molecular weight (g/mol)**	**Company**	**Assay (%)**
Sodium sulfate (anhydrous)	Na_2SO_4	142.04	EMD Chemicals, Inc.	99.0
Ferric Chloride (hexahydrate)	$FeCl_3.\ 6H_2O.$	270.295	Acros Organics - Fisher Scientific	99+
Potassium Chloride	KCl	74.55	Fisher Scientific	98
Potassium Ferrocyanide	$K_4[Fe(CN)_6].\ 3H_2O$	368.35	Fisher Chemical | Fisher Scientific	99.8
GQD	[Graphene]	-	Electrochemically manufactured by a US patented method [59]	-
CP	$C_{17}H_{18}FN_3O_3$	331.346	Sigma-Aldrich Chemicals company	≥98.0
Urea	CH_4N_2O	60.06	Fisher Chemical	99.2
Hydrochloric acid	HCl	36.46	EMD Chemicals, Inc.	98
Sulfuric acid	H_2SO_4	98.079	EMD Chemicals, Inc.	98

Acetic acid	CH_3COOH	60.05	Macron Fine Chemicals	96
Sodium acetate	CH_3COONa	82.03	Sigma-Aldrich Chemicals company	95
Argon gas	Ar	39.948	Linde, Fulton, NY	99.9
Oxygen gas	O_2	32	Linde, Fulton, NY	99.9

GQD used in this study was manufactured by a US patented method [59], where GQD is produced in a single step process involving no secondary purifications. The process utilizes an electrochemical cell containing electrodes with variable gaps including a zero gap, containing an anode electrode including graphite, a cathode electrode including electrically conductive material with an electrolyte-free electrochemical bath including water and an organic liquid that produces joule heating along with oxygen embrittlement.

2.2 Materials for experimentation

The *Table 2.2.* given below provides the experimental materials used with the names of the company from which they were procured.

Table 2.2. Experimental materials procurement details

Material	Company
Working electrode – GCE	Gamry Instruments
Working electrode – Platinum (Pt)	Gamry Instruments
Working electrode – CNT pipette electrode	Nano Bio-Interface Laboratory (NBIL), RIT
Reference electrode – Standard Calomel electrode (SCE)	Gamry Instruments

Counter electrode – Graphite	Gamry Instruments
Screen Printed electrode (SPE)	Gamry Instruments
Fluorescence cuvette	Fireflysci cuvette shop
UV-Visible absorption cuvette	Fireflysci cuvette shop
Inter-digitated gold electrode sensor	Electronics Design Center (Case Western, Ohio)
Pipettes, burettes, emery paper, volumetric flasks, scintillation vials, beakers and graduated cylinders	A-level stockroom of School of Chemistry and Materials Science, College of Science, RIT.

2.3 Instruments and equipment

The *Table 2.3.* given below provides the names of manufacturers from whom the instruments used to carry out experiments were purchased.

Table 2.3 Instruments and equipment details

Equipment and instruments	**Manufacturers**
Fourier Transform Infra-Red (FTIR) spectroscopy	Biorad Excalibur Series FTS 300
Fluorescence spectroscopy	Horiba Jobin Yvon Fluoromax-4
UV-visible absorption spectroscopy	Shimadzu UV-2501PC
Electrochemical workstation	Gamry Instruments
Meter view resistance measurements	22-812 Meter View Version 1.0

2.4 UV-Visible absorption spectroscopy

2.4.1 Basic principle

The UV-Visible absorption spectroscopy is based on the absorption of ultra-violet (UV) or visible radiation by the species under investigation [60].

The absorption is a two-step process:

1. Electronic excitation of the species

$$M + h\upsilon \rightarrow M^{*} \quad (2.1)$$

where, M represents the molecular species under investigation,

$h\upsilon$ represents the energy of the photon and

M^{*} represents the absorption product or the electronically excited species.

2. Relaxation of the excited species

$$M^{*} \rightarrow M + \text{heat} \quad (2.2)$$

Relaxation may occur by a photochemical process such as decomposition of M* to form new species or return of the species from its excited energy state to original energy state with the release of a photon. This photochemical transition is measured in the UV-visible absorption spectroscopy experiment.

The relationship between the absorbance and concentration of the absorbing species is linear and is explained by the Beer-Lambert's law [60], which is given by,

$$A = a(\lambda) * b * c \quad (2.3)$$

where, A is the measured absorbance (no units),

a (λ) is the wavelength-dependent absorptivity coefficient (M^{-1} cm^{-1}),

b is the path length (cm) and,

c is the analyte concentration (mol L^{-1} or M).

Since a (λ) is constant for a given species, b is constant in the experiment and A is experimentally determined absorbance, the value of c can be easily calculated from the Beer-Lambert's law.

2.4.2 Experimental set-up

In this study, UV-visible absorption spectroscopy was used to calculate the concentration of CP solutions. The solubility of CP is very low in water. Hence, the CP solutions, whose concentration was calculated by weighing the gram equivalent weight of CP solid, could not be used because of the turbid and unclear nature of the solutions. The turbid solutions were filtered until a clear solution was obtained. The unknown concentration of the clear CP solution was determined using UV-visible absorption spectroscopy. The schematic of Shimadzu UV-2501PC – High Resolution Spectrophotometer and the quartz cuvette in which the measurements were taken are shown in *Figure 2.1.* below:

Figure 2.1. a. Shimadzu UV-2501PC – High Resolution Spectrophotometer and

b. 1cm Quartz cuvette to study absorption

The measurements were carried out by putting the solutions in a 1cm quartz cuvette where two sides of the cuvette were fully transparent to light and the other two sides completely opaque to light.

2.5 Electrochemical detection

The electrochemical studies were carried out using three different techniques like differential pulse voltammetry (DPV), cyclic voltammetry (CV) and chronoamperometry to investigate the behavior of CP and ferric ion using working electrodes like bare GCE (diameter= 0.3cm, length=6in, area=0.071cm^2) and GQD modified GCE working electrodes (diameter=0.3cm, length=6 in, area= 0.071 cm^2). The performance of both the working electrodes was compared to show the enhanced effect of GQD. For all the electrochemical techniques, graphite rod (diam. 0.5 cm, length 6 in.) was used as the counter electrode and Standard Calomel Reference (SCE) (diameter=0.3cm, length=4 in, area=0.070 cm^2) was used as the reference electrode. Electrochemical measurements were done with CNT pipette electrodes as working electrodes. All the electrodes were polished with emery paper (Gator grit 220-b waterproof sand

paper) and cleaned with 1:1 1mM sulfuric acid and water. The electrodes were washed well with tap water and distilled water after cleaning. The *Figure 2.2.* below shows all the different electrodes and GQD used to modify GCE in the study.

Figure 2.2 Different electrodes and GQD used in the study [Present study]

a. Reference electrode, SCE, b. Working electrode, unmodified GCE, c. Counter electrode, Graphite rod and d. GQD.

GQD, used to modify GCE, was manufactured by a US patented method [59] and Scanning electron microscope (SEM) and Transmission Electron Microscope (TEM) were used for characterizing GQD samples [61]. The high-resolution TEM images of GQD is shown in Figure 2.3 below.

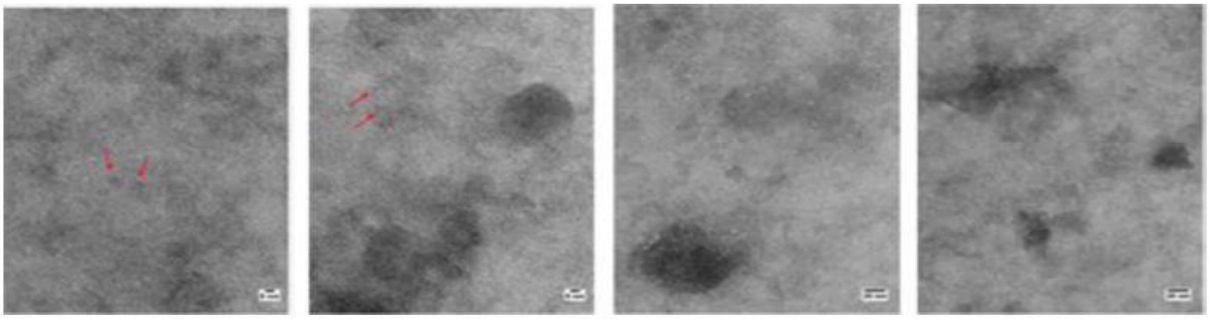

Figure 2.3.TEM of GQD sample [61]. Small particles found (arrows). Contrast enhanced to improve visibility. The original recorded scale is 0.5 cm = 5 nm on the red arrowed pictures. Image reduction 40%. The scale for non-red arrowed pictures is 1 cm = 20 nm; image reduction 35%.

All electrochemical measurements were performed with a Gamry Reference 600 potientiostat/galvanostat and in a Dr. Bob's cell^{TM} which consists of a five necked "V" shaped glass container to fit the working, counter and reference electrodes as shown in the *Figure 2.4.* below:

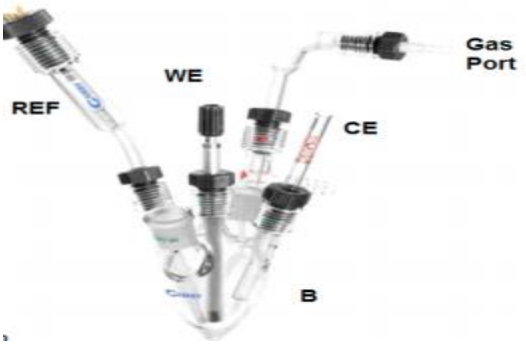

Figure 2.4. Dr. Bob's cell^{TM} used in the experiment. WE, CE, REF[Present study].

The background electrolytes used in different electrochemical measurements include:

a. 10ml - 0.1M Na_2SO_4 (for studying interaction of ferric ion with CP)

b. 10ml – 0.1M KCl (for GQD area calibration experiments done using 5mM $K_4[Fe(CN)_6]$. $3H_2O$ with GQD modified GCE)

c. 10ml – Acetate buffer (for studying effect of pH in CP determination)

d. 10ml - 0.1M Na_2SO_4 + 0.5 M Urea (for studying effect of interferences in CP determination)

Before carrying out the experiments, Dr. Bob's cell containing the electrolyte was bubbled with Argon gas for half an hour to ensure all the oxides were removed. After each addition of the electroactive species (ferric ion or CP), the electrolyte was bubbled with Argon gas for 1 minute, before studying the system electrochemically.

Some electrochemical experiments, like studying the effect of pH using acetate buffer as the electrolyte and studying the effect of urea which is an interference to CP determination, were done with a screen printed electrode (SPE) cell set-up. The *Figure 2.5.* below shows the cell stand of the SPE and a sample Carbon SPE.

Figure 2.5. a. SPE cell set up and b. Carbon SPE [Present study].

Being disposable electrochemical single use sensors based on the technology of screen printing, SPEs were used for obtaining fast, reliable and reproducible response with negligible

electrode maintenance. The effect of pH and interferences were studied electrochemically using SPEs.

2.5.1 Differential Pulse voltammetry (DPV)

DPV is an effective electrochemical technique, which measures trace levels of organic and inorganic species [62] and consists of fixed magnitude pulses superimposed on a linear potential ramp applied to the working electrode. The application of fixed magnitude pulses are shown in *Figure 2.6.* below.

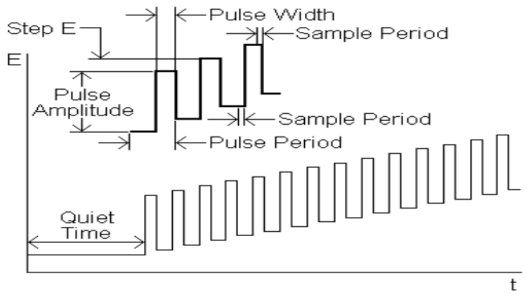

Figure 2.6. Application of fixed magnitude pulses in DPV [62]

The current is sampled twice in the DPV technique –

1. Before pulse application (includes charging and Faradaic current)
2. Before the pulse life ends (includes only Faradaic current)

The basis of DPV is the difference in the rate of the decay of the charging and the faradaic currents following a potential step or "pulse", E [63]. The charging current decays exponentially, but the faradaic current (for a diffusion-controlled current) decays as a function of $1/(\text{time})^{1/2}$. The rate of decay of faradaic current is hence slower than that of the charging current. At potentials which are not closer to the redox potential, there is no faradaic reaction in response to the pulse, so the current difference is zero. At potential around the redox potential, the net current (difference

between Faradaic current and charging current) reaches a maximum, and decreases to zero as the current becomes diffusion controlled. The current response usually consists of current peaks as shown below in *Figure 2.7.*

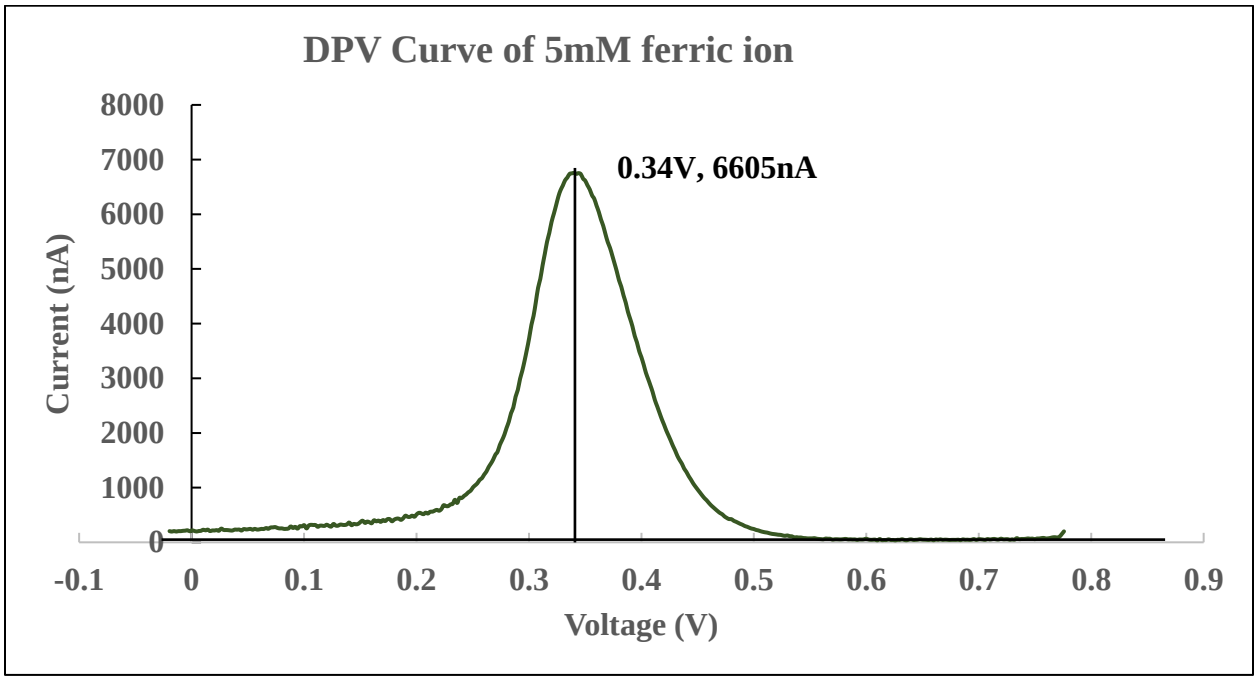

Figure 2.7. Sample DPV for 5mM ferric ion using unmodified GCE [Present study]

The peak potential E_p, is characteristic to the electro-active species under investigation. Hence, to identify the electro-active species, E_p is used based on the equation, $E_p = E_{1/2} - \Delta E/2$, where $E_{1/2}$ is the potential when current value is half of the peak current (V) and ΔE is the pulse height (V). The height of the current peak is directly proportional to the concentration of corresponding analytes. Hence, based on the peak potential and the peak current of the DPV curve, the concentration of ferric ion is monitored to determine CP concentration.

2.5.2 Cyclic voltammetry (CV)

CV is a very powerful electrochemical technique used for investigating the reduction and oxidation processes of atomic or molecular species [62]. CV is also extensively used for studying electron transfer-initiated chemical reactions, which includes catalysis. It is popular in qualitative electrochemical studies because of rapidly locating the redox potential for the electroactive species [62]. The basis of CV technique involves scanning a potential range of the working electrode linearly, using a triangular potential waveform as shown in *Figure 2.8.* below.

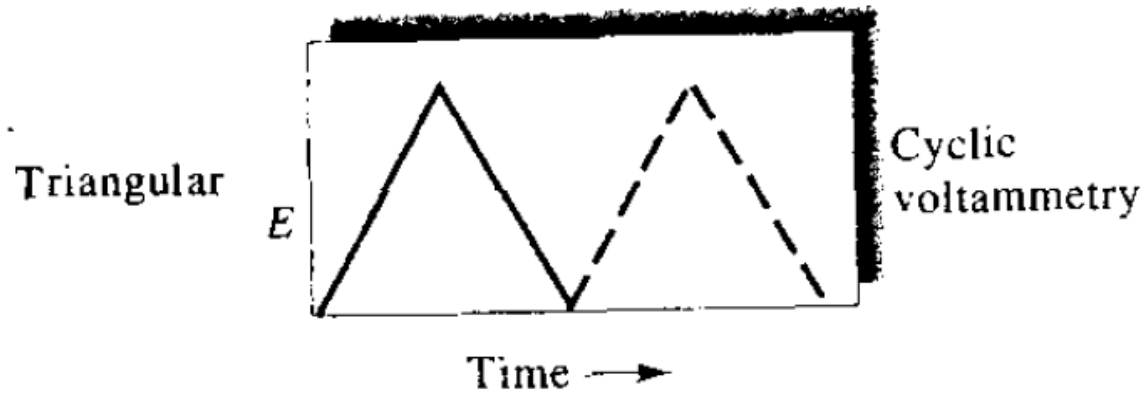

Figure 2.8. Application of triangular waveform in CV [62].

The current resulting from the applied potential is measured and plotted in the cyclic voltammogram. The x-axis represents a parameter that is imposed on the system (applied potential E) and the y-axis is the response (resulting current I). An illustration and example of CV is shown in the *Figure 2.9.* below:

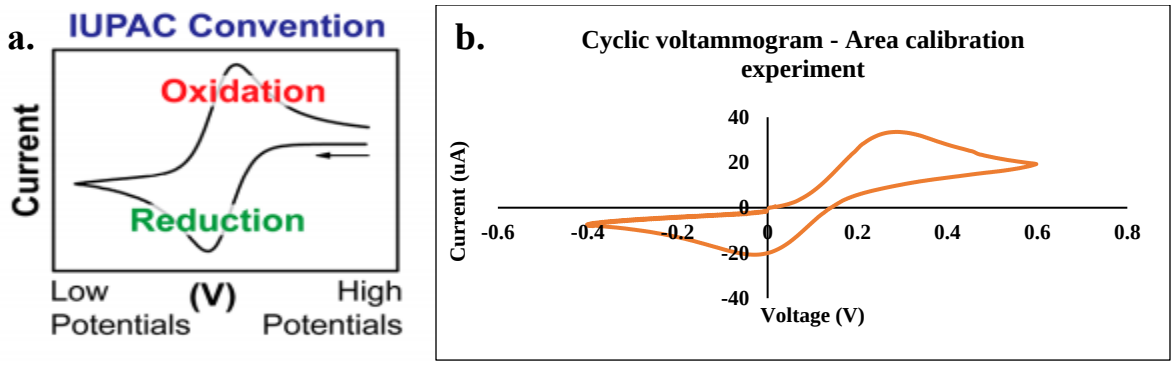

Figure 2.9. Cyclic voltammogram a. Illustration [62] and b. Example CV for an electrolyte of 10ml-0.1M KCl and 5mM $K_4[Fe(CN)_6]$. $3H_2O$ at a scan rate of 50mV s^{-1} [Present study]

A cyclic voltammogram consists of current-potential plot [62]. Current peaks indicate redox reactions at redox potentials. Redox potentials are characteristic of the electro-active species under investigation. For an electrochemically reversible process, the difference between the anodic and cathodic peak potentials, called peak-to-peak separation (ΔEp), is 57 mV at 25 °C (2.22 RT/F), where T is the temperature (K), R is the universal gas constant (8.314 J/K mol) and F is the Faraday's constant (96485 C/mol) [62]. The chemical reversibility is used to denote the stability of the analyte. For an electrochemically reversible electron transfer processes involving freely diffusing redox species, the Randles–Sevcik equation governing the peak current (i_p) is given below,

$$ip = 0.446nFAC^0\left(\frac{nF\upsilon Do}{RT}\right)^{\frac{1}{2}} \quad (2.4)$$

where, n is the number of electrons transferred, F is Faraday's Constant (96,485 C/mole), A (cm^2) is the electrode surface area, Do ($cm^2\ s^{-1}$) is the diffusion coefficient of the oxidized analyte, υ is the scan rate (V/s), R is the gas constant, (8.135 J K^{-1} mol^{-1}), T is temperature (K) and C^0 (mol

cm^{-3}) is the bulk concentration of the analyte. In this study, based on this equation, the value of area for the GCE modified by GQD electrode is determined.

2.5.3 Chronoamperometry

Chronoamperometry is an electrochemical technique used for studying processes like kinetics of chemical reactions, diffusion and adsorption [62]. It is also used for monitoring or detecting events or for determining the reversibility of electrochemical processes. In this technique, a step potential is applied to the electrode and the resulting current vs. time is observed. The potential step applied and the response to the potential step is similar to *Figure 2.10.* shown below.

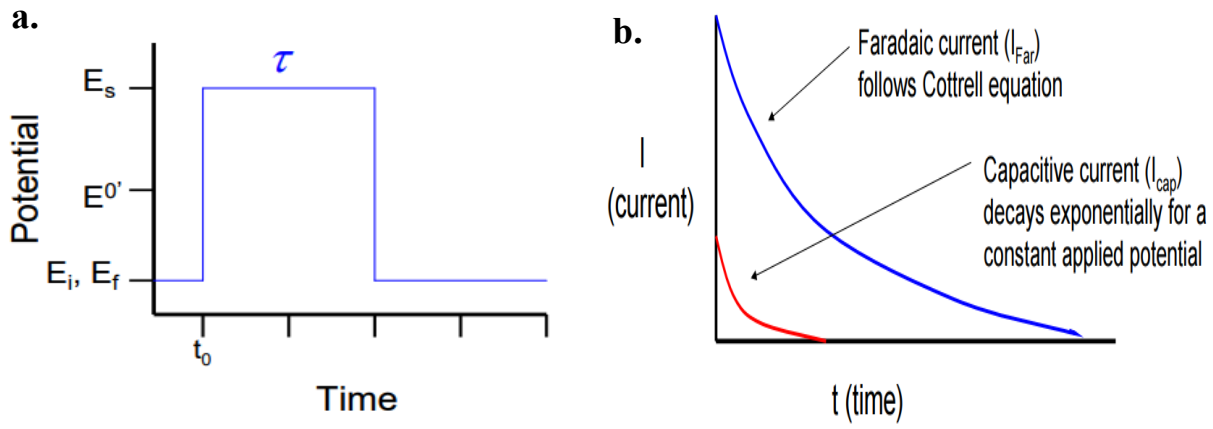

Figure 2.10. a. Potential step application, b. Response to the potential step in chronoamperometry [62].

Usually, a forward potential step is applied from E_i to E_s for a time duration of τ (s) [62]. The reverse potential step is a final potential E_f. Sometimes $E_f = E_i$ (as shown in *Figure 2.11*.), however, E_f may also be set to any other potential value depending on the kind of experiment performed. The response to the potential step is obtained by measuring the current (both the

capacitive and Faradaic current). Capacitive current depends on the charging up of the electrode capacitive layer and Faradaic current depends upon diffusion of the electroactive species. The resulting plot of chronoamperometry experiment consists of a plot of resulting current vs. time similar to *Figure 2.11.* as below.

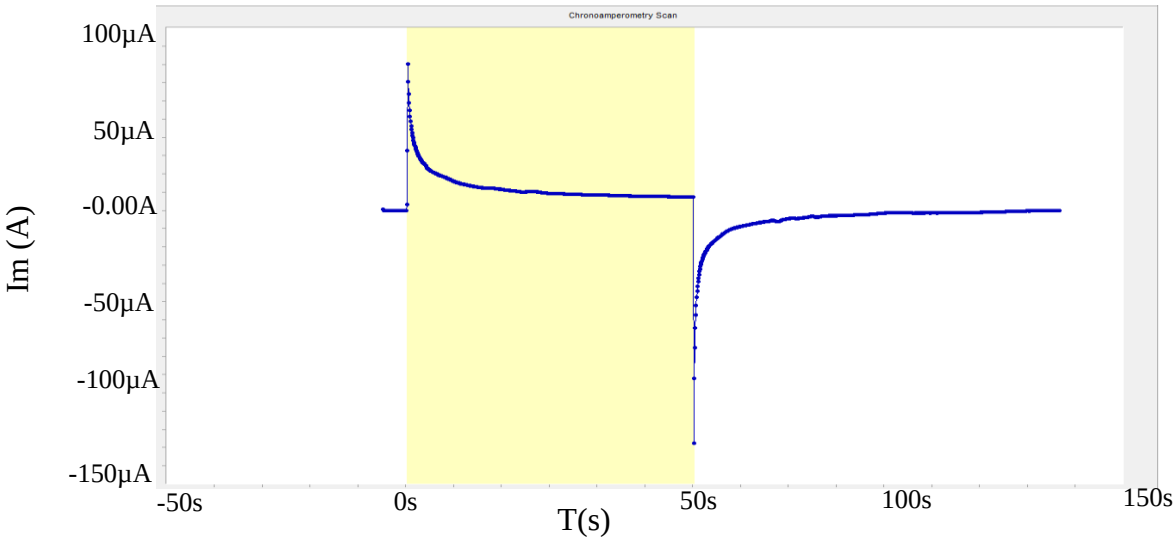

Figure 2.11. Example of chronoamperometry curve for 10ml-0.1M KCl and 5mM $K_4[Fe(CN)_6]. 3H_2O$. [Present study]

Generally, before beginning the experiment, the electrode is held at a potential at which no faradaic process occurs. The potential is then stepped to a value at which a redox reaction occurs. For reactions that are under diffusion control, the current decays with a $t^{1/2}$ and obeys the Cottrell's equation [62]:

$$i(t) = \frac{nFAD^{\left(\frac{1}{2}\right)}C^*}{\pi^{\frac{1}{2}}t^{\frac{1}{2}}} \qquad (2.5)$$

where n is the number of electrons, F is the Faraday constant, A is electrode area, D is the diffusion coefficient of the redox species, C^* is the bulk concentration of the redox species, and t is time. Chronoamperometry allows through the Cottrell's equation (2.5) to measure the value of area for

the GCE modified by GQD electrode and to determine the CP concentration using the GCE modified by GQD electrode.

2.6 Resistance sensor construction

2.6.1 Construction

A new sensor was constructed by using interdigitated finger electrode (5x5 mm) on 0.6 mm thick alumina substrate. The interdigitized arrangement is shown below in *Figure 2.12.*

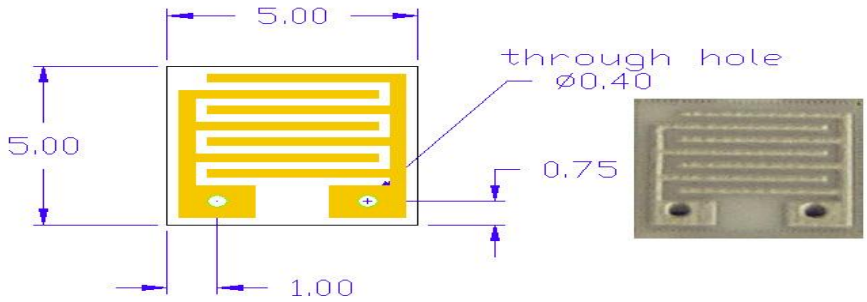

Figure 2.12. Interdigitated sensor (all spacing details are given in mm)

The two holes were used for connecting the insulated copper wires. This required extreme caution to prevent the lead solder to flow into the inter-digitated space. Using 20-40 lead-tin solder, the copper wires were soldered using low wattage soldering gun. The rear side soldering of the sensor and the front view of the sensor after soldering is shown in *Figure 2.13.* below.

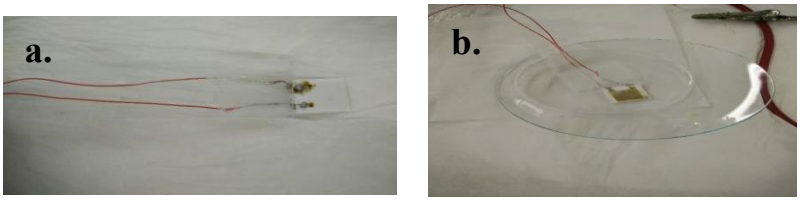

Figure 2.13. a. Rear side soldering and

b. Front view of the sensor mounted on glass slide kept on a watch glass

2.6.2 Procedure for cleaning the sensor

The sensor was first cleaned with water. The use of isopropyl alcohol (IPA) requires caution as alumina adsorbs it, causing functional problems leading to failure of the sensor.

2.6.3 Procedure for depositing the active material

The active material is made of graphene quantum dots (GQD) and ferric chloride. The deposition is done by dropwise addition of two drops of GQD first on the inter digitized space and later by the addition of 50µL drops of 0.1M ferric chloride. The GQD adsorbed ferric chloride strongly. The sensor was air dried for a couple of hours to ensure that a good coating of the active material was obtained.

2.6.4 Procedure for testing the sensor reproducibility

A test chamber and resting chamber were constructed for the measurements that would be conducive to CP. The test chamber and resting chamber are shown in *Figure 2.14. a. and b.* respectively.

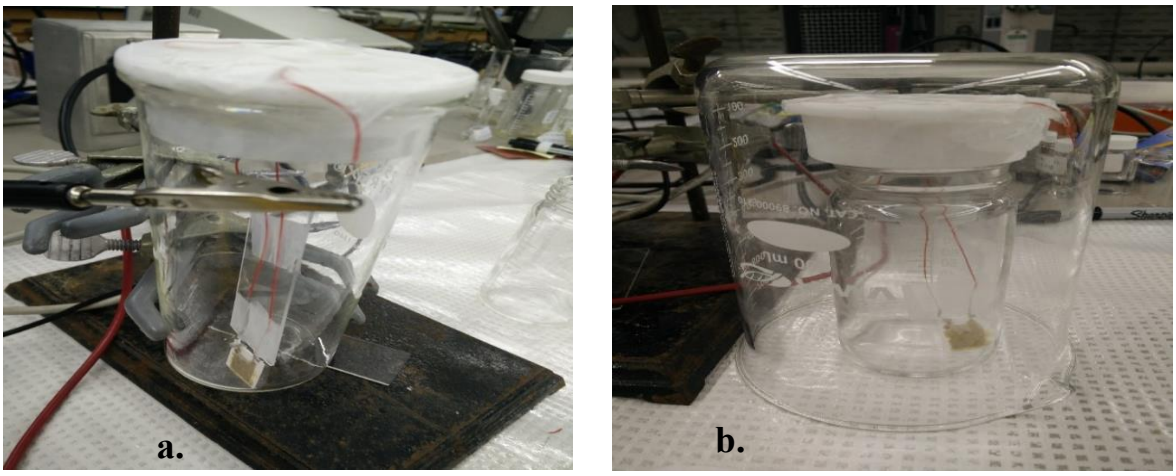

Figure 2.14. a. Sensor testing chamber and b. Sensor resting chamber

The testing chamber was a 250-ml tall form beaker fitted with Teflon cork having holes for injecting the analyte and for inserting the interdigitated sensor. After placing the sensor in the testing chamber, the two wires were taken out through the holes and connected to a digital multimeter that is interfaced with computer through RS230. The meter view software (RadioShack) was used for the measurements. The resting chamber is used to store the sensor. It consists of a 100 ml graduated cylinder into which the sensor was placed. The jar was covered by inverting a 500-ml beaker with the mouth resting flat as shown in *Figure 2.14.b*.

The resistance of the air dried sensor was measured in air and in different solutions containing varying concentrations of only CP and a combination of CP and urea solutions to formulate the methodology for determining CP concentration and for analyzing the effect of urea as an interference.

2.7 Fluorescence spectroscopy

2.7.1 Basic Principle

Fluorescence spectroscopy is based on the principle of photo-luminescence (PL), which is the emission of an absorbed radiant energy in the form of light [60]. Generally, the emitted light is almost of longer wavelength than that of the absorbed radiation. When the emission process occurs very rapidly after excitation ($l0^{-6}$ to 10^{-9} s), the process is defined as fluorescence. A schematic diagram for fluorescence is shown in the *Figure 2.15.* below.

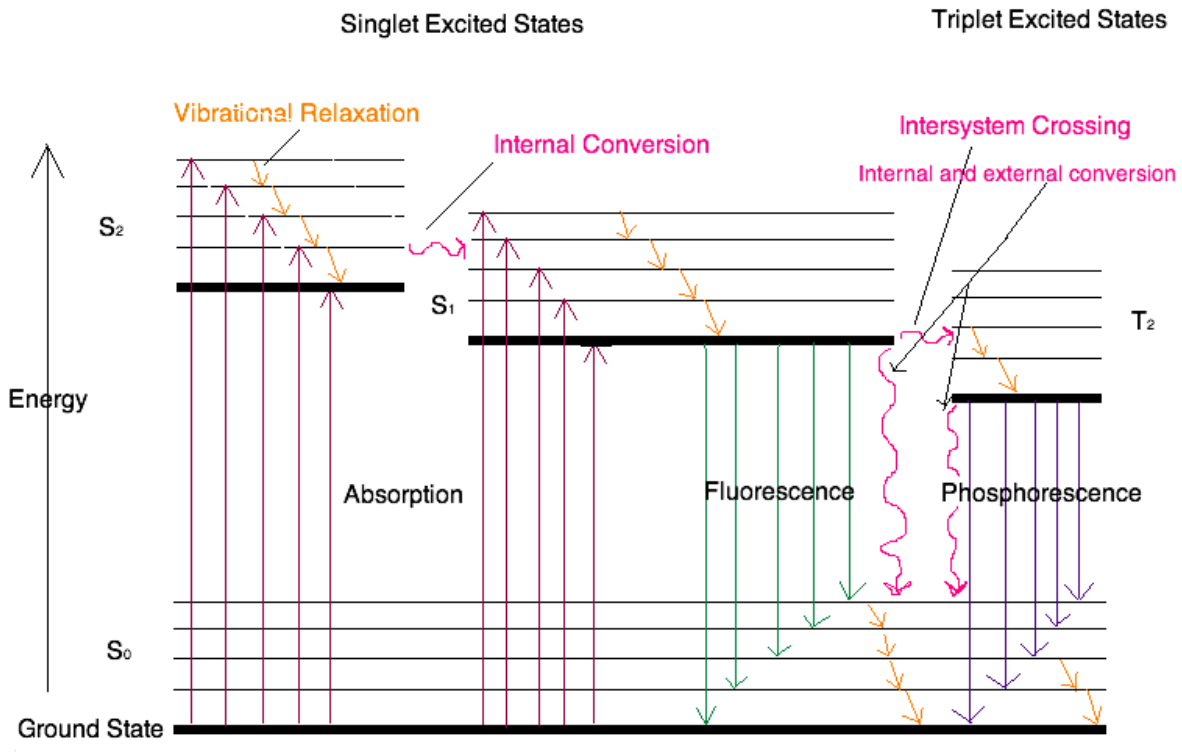

Figure 2.15. The electronic levels and transitions in a PL system [60].

The most important selection rule for all PL systems is that spin/multiplicity must not change during an electronic transition. The equation for multiplicity is given by

$$\text{Multiplicity} = 2S+1$$

where S is the total spin angular momentum.

For paired electrons: S= (-1/2) + (+1/2) =0 => Multiplicity = 1, and

For unpaired electrons: S= (+1/2) + (+1/2) =1 => Multiplicity =3.

In theory, therefore, a singlet ground state species can only transform into a singlet excited state and similarly a triplet ground state into triplet excited states, etc. Fluorescence is the electronic transition from ground state to single state and back. The fluorescence spectrum is obtained by

measuring fluorescence intensity at varying wavelengths while the excitation wavelength is constant. The peak intensity and wavelength are characteristic to the species under observation. Based on the changes in peak wavelength and intensity in the fluorescence spectrum of different samples of study, different inferences can be made.

2.7.2 Experimental set-up

Fluorescence spectroscopy was used in this study to investigate the fluorescence behavior of the solutions of:

1. Different concentrations of ferric ion in a constant concentration (reference sample) of CP, and
2. Different concentrations of ferric ion in a constant concentration (reference sample) of GQD.

The schematic of Horiba Jobin Yvon Fluoromax-4 Fluorimeter and the quartz cuvette in which the fluorescence measurements were taken are shown in *Figure 2.16.* below.

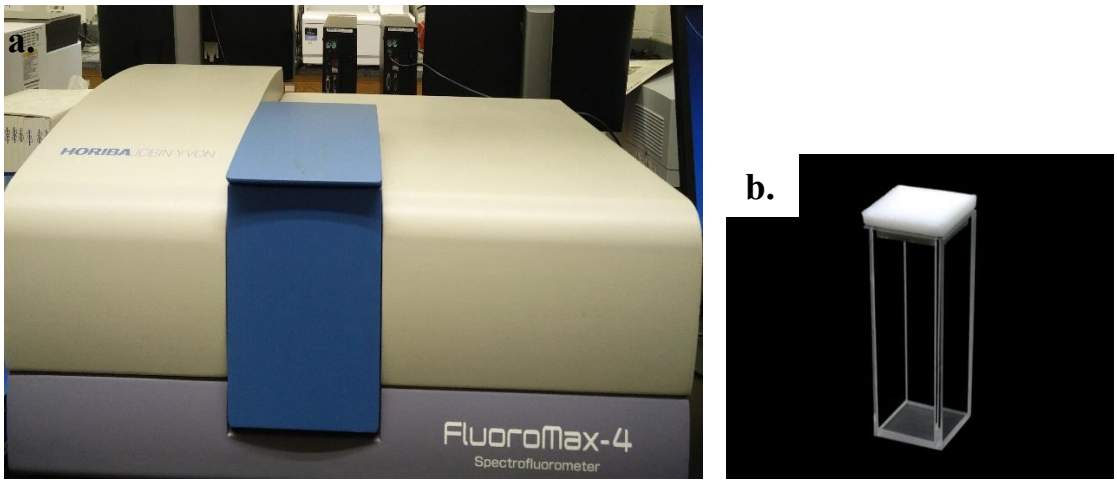

Figure 2.16. a. Horiba Jobin Yvon Fluoromax-4 Fluorimeter and

b. 1cm Quartz cuvette to study fluorescence

A beam with a wavelength varying between 180 and ~800 nm is passed through a solution in a completely transparent cuvette and the light that is emitted from the sample is measured at an angle of 90 degrees. Based on the changes in intensities and wavelengths of peaks seen in fluorescence spectra of different solutions, various inferences are made and presented in section 3.4 of this thesis.

2.8 Fourier Transform Infra-red (FTIR) measurements

2.8.1 Basic Principle

The FTIR spectroscopy is one of the most useful techniques for identifying organic and inorganic chemicals [60] by identifying types of chemical bonds in a molecule due to the infrared absorption spectrum that is like a molecular "fingerprint". The wavelength of light absorbed is characteristic of the type of the chemical bond in the molecule.

The basic principle of FTIR depends on the vibration of molecular bonds at various frequencies. For any given bond, there are several specific frequencies at which it can vibrate [60]. According to quantum mechanics, these frequencies correspond to the ground state (lowest frequency) and several excited states (higher frequencies). The molecular vibration can be increased by exciting the bond by having it absorb light energy. The FTIR experiment uses the principle of exciting the bonds in a molecule by passing infra-red light energy through it. As a result of this, an intensity-vs.-time spectrum is converted into an intensity-vs.-frequency spectrum using a special mathematical function called as the Fourier transform. Based on the wavelengths at which peaks are obtained in the FTIR spectrum, the type of bonds in a molecule are identified.

2.8.2 Experimental set-up

In this study, FTIR was performed for solutions like ferric ion only (ferric chloride), and combination of ferric ion and CP. The schematic of Biorad Excalibur Series FTS 300 on which the FTIR measurements were performed are as shown in the *Figure 2.17*

Figure 2.17 FTIR experimental set up

The background emission spectrum of the IR source (in atmospheric air) is first recorded, followed by the emission spectrum of the IR source with the sample in place. Each FTIR recording comprises of 2000 scans in the range from 4000 cm^{-1} to 300 cm^{-1}. Various inferences made from the absorption spectrum are illustrated in section 3.5.

CHAPTER – 3

RESULTS AND DISCUSSION

3.1 Concentration determination of CP stock solution

Because of very low solubility of CP in water (3000mg/L), the CP solutions whose concentration were calculated by weighing the gram equivalent weight of CP solid could not be considered accurate. The CP solutions showed turbidity. The CP stock solutions were filtered and its concentration was measured by UV-visible absorption spectroscopy.

100ml of 6mM CP solution was made by weighing 0.198g of CP and diluting it to 100ml with distilled water. The solution was filtered and 0.1ml of the filtered solution was diluted to 10ml with distilled water, i.e, the filtered solution was diluted by a hundred times. The UV-visible absorption spectrum was recorded for the diluted filtered CP solution with respect to water as the reference sample. The UV-visible absorption spectrum and the wavelengths at which peaks were obtained are shown in *Figure 3.1.*

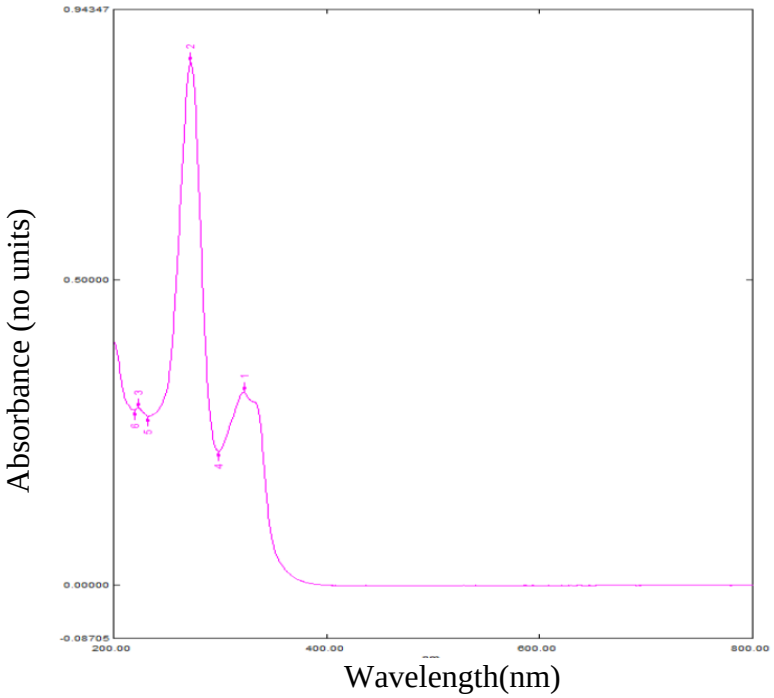

Peak Wavelength (nm)	Absorbance (no units)
322.5	0.31622
298.5	0.21927
272.5	0.85759
232.5	0.27661
223	0.29071
220	0.28691

Figure 3.1. UV-visible absorption spectrum and b. Absorbance and peak wavelengths for diluted filtered CP stock solution

By using Beer Lambert's law for the absorbance at the peak of wavelength 272nm, the unknown concentration of CP was found as follows [60] ,

A=€cl

where, A -> Absorbance (0.85759)

€-> wavelength-dependent molar absorptivity coefficient with units of M^{-1} cm^{-1}

For CP, € = ($9x10^4$) [60],

c->analyte concentration with units of mol L^{-1} or M (Unknown)

l-> Path length (1 cm)

ie 0.85759 = ($9x10^4$ L mol^{-1} cm^{-1})*c* (1cm)

c= $9.52*10^{-6}$ mol L^{-1} or M

c=9.52 µM

This is the concentration of the hundred-time diluted solution of filtered CP solution. The concentration of filtered CP stock solution is Conc $_{\text{filtered solution}}$ = 9.52uM *10/0.1= **952uM**. This stock solution of CP was used and diluted to make other CP solutions subsequently used in the study.

3.2 Electrochemical results

3.2.1 Area calibration of GCE modified by GQD

The GCE modified by GQD was made by coating the electrode surface of bare GCE with 30µL of electrochemically synthesized GQD and drying it in the oven at a temperature of 75ºC for about an hour. The GCE modified by GQD made by this procedure is shown in *Figure 3.2.*

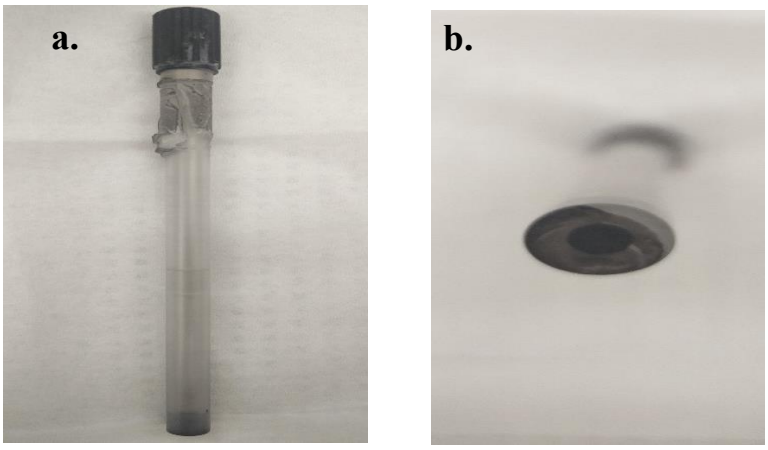

Figure 3.2. GCE modified by GQD a. Longitudinal view b. Cross-sectional view

The area calibration of GQD electrode was electrochemically done to ensure that the entire geometrical area of unmodified GCE (Diameter = 0.3 cm, radius = 0.15 cm and area = 0.071 cm^2) became electrochemically active through the use of GQD.

The electrolyte used in this process was 10ml of 0.1M KCl and 5mM $K_4[Fe(CN)_6]$. $3H_2O$. Cyclic voltammetry was performed by scanning the system between the voltage range of 0.6 V and -0.4 V at a scan rate of 50mV s^{-1}. The cyclic voltammogram obtained is shown in *Figure 3.3.*

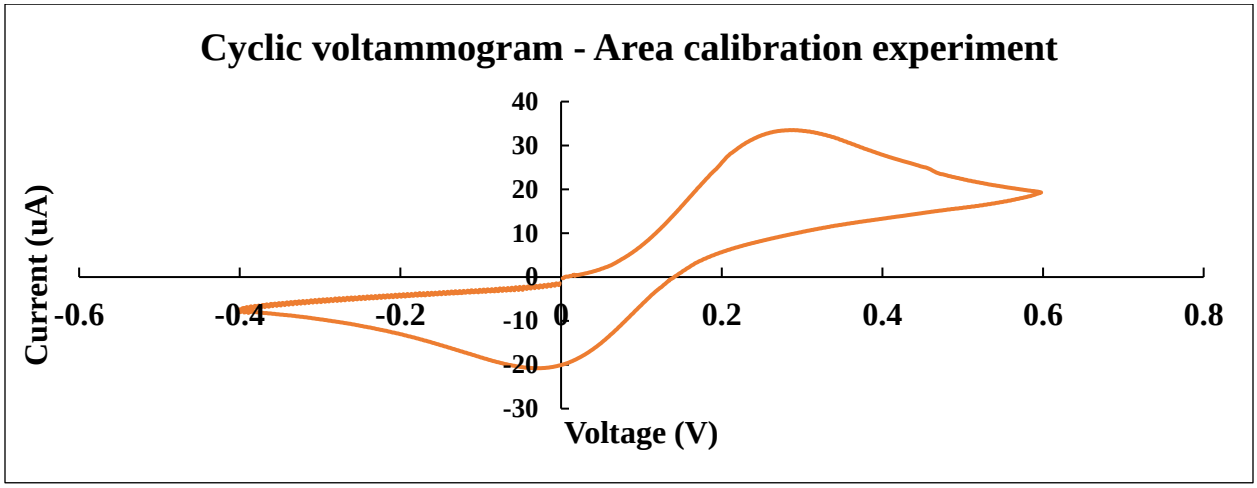

Figure 3.3. Cyclic voltammogram for an electrolyte of 10ml-0.1M KCl and 5mM $K_4[Fe(CN)_6]$. $3H_2O$ at a scan rate of 50mV s^{-1}.

The peak voltage and currents for the above cyclic voltammogram are Epa=0.273 V, Ipa = 33.7 µA and Epc = -0.022 V, Ipc = -20.74 µA, and this gives ΔEp = 0.295V. By reports in the literature, it is known that if the peak separation voltage, ΔEp > 60mV, then the reaction is classified as a quasi-reversible reaction [60], where current is controlled by both the charge transfer and mass transport. The peak current for a quasi-reversible reaction is given by [60],

$$ip = (2.99 * 10^5)n(\propto na)^{(\frac{1}{2})} ACD^{\frac{1}{2}}\nu^{\frac{1}{2}} \quad (3.1)$$

Because of factors like α, the transfer coefficient and n_a, the number of electrons involved in the charge-transfer step, are difficult to be determined, the area of the GQD electrode using cyclic voltammetry experiment became difficult to calculate. However, area calibration was done using chronoamperometry, where the equation of peak current is the same for reversible and quasi-

reversible systems as long as the experiment is carried out in the diffusion limit range of the electro-active species [60].

The chronoamperometry experiment was done by applying a forward potential step from 0V to 0.4 V for 60 s. The reverse potential step had a final potential of -0.2 V which was applied for 120s. The chronoamperometry curve obtained is given in the *Figure 3.4.* below.

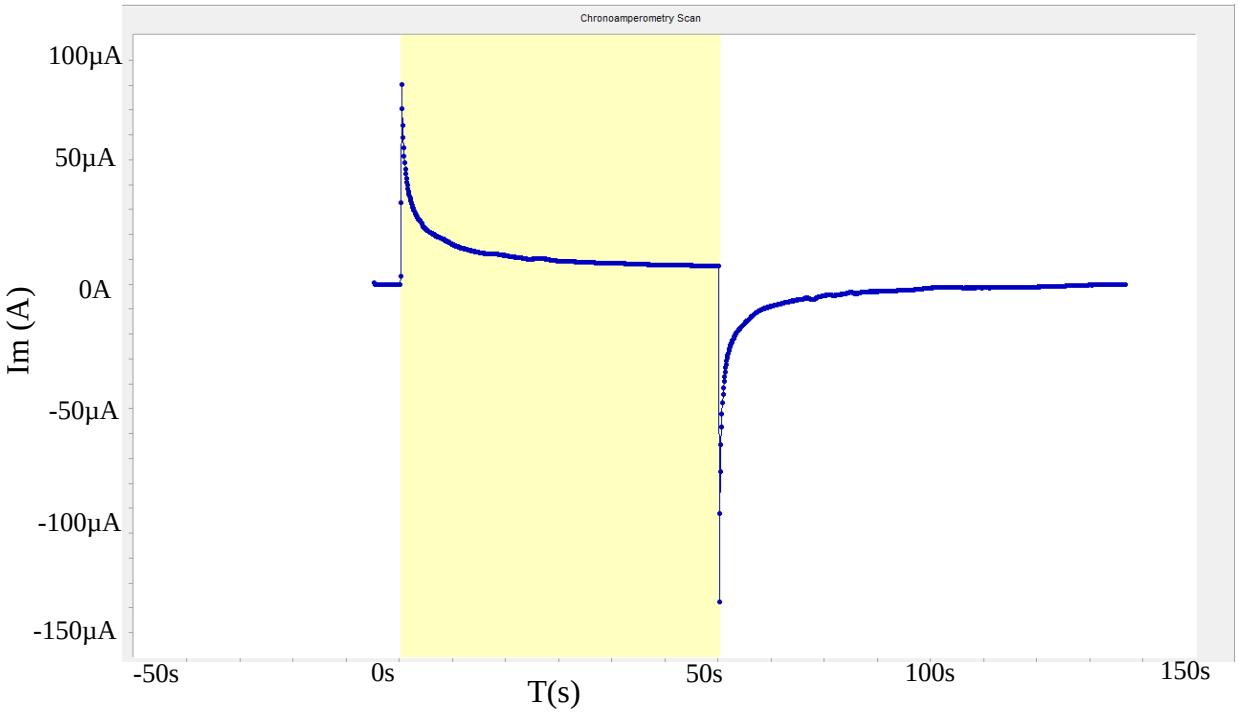

Figure 3.4. Chronoamperometry curve for 10ml-0.1M KCl and 5mM $K_4[Fe(CN)_6]$. $3H_2O$.

The range in which the potential step was applied was in the range of the diffusion limit of ferric ion species. Hence the equation of peak current is given by the Cottrell equation [60],

$$i(t) = \frac{nFAD^{\left(\frac{1}{2}\right)}C^*}{\pi^{\frac{1}{2}}t^{\frac{1}{2}}} \qquad (3.2)$$

where, i(t) is the decay of current with time following a $t^{1/2}$ decay, n is the number of electrons (1 electron), F is the Faraday constant (96500 C mol^{-1}), A is electrode area (unknown cm^2), D is the

diffusion coefficient of the redox species (cm s^{-1}), C^* is the bulk concentration of the redox species (10^{-3} moles cm^{-3}), and t is time (s) [60]. The plot of i(t) vs $t^{-1/2}$ for the data obtained by the chronoamperometry curve is shown in *Figure 3.5.*

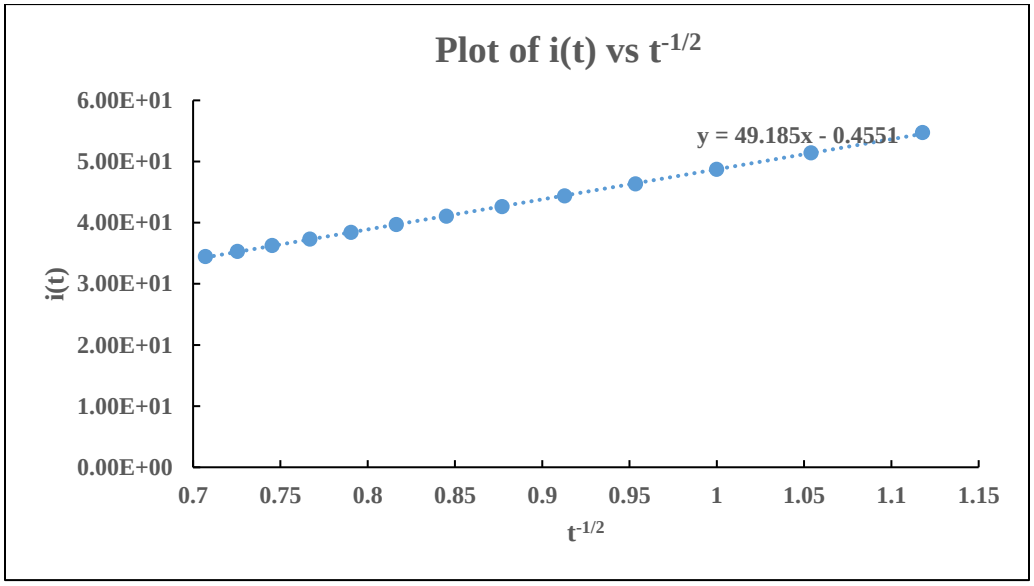

Figure 3.5. Plot of i(t) vs $t^{-1/2}$.

The slope of this plot equals $\frac{nFAD^{\left(\frac{1}{2}\right)}C^*}{\pi^{\frac{1}{2}}}$, where the slope = 49.185 µA, n = 1 electron, F = 96485 C mol^{-1}, D = 6.5*10^{-6} cm s^{-1}, C^* = 5mM. All values except A are known, and hence calculation of A results in 0.0708 cm^2 (which is almost equal to the geometrical area of unmodified GCE, A=0.071cm^2). This result proves that the entire geometrical area of unmodified GCE became electrochemically active in the GCE modified by GQD. The results of different electrochemical experiments performed using both unmodified GCE and GCE modified by GQD for this study are presented in the following sections.

3.2.2 DPV analysis of CP with ferric ion

The DPV experiment was performed using an electrolyte of 10ml - 0.1M Na_2SO_4 (pH=6.4) containing 5mM ferric ion in the form of 5mM $FeCl_3$ solution. Both the unmodified GCE and GCE modified by GQD electrodes were used to study the effect of CP on ferric ion. DPV was performed by scanning the system from an initial voltage of 0.8 V to a final voltage of 0 V by applying fixed magnitude pulses, each of 20mV pulse size, 0.1s pulse time and 1s sample time.

3.2.2.1 Using unmodified GCE

The differential pulse voltammogram of 5mM ferric ion obtained by using unmodified GCE is shown in *Figure 3.6.* below.

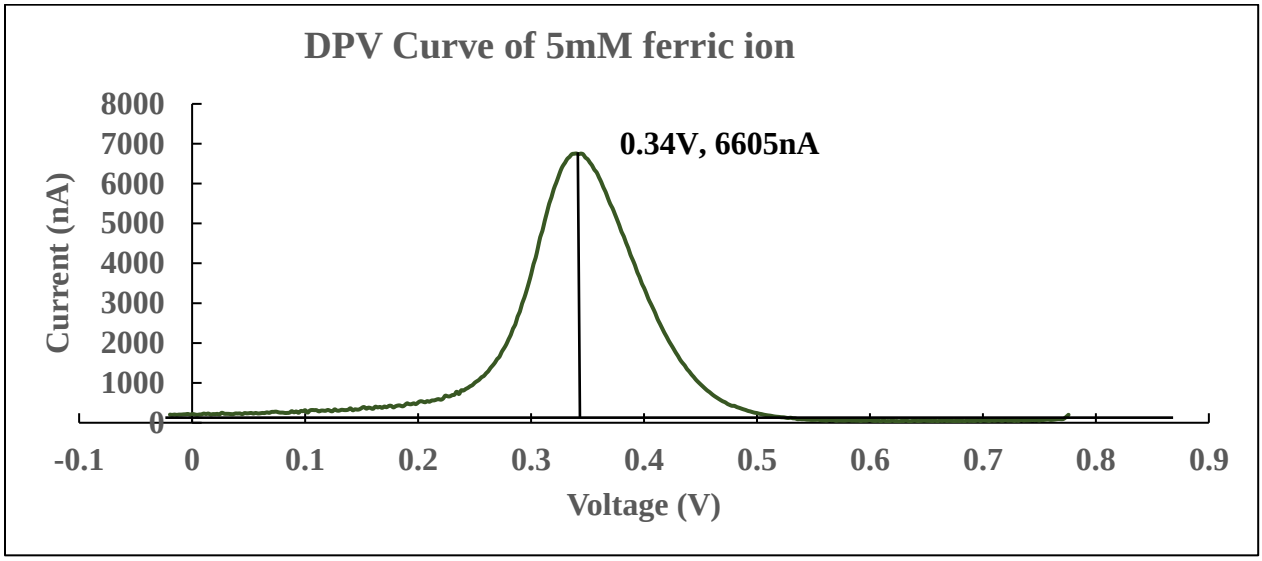

Figure 3.6. DPV curve for 5mM ferric ion using unmodified GCE.

As seen from *Figure 3.6.*, DPV of ferric ion in sodium sulfate supporting electrolyte (pH=6.4) showed a single well defined reduction peak at 0.34 V. Previously reported literature studies indicate that the reduction peak of ferric ion occurs at 0.34 V [64]. This confirmed the presence of ferric ion species, with the concentration of 5mM corresponding to 6605 nA peak

current. When CP was added to the system containing 5mM ferric ion, the peak current corresponding to ferric ion at 0.34 V decreased and additional peaks appeared at Ep^{I} = 0.20 V, Ep^{II} = 0.050 V and Ep^{III} = -0.085 V. The appearance of three different peaks upon addition of CP can be seen in *Figure 3.7.* below.

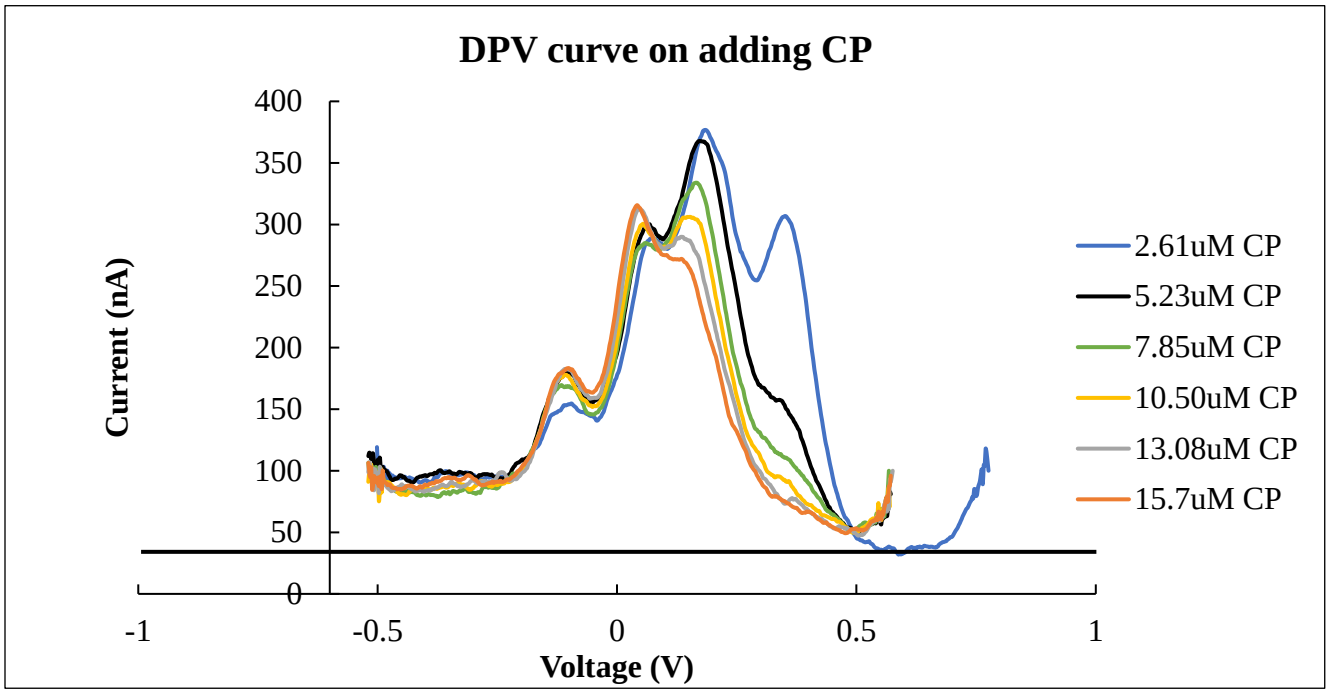

Figure 3.7. DPV curve upon addition of CP to ferric ion.

It is seen from *Figure 3.7.* that, the peak current at 0.34 V corresponding to ferric ion continuously decreases with increasing addition of CP. The three peaks are attributed to the reduction of the bound CP with ferric ion because CP exists in the pH range of 6-9 as an anionic species as shown in *Figure 3.8.* and binds with the positively charged ferric ion.

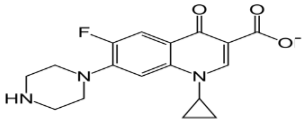

Figure 3.8. Structure of CP anion in pH range of 6-9 [65]

The reaction governing the binding of anionic CP to positively charged ferric ion is given below

$$Fe^{3+} + 3\ CP^{-} \rightarrow [Fe^{3+} - (CP)_3] \quad (3.3)$$

This reaction proceeds in three single steps as in any other complexation by successive neutralization charges of ferric ion. Consequently, the ferric ion peak current is reduced depending on the complete binding. The three successive peaks represent the three stages of the reduction of the ferric ion bound CP species in solution. The ferric ion reduction current decreases with increasing concentration of CP, thus giving rise to a methodology to sense and to electrochemically measure the concentration of CP as explained in section 3.2.3.1.

3.2.2.2 Using GCE modified by GQD

The differential pulse voltammogram of 5mM ferric ion obtained by using GCE modified by GQD is shown in *Figure 3.9.* below.

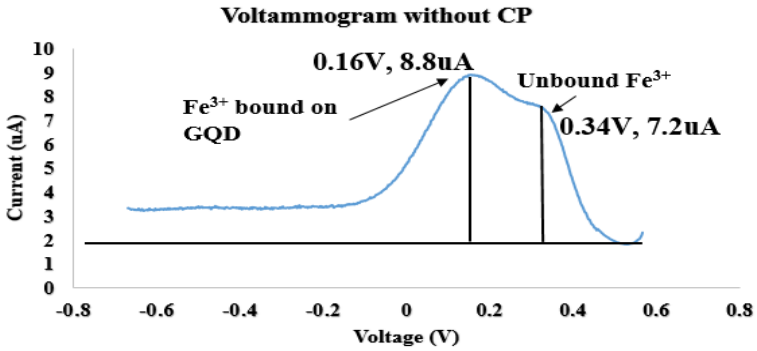

Figure 3.9. DPV curve for 5mM ferric ion using GCE modified by GQD.

As seen from *Figure 3.9.*, DPV of ferric ion in sodium sulfate supporting electrolyte showed two peaks 0.34 V which indicated the unbound ferric ion [64] and at 0.16V which indicated the ferric ion adsorbed and bound on GQD electrode. The unbound 5mM ferric ion had a peak

current of 7.2 µA significantly larger than that obtained using unmodified GCE. When CP was added to the system containing 5mM ferric ion, the peak potential of the peak obtained shifted to E_p = 0.20V as seen below in *Figure 3.10.*

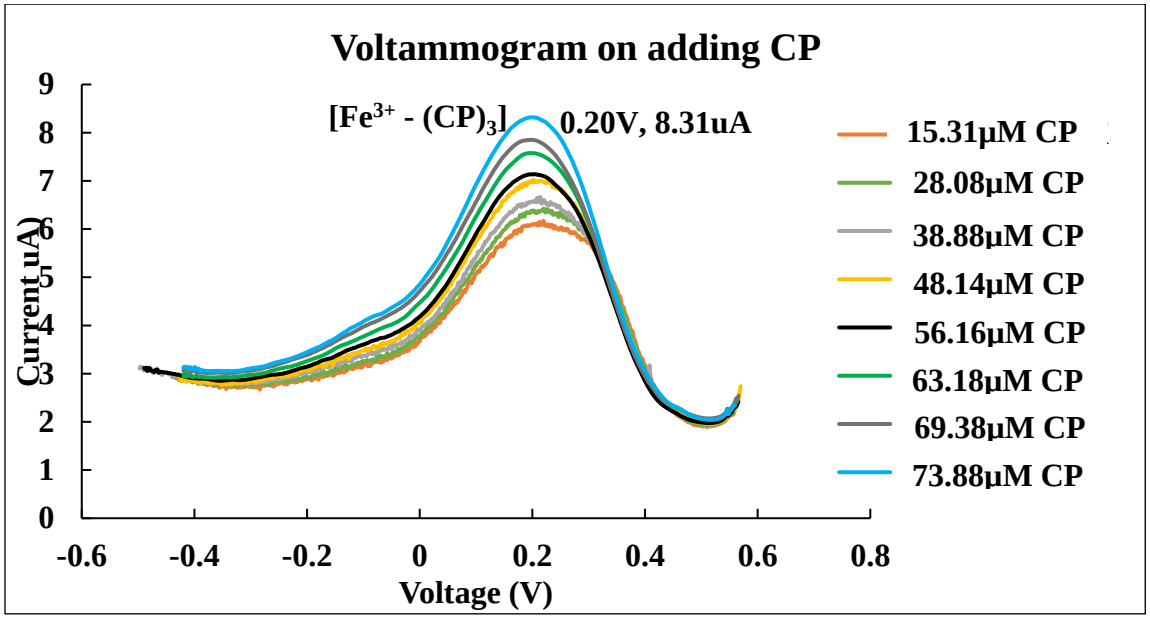

Figure 3.10. DPV curve upon addition of CP to ferric ion.

From *Figure 3.10.*, it is seen that, the peak current at 0.20 V continuously increases with increasing addition of CP. The peak at 0.20V is attributed to the reduction of the bound CP with ferric ion. Due to the large surface area of GQD, the three successive neutralization of charges of ferric ion as observed in unmodified GCE takes place as a single step when GCE is modified by GQD. Hence, the binding is observed as a single peak at 0.20 V which is attributed to $[Fe^{3+} - (CP^{-})_3]$. The reduction peak current at 0.20V successively increases with successive additions of CP. This gives rise to a methodology to sense and to electrochemically measure the concentration of CP using GCE modified by GQD as explained in section 3.2.3.3.

3.2.3 CP concentration measurement by DPV

3.2.3.1 Using unmodified GCE

As seen in section 3.2.2.1, when unmodified GCE is used to study CP electrochemically, the ferric ion reduction current decreases with increasing concentration of CP. This observation has helped to develop an approach to sense CP electrochemically by DPV using unmodified GCE. The calibration curve for the sensor has been obtained by measuring the value of reduction peak current of ferric ion with additions of CP. The *Table 3.1* below indicates the value of reduction peak current of ferric ion and the *Figure 3.11.* below shows the plot of *Table 3.1.*

Table 3.1. Calibration Data for the Sensor with ferric ion using unmodified GCE

CP Concentration (µM)	**Fe^{3+} Peak current (nA)**
2.61	253.66
5.23	109.26
7.85	61.56
10.50	43.1
13.08	22.47
15.7	20.11

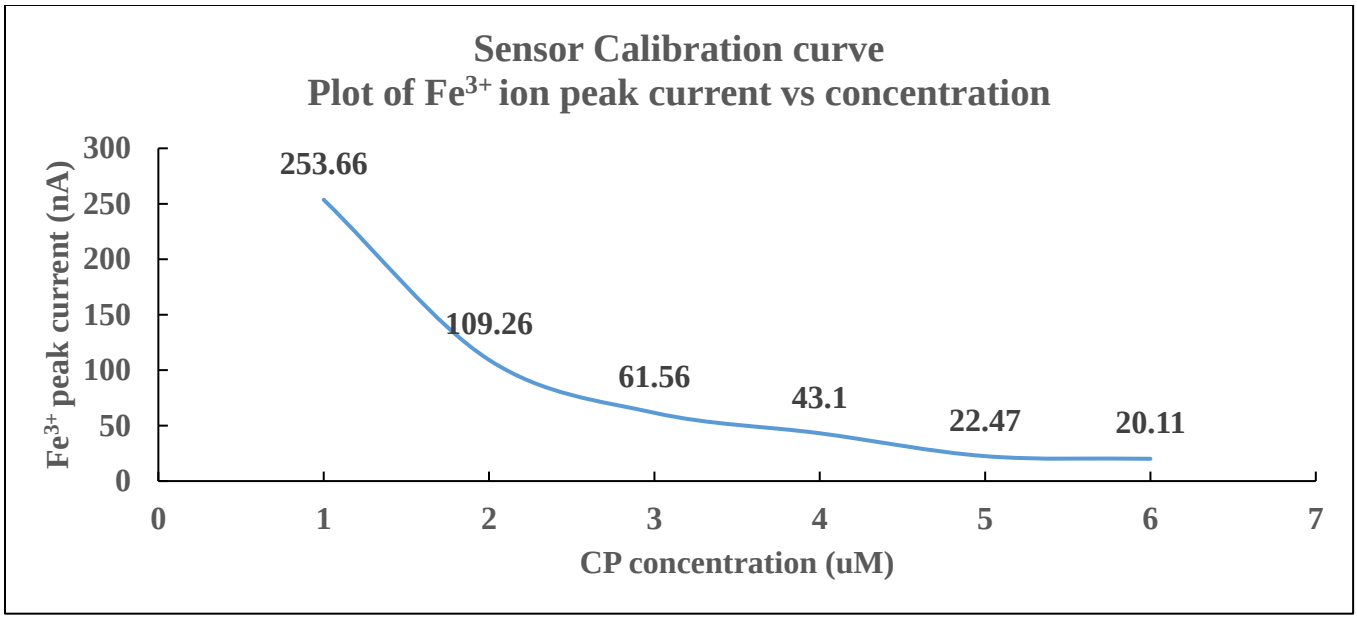

Figure 3.11. Calibration curve for CP sensor using unmodified GCE.

Using this calibration curve, if any sample solution of unknown CP concentration is given, its value can be electrochemically determined by measuring the reduction peak current of ferric ion by DPV using unmodified GCE. The sensitivity of this technique was about 55nA/µM.

3.2.3.2 Using GCE modified by GQD

As seen in section 3.2.2.2, when GCE modified by GQD is used to study CP electrochemically, the ferric ion reduction current increases with increasing concentration of CP. This observation has helped to develop an approach to sense CP electrochemically by DPV using GCE modified by GQD. The calibration curve for the sensor has been obtained by measuring the peak current of [Fe^{3+} - $(CP^{-})_3$] with additions of CP. The *Table 3.2* below indicates the value of the peak current of [Fe^{3+} - $(CP^{-})_3$] and the *Figure 3.12.* below shows the plot of *Table 3.2.*

Table 3.2 Calibration Data for the Sensor with $[Fe^{3+} - (CP^{-})_3]$ using GCE modified by GQD.

CP Concentration (µM)	Peak current (µA)
15.31	4.346
28.08	4.531
38.88	4.556
48.14	5.113
56.16	5.13
63.18	5.736
69.38	5.831
73.88	6.298

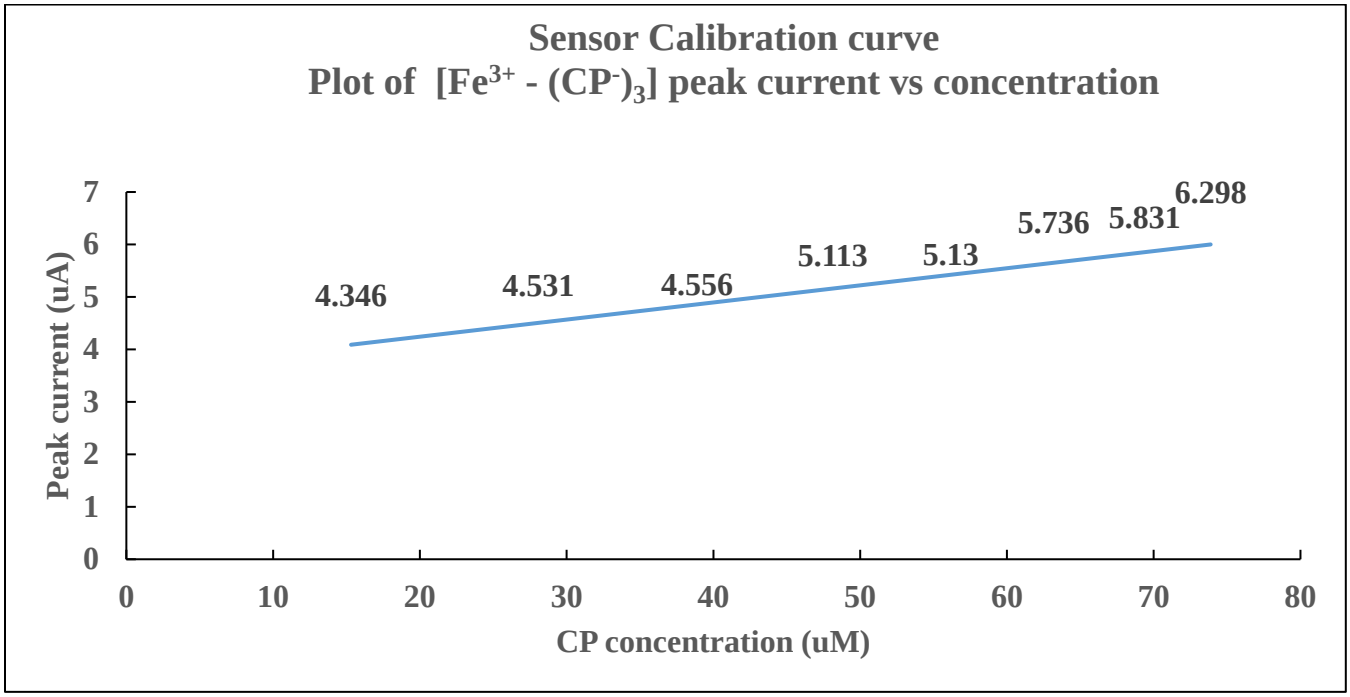

Figure 3.12. Calibration curve for CP sensor using GCE modified by GQD.

Using this calibration curve, if any sample solution of unknown CP concentration is given, its value can be electrochemically determined by measuring the reduction peak current of $[Fe^{3+} - (CP^{-})_3]$ by DPV using GCE modified by GQD. The sensitivity of this technique was observed to be about 243 nA/µM.

3.2.4 CP concentration measurement by Chronoamperometry

The Chronoamperometry experiment was performed using an electrolyte of 10ml - 0.1M Na_2SO_4 (pH=6.4) containing 5mM ferric ion in the form of 5mM $FeCl_3$ solution. For this experiment, GCE modified by GQD electrode was used to study the effect of CP on ferric ion. The chronoamperometry experiment was done by applying a forward potential step from 0.8 V to 0.4 V for 60 s. The reverse potential step had a final potential of 0.6 V which was applied for 60s. The chronoamperometry curve obtained is given in the *Figure 3.13.*.

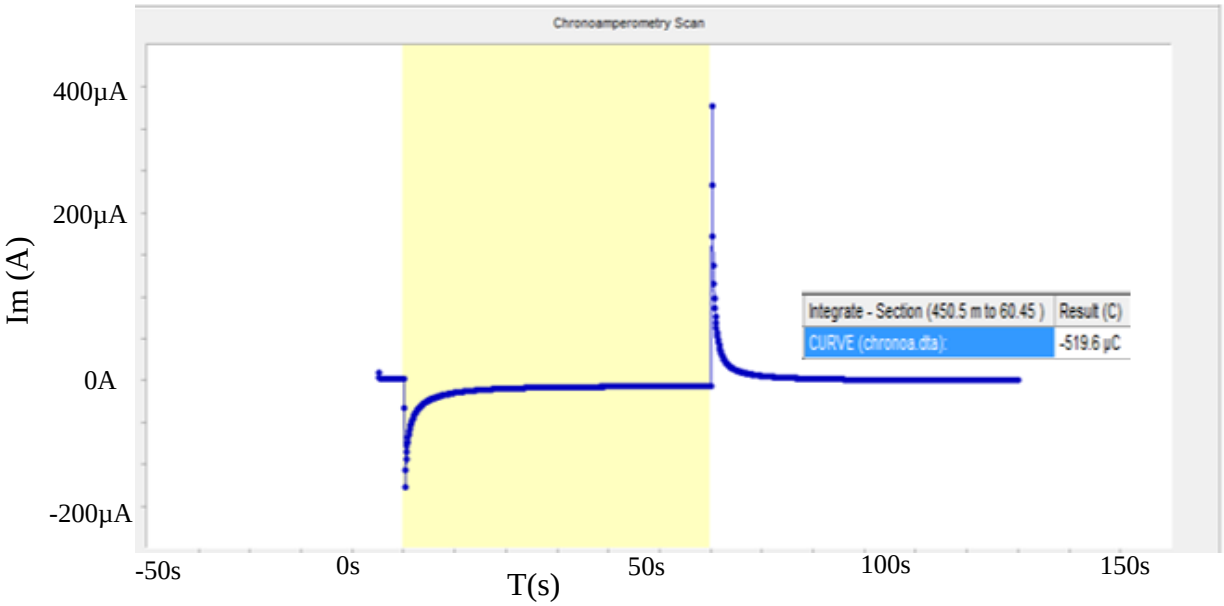

Figure 3.13. Chronoamperometry curve for 10ml - 0.1M Na_2SO_4 containing 5mM ferric ion

As seen from *Figure 3.13.*, the value of total integrated coulombic charge obtained for 5mM ferric ion was 519.6µC. When CP was added to the system containing 5mM ferric ion, the value of total integrated coulombic charge continuously decreased with increasing concentrations of CP.

Table 3.3 and the *Figure 3.14.* indicate the continuous decrease in the values of total integrated coulombic charge with successive additions of CP.

Table 3.3 Decrease in the total integrated coulomb charge with increasing CP concentration

CP Concentration	**Integrated Coulomb (uC)** **On GQD electrode**
0	519.6
0.7	301.0
1.32	227.3
1.89	132.3

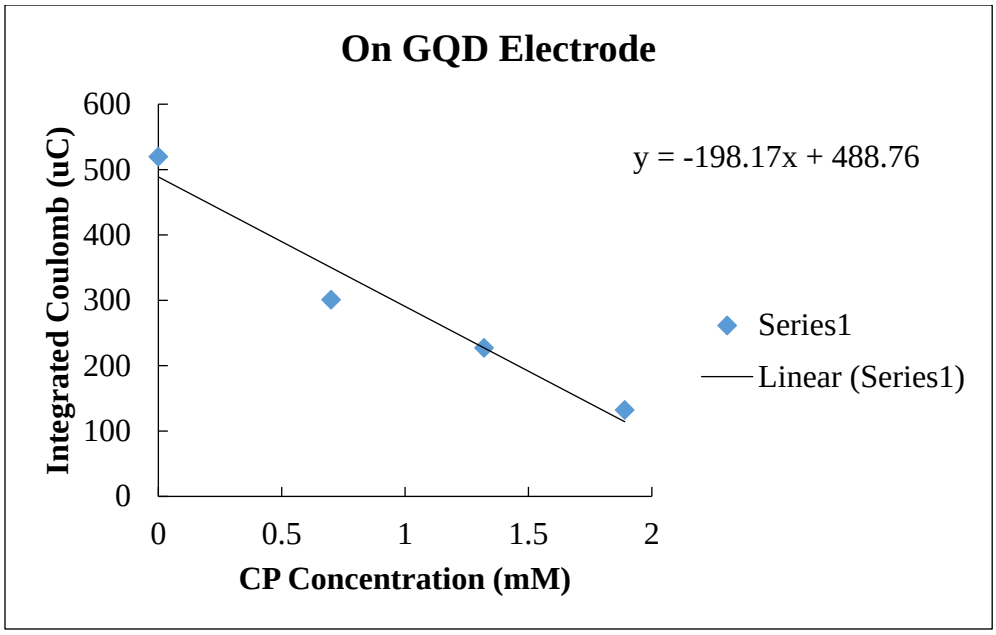

Figure 3.14. Calibration curve for CP sensor by chronoamperometry using GCE modified by GQD

As seen from *Table 3.3* and *Figure 3.14*, the total integrated coulombic charge decreases with increasing CP concentration. This decrease is attributed to the decrease in the total charge contributed by the ferric ion to the system. The decrease in the ferric ion coulombic charge is due to the decrease in ferric ion concentration because of the formation of $[Fe^{3+} - (CP^{-})_3]$. That is, the tendency to form $[Fe^{3+} - (CP^{-})_3]$ increases with increase in CP concentration. This leads to the decrease in the total integrated coulombic charge. This observation has helped to develop an approach to sense CP electrochemically by chronoamperometry using GCE modified by GQD. The calibration curve for the sensor shown in *Figure 3.14.* was obtained by measuring the value of total integrated coulombic charge of $[Fe^{3+} - (CP^{-})_3]$ with additions of CP.

Using this calibration curve, if any sample solution of unknown CP concentration is given, its value can be electrochemically determined by measuring the total integrated coulombic charge of $[Fe^{3+} - (CP^{-})_3]$ by chronoamperometry using GCE modified by GQD.

3.2.5 Effect of pH in CP determination

To study the effect of pH on the measurement of CP concentration, the DPV experiment was performed using an electrolyte of 10ml – 0.1M Na_2SO_4 and acetate buffer (pH=5.6) containing 1.2mM ferric ion in the form of 1.2mM $FeCl_3$ solution. Three different concentrations (2.64µM, 4.4µM and 6.09µM) of CP solutions were added to the system containing 1.2mM ferric ion. DPV was performed by scanning the system from an initial voltage of 0.6 V to a final voltage of -0.4 V by applying fixed magnitude pulses, each of 20mV pulse size, 0.1s pulse time and 1s sample time. The differential pulse voltammogram of 1.2mM ferric ion obtained is shown in *Figure 3.15.* The DPV curve obtained when various CP concentrations were added to the system is shown in *Figure 3.16.*

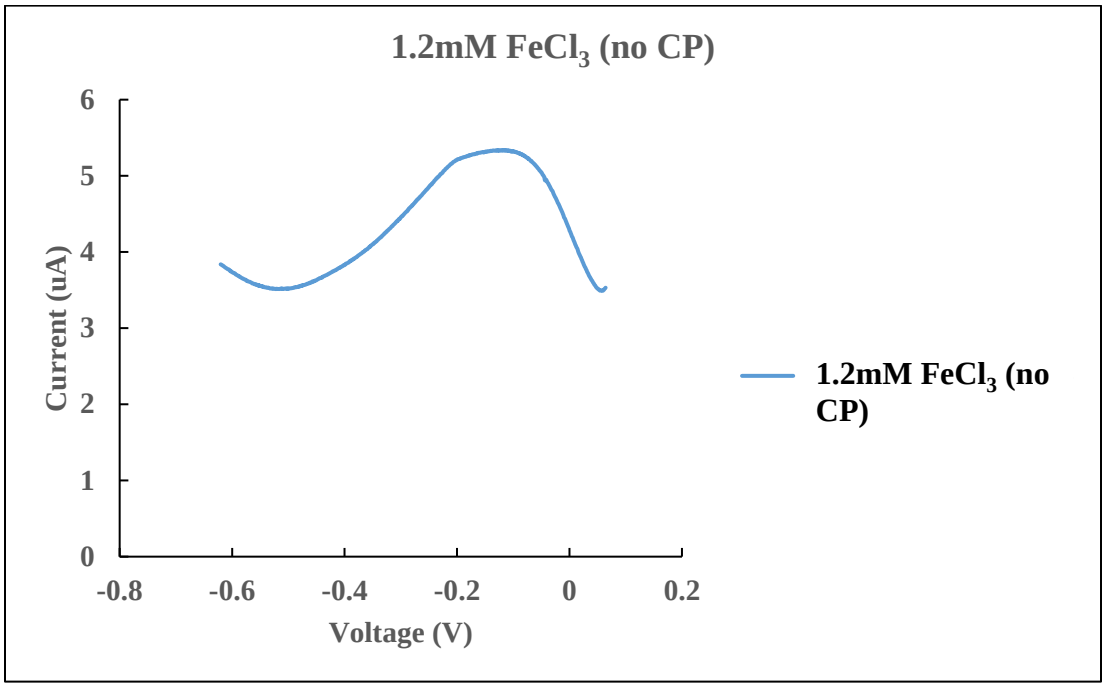

Figure 3.15. DPV curve for 1.2mM ferric ion in electrolyte of pH 5.6

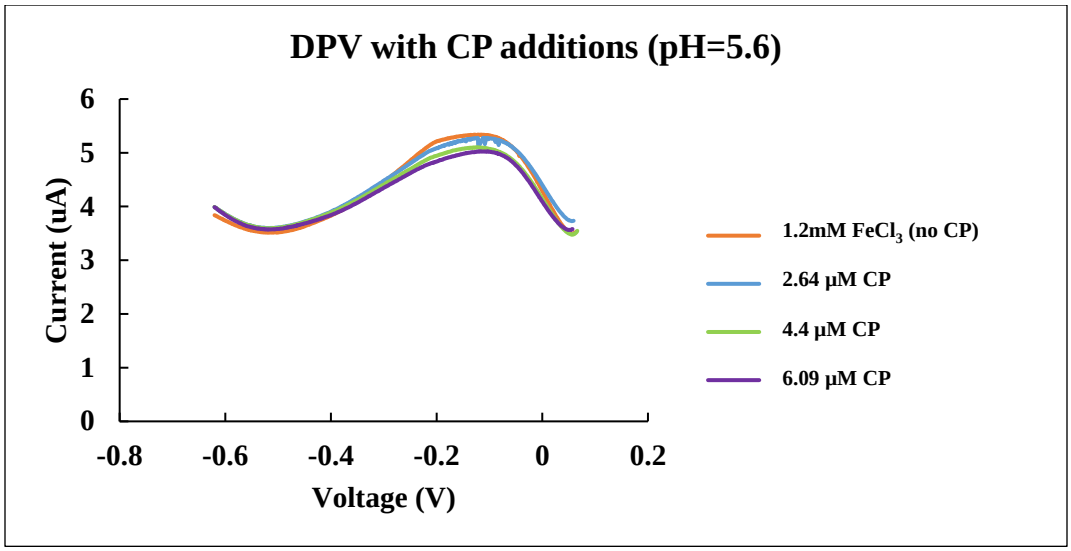

Figure 3.16. DPV curve upon addition of CP to ferric ion.

It is seen from *Figure 3.15.* and *Figure 3.16.*, that the peak of the DPV curves is at -0.12V corresponding to the reduction of ferrous hydroxide and not due to the reduction of ferric ion occurs at 0.34 V [64]. The presence of hydroxide in this pH range affects the binding of CP to ferric ion. Hence, the pH range affects the measurement of CP while using ferric ion as the probe. That is, the presence of hydroxide in this pH range affects the ability of ferric ion to bind to the anionic species of CP as discussed in section 3.2.2.

Hence, it is desirable to carry out the electrochemical measurement of CP concentrations by DPV and chronoamperometry in the pH range of 6-7 and to avoid other pH ranges for getting accurate results.

3.3 Fluorescence measurements as a support of binding

Fluorescence measurements were carried out to demonstrate that there is interaction between Fe^{3+} and CP as well as to indicate the binding of Fe^{3+} to GQD. The experiments were carried with the following solutions:

1. Different concentrations of ferric ion in a constant concentration (reference sample) of CP, and
2. Different concentrations of ferric ion in a constant concentration (reference sample) of GQD.

An excitation wavelength of 350 nm was used for sample excitation in these experiments. The fluorescence emission of CP and ferric ion solutions were monitored by scanning the wavelength range from 380 nm to 600 nm. The fluorescence emission of GQD and ferric ion solutions were studied by scanning a wavelength range from 355 nm to 600 nm.

3.3.1 Fluorescence of CP and ferric ion

The reference sample used while studying the fluorescence emission of CP and ferric ion solutions was 24.3 µM CP solution. The fluorescence emission spectra of reference CP sample and different concentrations of ferric ion in a constant CP concentration are shown in *Figures 3.17.* and 3.18 below.

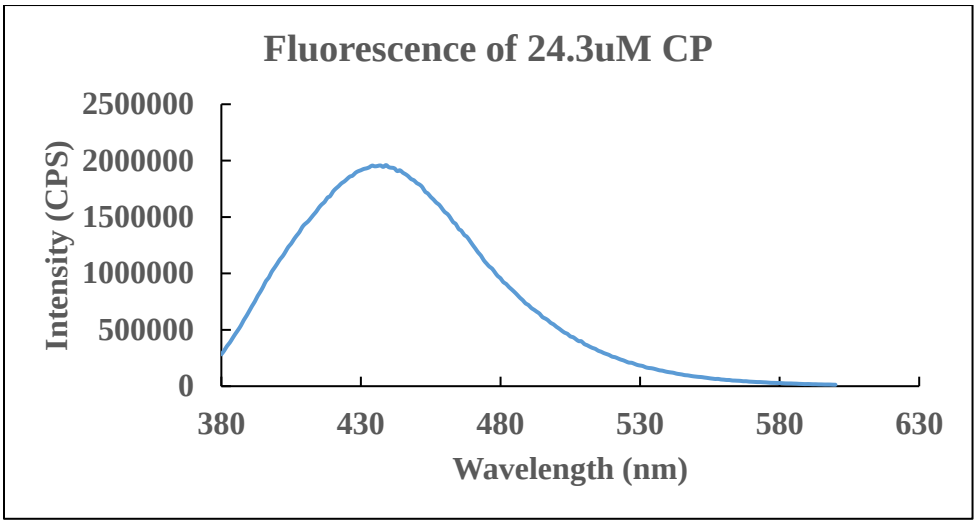

Figure 3.17. Fluorescence emission spectra of 24.3 µM CP, excitation wavelength: 350nm

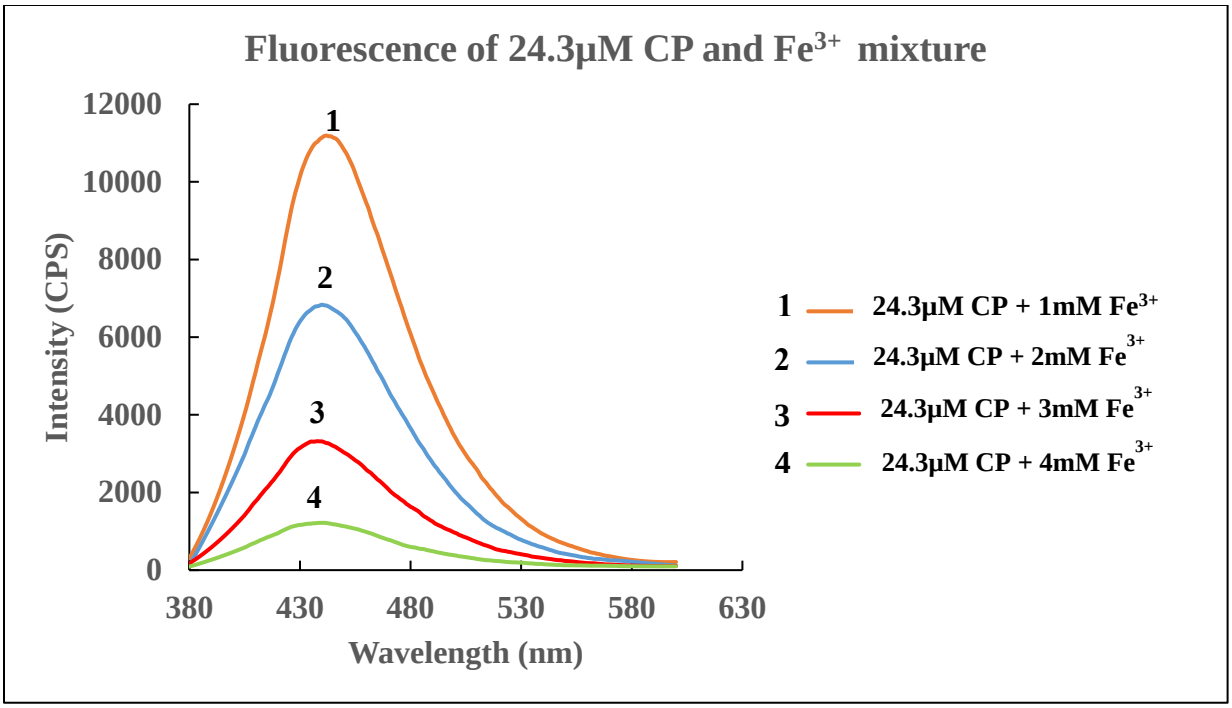

Figure 3.18. Fluorescence emission spectra of different concentrations of ferric ion in 24.4µM CP, excitation wavelength: 350nm

From *Figure 3.17.*, it is seen that CP shows an emission intensity of 1.94 x 10^6 counts at 438 nm. The ferric ion binding to CP resulted in the decrease in the counts as shown in *Figure 3.18.* The results in *Figure 3.18.* demonstrate that the bound species is not fluorescent in the wavelength region of CP. The rapid decrease in CP fluorescence in *Figure 3.18.*, suggests that there is fluorescence quenching of CP.

Fluorescence quenching of CP can be caused by:

a. Excited state interaction, or

b. Ground state interaction.

In order to establish if fluorescence quenching or binding reaction of CP is proceeding in the ground state, absorption spectrum of the solutions (only 5 µM CP and a combination of 16.95 µM CP and 50 µM $FeCl_3$) were taken. The absorption spectra is shown in Figure 3.19.

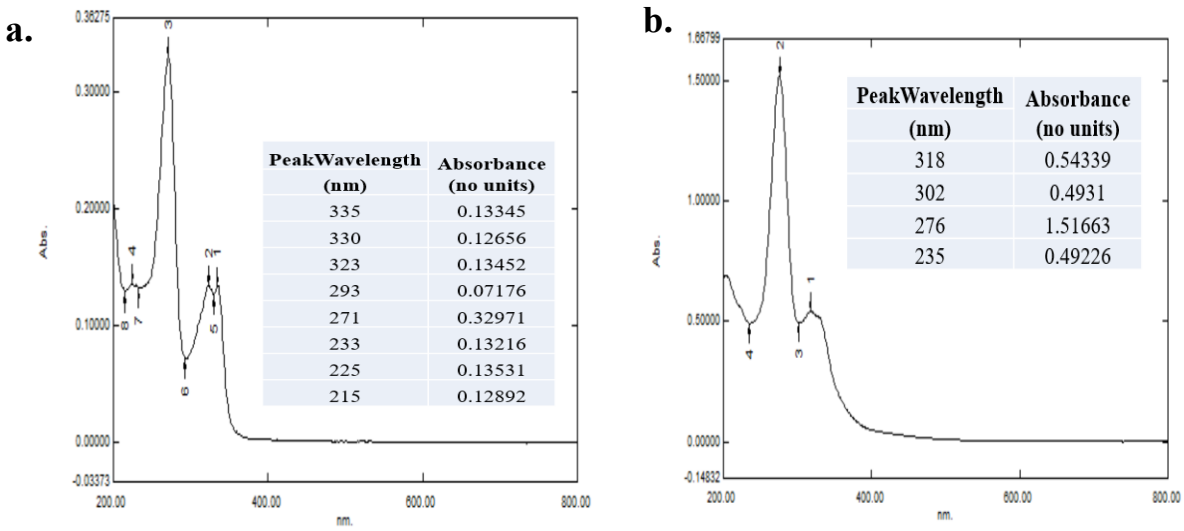

Figure 3.19. UV-Visible absorption spectra of a. 5µM CP, b. 16.95 µM CP and 50 µM $FeCl_3$.

From Figure 3.19, it is seen that peaks obtained at the wavelength of 271nm and 293nm in the absorption spectrum of 5 µM CP have shifted to 276nm and 302nm respectively in the absorption spectrum of 16.95 µM CP and 50 µM $FeCl_3$. In addition to this, the well-separated peaks obtained at wavelength of 335nm and 323nm in the absorption spectrum of 5 µM CP have merged to a single peak obtained at 318nm in the absorption spectrum of 16.95 µM CP and 50 µM $FeCl_3$. This result concluded the absence of excited state interaction of CP and ferric ion. It provided support for ground state interaction for CP and ferric ion. This result explained the development of magenta color in the solution due to the bound CP. The unbound CP contributed to the fluorescence of the solution in the mixture whose concentration decreases with increasing concentration of ferric ion in the medium.

3.3.2 Fluorescence of GQD and ferric ion

Fluorescence experiments also provided additional support to indicate the binding of Fe^{3+} to GQD. GQD was used as the reference sample while studying the fluorescence emission of GQD and ferric ion. The fluorescence emission spectra of reference GQD sample and different concentrations of ferric ion in a constant GQD concentration are shown in the *Figure 3.20.* and *3.21.* respectively.

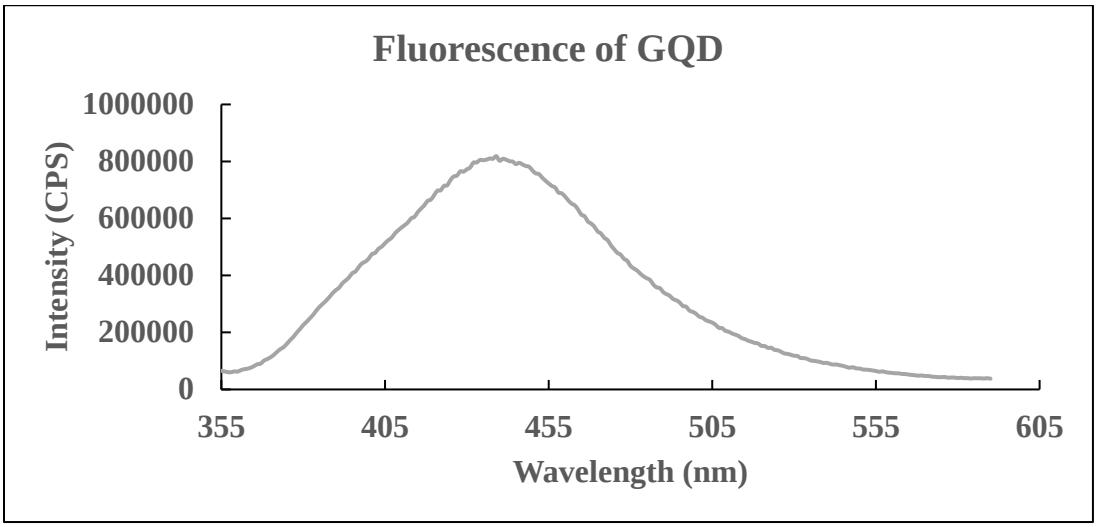

Figure 3.20 Fluorescence emission spectrum of GQD (reference), excitation wavelength: 350nm

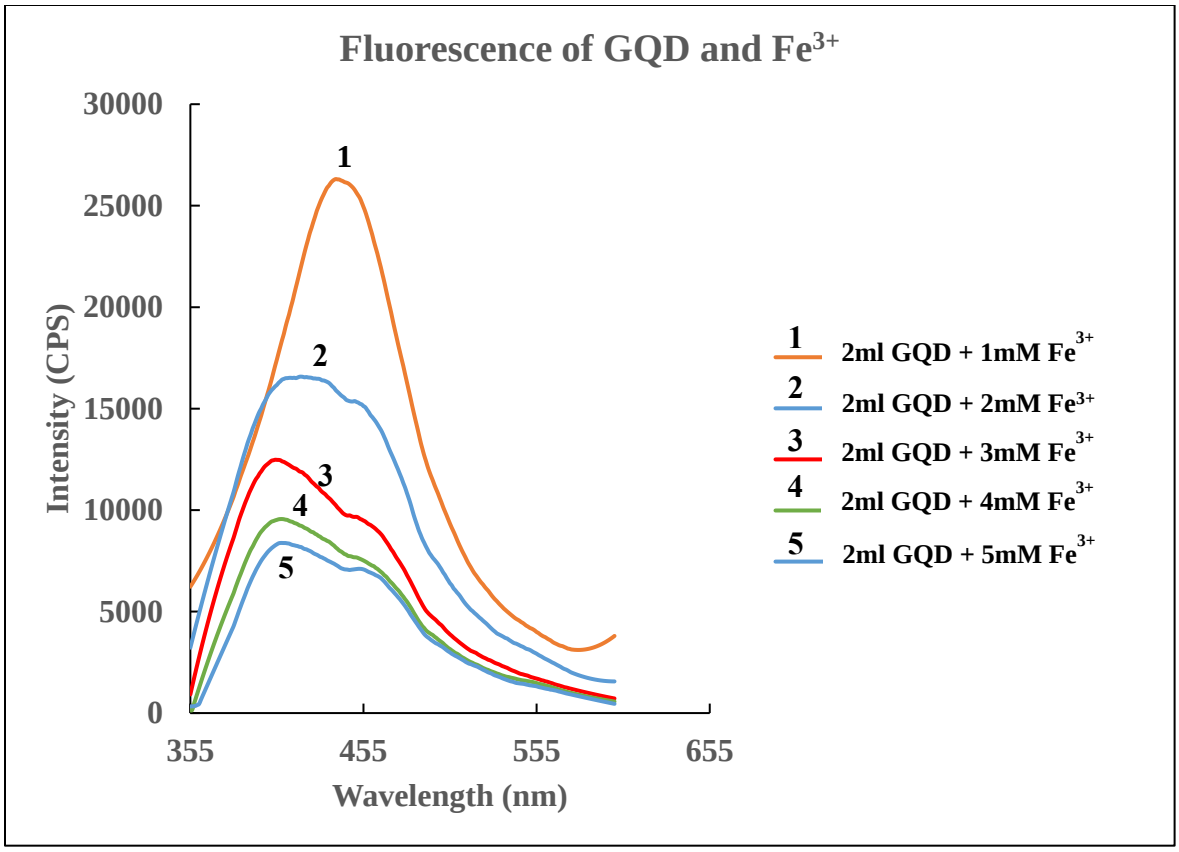

Figure 3.21 Fluorescence emission spectra of different concentrations of ferric ion in a constant concentration, excitation wavelength: 350nm

As seen from *Figure 3.20.*, GQD shows an emission intensity of 8.09 x 10^5 counts per second at 441 nm. The ferric ion binding to GQD resulted in the decrease in the counts as shown in *Figure 3.21.* The emission intensity continuously decreased with successive additions of Fe^{3+} to the GQD reference sample. The decrease in fluorescence intensity of GQD in the composite solution of GQD and ferric ion is attributed to the binding of ferric ion to GQD.

These observations along with FTIR (see section 3.4) confirmed the binding of Fe^{3+} to GQD and hence acts as the support to the utility of the Fe^{3+}- GQD sensor approach for determining CP concentration (as discussed in section 3.2.3.2, 3.2.4 and 3.5).

3.4 FTIR Spectroscopy in support of binding

FTIR spectroscopy was done on solids with ferric chloride alone and a mixture of ferric chloride with added CP solution. This was carried out to have additional support to the binding mechanism of anionic CP to positively charged ferric ion Fe^{3+}. *Table 3.4* gives the FTIR features of the ferric ion and the bound ferric ion with CP.

Table 3.4 FTIR Spectroscopy of ferric ion and the bound species

Compound	**FTIR Peak wavelength (cm^{-1})**
$Fe^{3+}(Cl^{-})_3$	329,399,433,530,596,669,690,842,1180,1340,1363, 1695
$[Fe^{3+}(CP^{-})_3]$	300,351,1153,1261,1271,1288, 1319.1338.1361.1375.1419.1489.1506,1521,1541,1558,1610,1734
CP	1494,1627,1707

The characteristic peaks of ferric ion at 530 cm-^{1}, 596 $cm^{-1}$and 669 cm^{-1} were broadened with the bound species. The peaks at 1489 cm^{-1}, 1610 cm^{-1} and 1734 cm^{-1} are arising from ciprofloxacin due to C-O-C stretch and carbonyl (-C=O) group are shifted from the original values of 1494 cm^{-1}, 1627 cm^{-1} and 1707 cm^{-1} [66]. The shift in the molecular bonds from their original values suggests the binding of anionic CP to positively charged ferric ion Fe^{3+}.

3.5 Resistance measurements for determining CP concentration

The active material of the sensor is made of GQD and ferric chloride. The deposition is done by dropwise addition of two drops of GQD first on the inter digitized space and later by the addition of 50µL drops of 0.1M ferric chloride. The concentration of CP by resistance measurements is determined based on the sensitivity relationship given in equation (3.4).

$$\text{Sensitivity} = \frac{Rf - Ri}{Ri} = \frac{\Delta R}{R} \quad (3.4)$$

where, R_i = R= Resistance of the sensor before exposure to CP or to Argon or Oxygen.

R_f = Resistance of the sensor after exposure to CP or to Argon or Oxygen.

ΔR = Change in resistance of the sensor.

3.5.1 Modeling the sensor methodology using resistance measurements

3.5.1.1 Before treatment with CP solutions

A pictorial representation of the active material of the sensor consisting of GQD and ferric ion is shown in *Figure 3.22.*

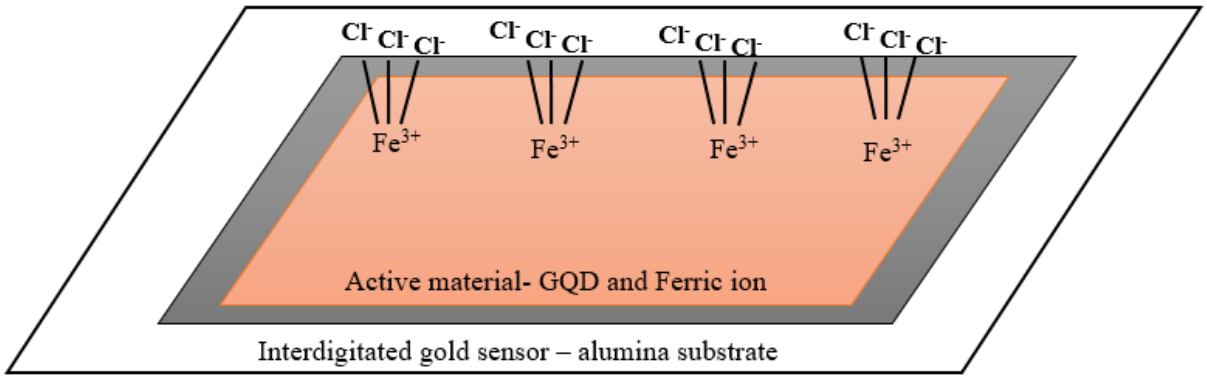

Figure 3.22.Pictorial representation of the active material of the sensor.

As ferric chloride is used to coat ferric ion on the sensor surface, three chloride ions are bonded to the ferric ion coated over the GQD surface which is in turn coated over the alumina substrate surface of the interdigitated gold electrode sensor. The total number of active Fe^{3+} sites available to bind to CP is theoretically calculated from the moles of ferric ion ($50x10^{-7}$ moles) used for coating the sensor and the Avogadro's number ($6.02x10^{23}$ atoms/mole) as $3.01x10^{18}$.

3.5.1.2 After treatment with CP solutions

When treated with CP solution (for example, 2ml of 0.5µM CP), some of the active sites of Fe^{3+} ions get used up due to the binding of Fe^{3+} to CP^- ions as discussed in section 3.2.2. Each Fe^{3+} binds to three CP^- ions (section 3.2.2.1) and this binding (assuming 100% binding) is pictorially represented in *Figure 3.23* below.

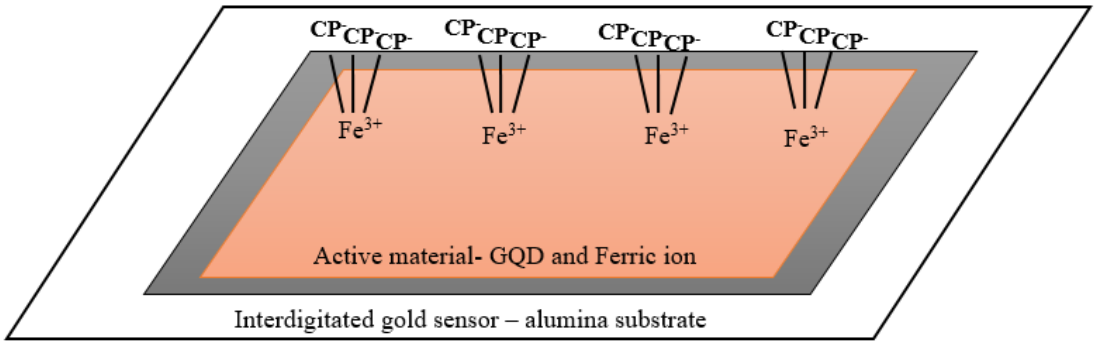

Figure 3.23.Pictorial representation of the binding of Fe^{3+} ions to three CP^- ions.

This estimation of CP binding to Fe^{3+} sites leaves $2x10^{14}$ sites on the sensor for subsequent usage. With increasing CP concentrations, the number of available Fe^{3+} sites for binding with CP decreases continuously because at each addition, some available Fe^{3+} sites get used up while CP and Fe^{3+} bind to each other. At an n^{th} addition of CP concentration, the number of available Fe^{3+} sites would be $(N-x_1-x_2-x_3-x_4-\ldots..x_n)$, where N is the total number of sensor active sites before treatment with CP, $x_1,x_2,x_3,\ldots,x_n$ are the Fe^{3+} sites used up for binding Fe^{3+} and CP during each CP addition. The continuous decrease in the number of available Fe^{3+} sites with increasing CP concentration is shown in *Figure 3.24*.

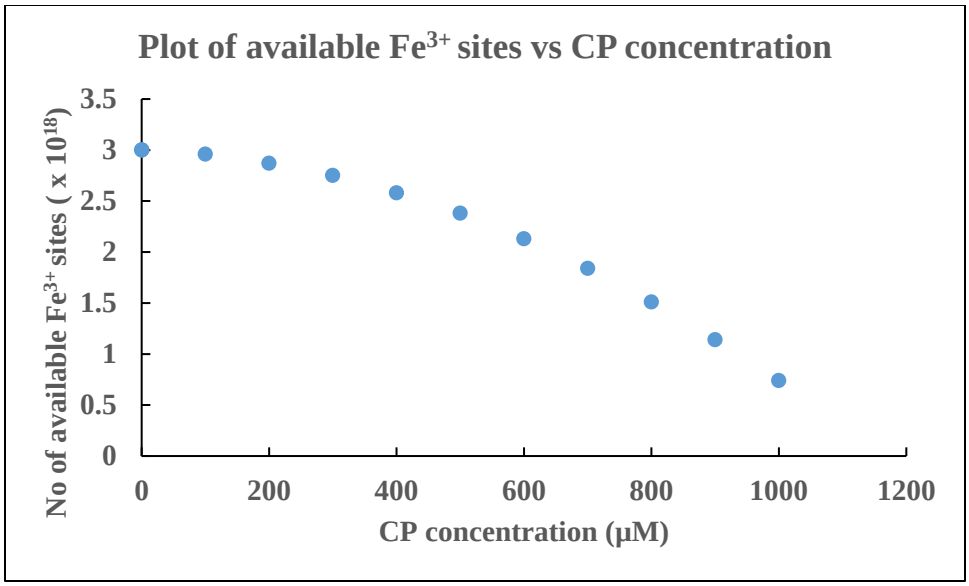

Figure 3.24. Continuous decrease in the number of available Fe^{3+} sites with increasing CP concentration

The continuous decrease in the number of available Fe^{3+} sites with each CP addition as seen in *Figure 3.24*, is related to the measured resistance by the relation given in (3.5),

$$R = k * x * \frac{1}{N} \tag{3.5}$$

where, R is the resistance of the sensor (Ω), x is the binding probability (no unit), N is the number of available sites (no unit) and k is the correlation coefficient between R and N (Ω). For a system with constant k and x, the decrease in N is associated with an increase in R.

Considering the above factors mentioned, three different plots are proposed to be used for determining the CP concentration using the measured value of resistance.

1. Concentration plots with reference to original N sites corrected for extraneous removal of active sites;
2. Conventional ΔR/R plots ignoring the decreasing available sites concept; and

3. Sensor plots based with reference to decreasing available sites.

An illustration of the proposed concentration plots are shown in *Figures 3.25* and *3.26*.

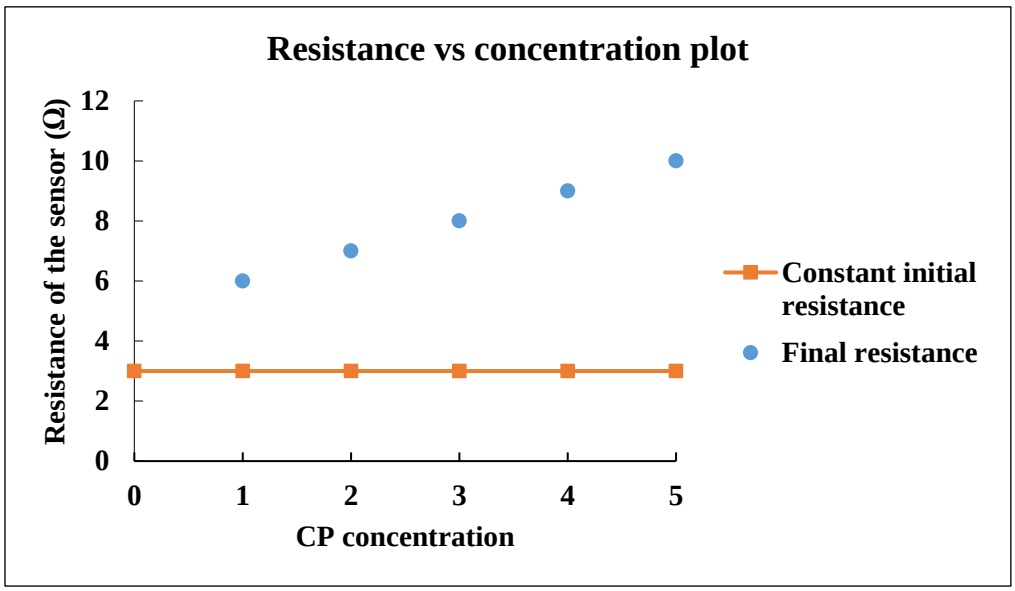

Figure 3.25. Concentration plots ignoring the decreasing available sites concept (plot type 1 and 2)

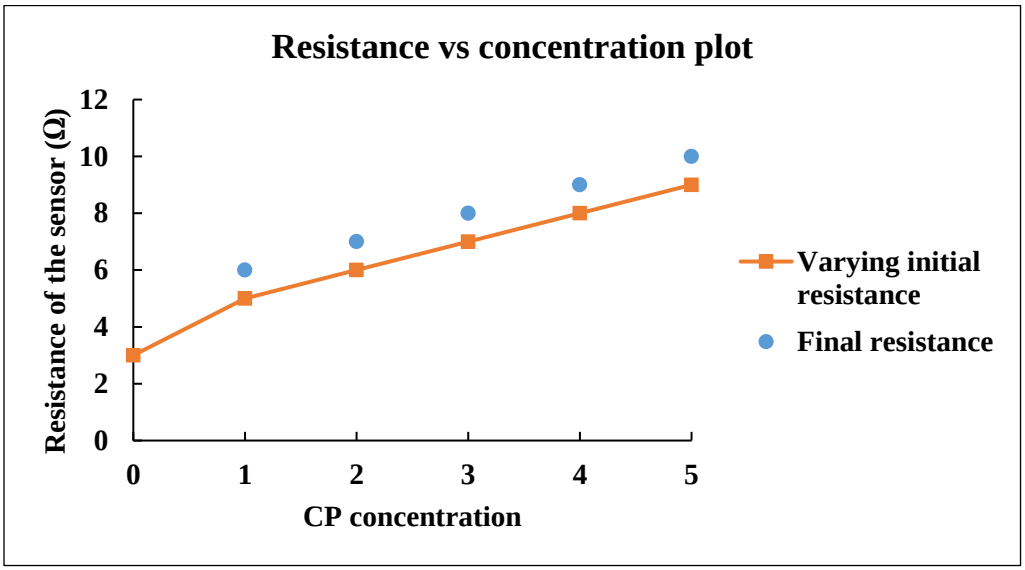

Figure 3.26. Concentration plots with reference to decreasing available sites concept (plot type 3)

For the types of plots 1 and 2, the original resistance of the sensor in air (that is the resistance measured for the active material before treating with CP) remains the same. The resistance change with each concentration is calculated by keeping R_i constant. For the 3rd type of plot, the resistance of the sensor, R_i keeps changing as the available sites decreases continuously. However, this type of plot would be difficult to determine the concentration of CP because the change in resistance ΔR will not be accurate because of the varying initial resistance.

The results of measurements performed using the inter-digitated gold electrode sensor with GQD-ferric ion active material is discussed in the following sections. All the resistance and concentration plots for calibration have been plotted by ignoring the decreasing available sites concept.

3.5.2 Resistance (R_i) measurements of the sensor blank

The resistance measurements were made using the interdigitated Gold electrode with GQD bound ferric ion. Three resistance measurements were made by repetitively switching the interdigitated GQD-ferric ion sensor between the resting chamber for 30 minutes and testing chamber. These three resistance measurements are made in the testing chamber as the sensor blank with a finite number of active sites, R_i.

Table 3.5 gives the results of these three measurements.

Table 3.5 Resistance measurements of the sensor blank, R_i.

Trial Number	Response in air R_i (kΩ)
Trial 1	3.068
Trial 3	3.59
Trial 3	3.33
Average	**3.33**

The sensor blank also showed the property of giving 267.4 mV output when measured in the configuration

$$Au/Al_2O_3: GQD\text{-}Fe^{3+}/Au \quad (3.6)$$

in the testing chamber.

3.5.3 Resistance (R_f) measurements in different CP solutions

Resistance of the sensor in different solutions of 5 different CP concentrations was measured by injecting the solution into the sensor testing chamber and allowing the resistance to reach a stable value. After each measurement, the sensor was washed well with distilled water and kept in a hot bath for 15 minutes to desorb any species adsorbed on the sensor surface. The response of the sensor to different CP solutions is shown in *Table 3.6*.

Table 3.6 Response of the sensor to varying CP concentrations

CP Concentration (µM)	**$\Delta R/ R_i$ (no units)**
0.5	**1.58**
1	**1.73**
1.5	**1.96**
2	**1.96**
2.5	**2.14**

As seen from *Table 3.6*, the resistance of the sensor increases with increasing CP concentration. This validates the equation 3.4 where the resistance increases with decreasing number of available Fe^{3+} sites and provides support to the binding reaction discussed in section 3.2.2.1 implying that $[Fe^{3+} - (CP^{-})_3]$ provides higher resistance to voltage. Based on the change in the value of ΔR/R with respect to different CP concentrations, CP concentration can be determined based on the resistance measurements.

3.5.4 CP sensor models

3.5.4.1 Model 1 – Disposable sensor

Based on the binding reaction of anionic CP species to positive ferric ion (as discussed in 3.2.2.1) and the data given in *Table 3.6*, a sensor methodology to determine CP concentrations by resistance measurements is developed as given below in *Figure 3.27.*

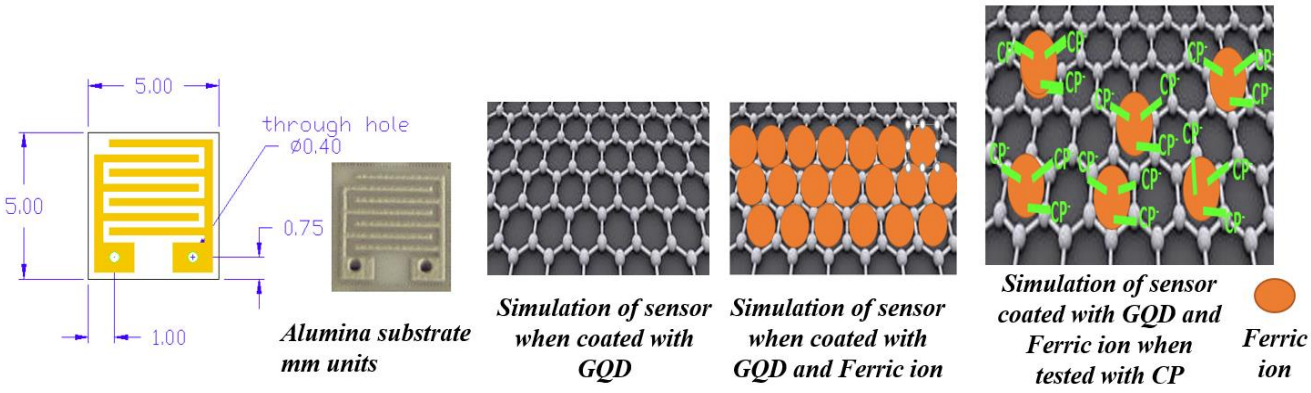

Figure 3.27. CP Sensor approach using interdigitated Gold electrode with GQD bound ferric ion

As seen from *Figure 3.27.*, the binding of anionic CP to ferric ion occurs on the sensor surface. This binding reaction changes the resistance of the sensor. The calibration curve for

determining CP concentration using the interdigitated Gold electrode with GQD bound ferric ion sensor is plotted by using the values of ΔR/R vs CP concentrations from *Table 3.6.*

The calibration curve of the CP sensor is shown in *Figure 3.28.* below.

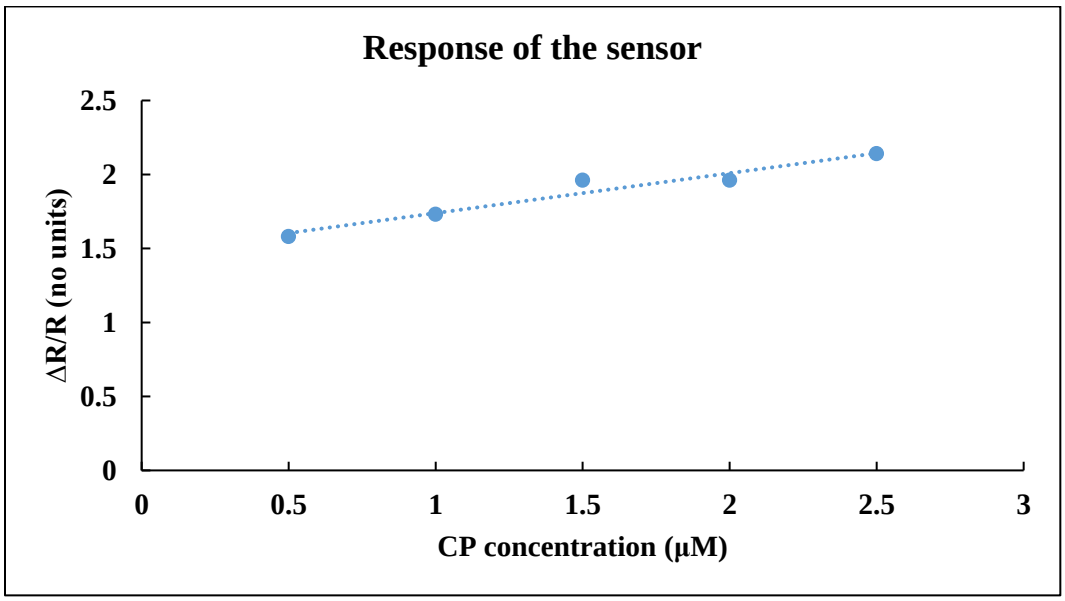

Figure 3.28. Calibration curve for CP sensor by resistance measurements using interdigitated Gold electrode with GQD bound ferric ion

The calibration curve has been plotted by ignoring the decreasing available sites concept. But in reality, available sites get used up with every addition of CP. Hence, it is advisable to use the sensor only once for accurate resistance measurement. Using the calibration curve (*Figure 3.28*), if any sample solution of unknown CP concentration is given, its value can be determined by measuring the value of ΔR/R using the GQD bound ferric ion sensor. For accurate measurement and to avoid the decrease in available Fe^{3+} sites, it is recommended that after one time measurement, the sensor should be thrown away and a new sensor should be used.

3.5.4.2 Model 2 – Regenerative sensor

A regenerative sensor model is proposed to enable reusability of the sensor. The sensor can be made reusable if the number of available Fe^{3+} is regenerated to the original value that was obtained before the treatment of CP. One possible way to regenerate the originally available Fe^{3+} sites is to immerse the sensor in 1N HCl solution and pass a current through the sensor for a duration of 30 s to 1 minute after treatment with CP. This would reduce Fe^{3+} to Fe^{2+}. Since CP does not bind to Fe^{2+}, the bound CP anions will be released back into the HCl solution. Fe^{3+} can be regenerated by performing CV in a range from the reduction potential of Fe^{2+} to the oxidation potential of Fe^{3+}. This would help in regenerating all the originally available Fe^{3+} sites and keep the initial resistance of the sensor constant. This approach has a potential scope for future research and investigation.

3.5.5 Effect of interferences

The effect of urea in the measurement of CP was studied by measuring the resistance of the sensor in a combination of CP and urea solutions. 5mM and 0.5M Urea solutions were added to different CP solutions of concentrations (0.5µM, 1µM, 1.5µM, 2µM and 2.5µM). The resistance of the sensor in each measurement was recorded. The response of the sensor to different CP solutions containing 5mM Urea is shown in *Table 3.7*.

Table 3.7 Response of the sensor to various CP solutions containing 5mM Urea

CP Concentration (µM)	**∆R/ Ri (no units)**
0.5	**1.32**
1	**1.61**
1.5	**1.79**
2	**1.89**
2.5	**2.16**

The response of the sensor to different CP solutions containing 0.5M Urea is shown in *Table 3.8*.

Table 3.8 Response of the sensor to various CP solutions containing 0.5M Urea

CP Concentration (µM)	ΔR/ Ri (no units)
0.5	**1.90**
1	**1.96**
1.5	**2.15**
2	**2.14**
2.5	**2.14**

As seen from *Table 3.7 and Table 3.8*, the resistance of the sensor increases with increasing CP concentration. This is in compliance with the resistance measurements performed without urea. It also validates the equation 3.5 where resistance increases with decreasing number of available Fe^{3+} sites. These indicate that there is no interference of urea in the concentration measurement of CP using the sensor.

To obtain statistically accurate measurements, each resistance measurement in the study was repeated for 3 trials. The standard deviation of the data obtained was between 0.0635 and 0.219. Values of variance of the data obtained were between 0.004 and 0.048. Data averaging was done to increase the accuracy of the resistance measurements. Three repetitive trials for each measurement were performed and the average of values obtained were used in the tabulation and concentration plots. The concentration plots shown in *Figure 3.29* are also plotted by ignoring the decreasing available sites concept.

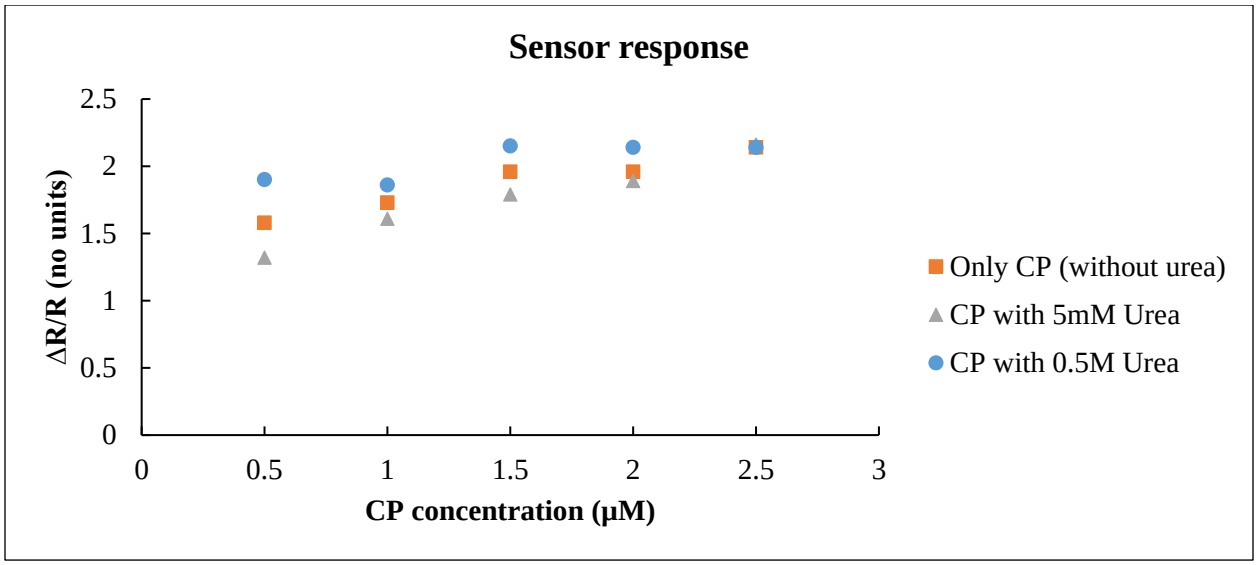

Figure 3.29. Response of the sensor to various CP solutions containing 5mM and 0.5M Urea

The effect of urea in the CP concentration measurement is seen clearly from *Figure 3.29* which indicates that there is no interference of urea in the concentration measurement of CP using the sensor.

3.5.6 Effect of oxygen

When the sensor blank was kept in the testing chamber, oxygen (air) was flown into the chamber to record the sensor response. The sensor responded by undergoing continuous increase in its original value of 236.4 kΩ to MΩ to infinite resistance. It is attributed to adsorption of the gas by the sensor. When the gas is desorbed, the sensor regained its original resistance value.

3.5.7 Effect of Argon

When the sensor blank was kept in the testing chamber, argon gas was flown into the chamber to record its response. The sensor responded by changing its original value from 236.4 kΩ to infinite resistance. The sensor regained its original resistance value when the adsorbed gas was desorbed.

CHAPTER – 4

CONCLUSION

In this study, a CP sensor was developed by using ferric ion as the probe and utilizing the unique properties of GQD. Two sensor methodologies for determining CP concentration have been formulated and presented. They are:

1. Electrochemical sensor (formulated by an electrochemical technique called Differential Pulse Voltammetry (DPV) and chronoamperometry); and
2. Resistive sensor (formulated by resistance measurement technique).

The electrochemical performance of the two different electrodes (bare GCE and GCE modified by GQD) were studied and compared by employing ferric ion as a probe to sense CP in the pH value of 6.4. The determination of detection limit (for bare GCE and for GCE modified by GQD) and sensitivity (for bare GCE and for GCE modified by GQD) of this technique are also presented.

While using unmodified GCE as the working electrode to determine CP concentration, the DPV calibration curve plotted by measuring the net peak current of ferric ion at 0.34V is used to measure the concentration of CP. The sensitivity of this technique was about 55nA/µM. While using GCE modified by GQD as the working electrode to determine CP concentration, the DPV and chronoamperometric calibration curves are used to measure the concentration of CP. By measuring the value of the reduction peak current of $[Fe^{3+} - (CP^{-})_3]$ at 0.20 V and by comparing the measured value with the DPV calibration curve, the value of CP concentration can be determined. The sensitivity of this technique was about 243 nA/µM. By measuring the value of

the total integrated coulombic charge of [Fe^{3+} - $(CP^{-})_3$] and by comparing the measured value with the chronoamperometry calibration curve, the value of CP concentration has been determined.

The determination of CP concentration by resistance measurements and by using the calibration curve which was plotted based on the sensitivity relation ($\Delta R/R$), was given in detail. Supporting data for the binding mechanism to form [Fe^{3+} - $(CP^{-})_3$] is included from fluorescence and FTIR data.

Some challenges faced in CP concentration determination while using electrolyte of different pH ranges and carbon nanotubes (CNT) pipette electrodes as working electrodes are also discussed. Some preliminary work done for determining the concentration of p-aminophenol (PAP) is also presented as a scope for future work.

CHAPTER – 5

FUTURE WORK

The current research work has provided some exciting results, which have scope and potential for carrying out future work. The research work can be extended in future to study the following.

1. Use the currently developed sensor methodology as a prelude for probing into intracellular electrochemistry with CNT pipette electrodes coated with GQDs.
2. Analyze the effect of possible interferences for CP when biological samples are used. The possible interferences include ascorbic acid, albumen, caffeine and dopamine.
3. Electrochemically investigate the PAP behavior with GCE and CNT pipette electrodes modified by GQD to develop a sensor methodology for PAP.

Some of the preliminary results obtained with CNT pipette electrodes modified by GQD for studying CP and with GCE modified by GQD for investigating PAP are given below.

5.1 Preliminary results obtained for future work

5.1.1 Investigation using CNTs modified by GQD

Electrochemical studies were carried out using CNT pipette electrodes supplied by the Nano Bio-Interface laboratory. The behavior of unmodified CNT pipette electrodes and CNT modified by GQD was investigated. The DPV experiments for unmodified CNT pipette electrodes were performed using an electrolyte of 10ml - 0.1M Na_2SO_4 (pH=6.4) containing 5mM ferric ion. DPV was performed by scanning the system from an initial voltage of 0.6 V to a final voltage of -

0.5 V by applying fixed magnitude pulses, each of 20mV pulse size, 0.1s pulse time and 1s sample time. The DPV curve of unmodified CNT pipette electrode is shown in *Figure 5.1.*.

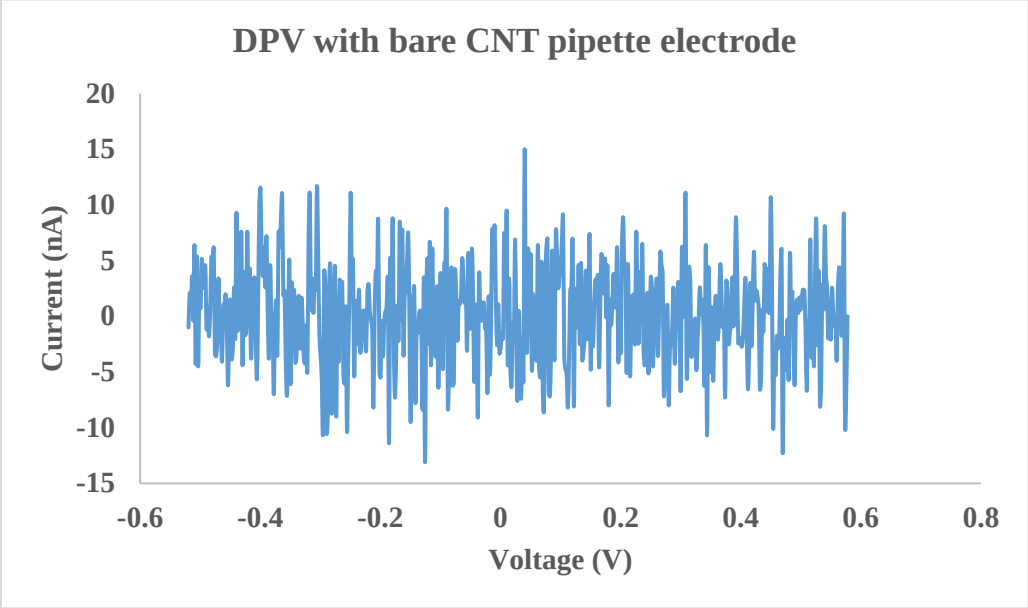

Figure 5.1. DPV for 5mM ferric ion using unmodified CNT pipette electrode

Figure 5.1 shows that the unmodified CNT pipette electrodes were very poor in performance and could not give any valuable results. The unmodified CNT pipette electrodes were then modified with GQD to carry out further electrochemical studies with DPV. DPV using CNT pipette electrodes modified with GQD were carried out for an electrolyte of 10ml – 0.1M KCl and 5mM potassium ferrocyanide. DPV was performed by scanning the system from an initial voltage of 0.5 V to a final voltage of 0 V by applying fixed magnitude pulses, each of 20mV pulse size, 0.1s pulse time and 1s sample time. The DPV curve of unmodified CNT pipette electrode modified by GQD is shown in *Figure 5.2.*.

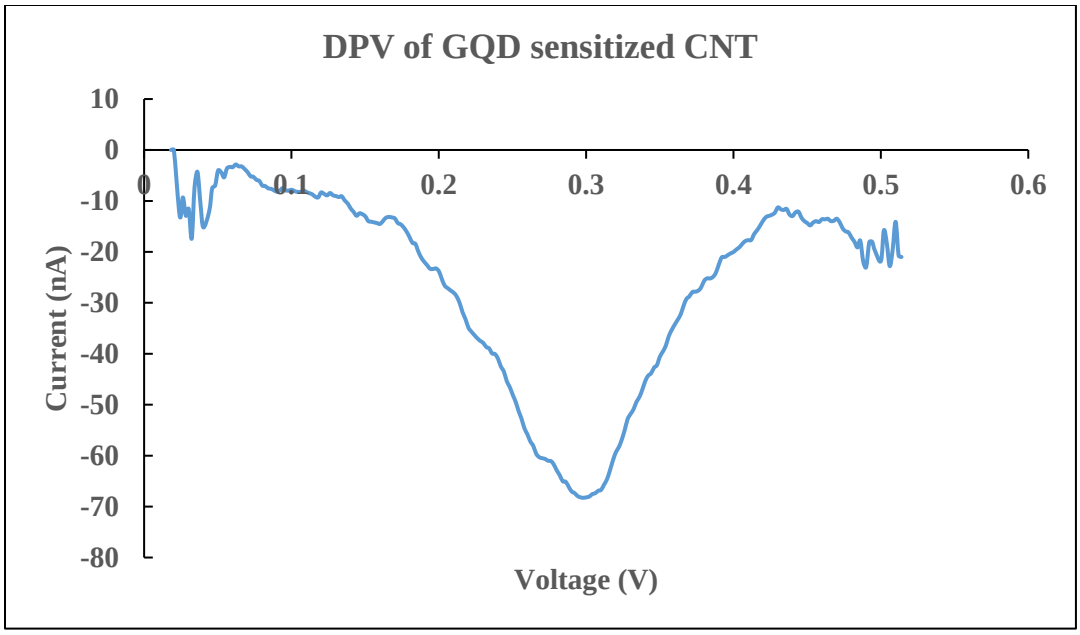

Figure 5.2. DPV for 5mM ferric ion using CNT pipette electrode modified by GQD

As seen from *Figure 5.2.*, there is a DPV peak observed at E_p = 0.31 V corresponding to ferric ion with a peak current of 66.28 nA. The sensitivity and performance of CNT pipette electrodes modified with GQD is clearly better than unmodified CNT pipette electrodes. Though the handling and use of these tiny pipette electrodes may be challenging, there is apparent scope and potential for future work using the GQD modified CNT pipette electrodes for probing into intra-cellular electrochemistry.

5.1.2 Investigation of p-Aminophenol (PAP)

To electrochemically investigate the behavior of PAP, electrochemical experiments like CV and DPV were performed using an electrolyte of 10ml - 0.1M Na_2SO_4 (pH=6.4) containing different concentrations of PAP. Both the unmodified GCE and GCE modified by GQD electrodes were used to study the behavior of PAP. DPV was performed by scanning the system from an initial voltage of -0.3 V to a final voltage of 0.55 V by applying fixed magnitude pulses, each of

25mV pulse size, 2mV step size, 3s pulse time and 5s sample time. CV was performed by using unmodified GCE by scanning the system from an initial voltage of 0.8 V to a final voltage of -0.5 V with a scan rate of 20mV/s. The effect of varying different parameters of DPV like step size and pulse size while using unmodified GCE was also determined. The results of different electrochemical experiments are described below.

5.1.2.1 Investigation with unmodified GCE

The cyclic voltammogram obtained for 1µM PAP in an electrolyte of 10ml-0.1M Na_2SO_4 is shown in *Figure 5.3.*.

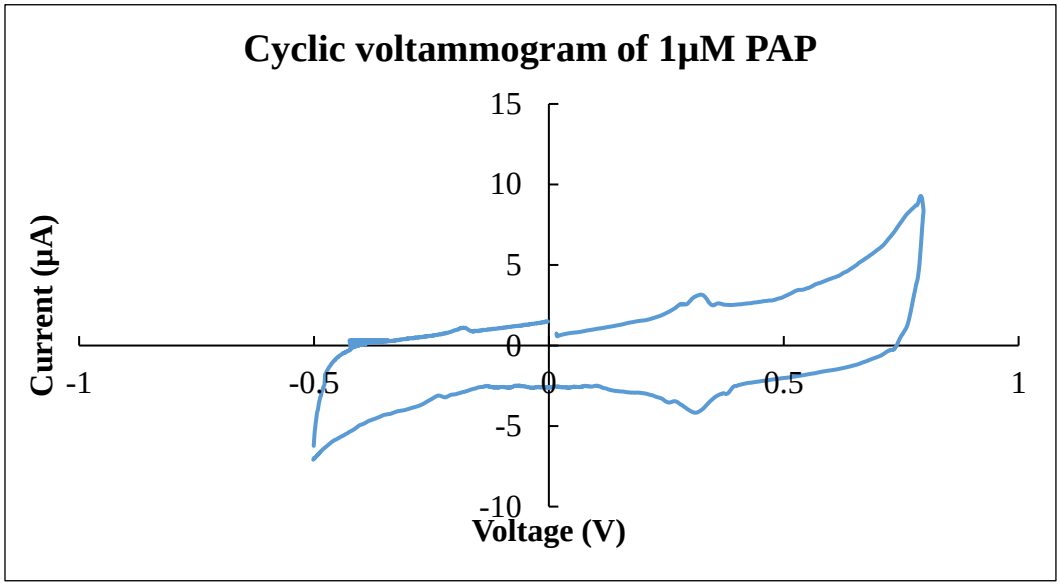

Figure 5.3. Cyclic voltammogram of 1µM PAP

From *Figure 5.3.*, it is seen that the PAP system has an oxidation peak at E_{pa} =0.322 V with a peak current of 3.16 µA and a reduction peak at a potential of E_{pc} = 0.319 V with a peak current of 4.11µA. The peak separation ΔE_p = 3 mV, indicating the system is a reversible system. The system was further observed by DPV. The DPV curve of 1µM PAP is was studied by varying the DPV parameters like step size and pulse size.

5.1.2.1.1 Effect of pulse size variation

DPV was performed by scanning the system from an initial voltage of -0.3 V to a final voltage of 0.55 V by applying fixed magnitude pulses, each of 25mV pulse size, 3s pulse time and 5s sample time and varying step sizes. Three step sizes 2 mV, 4 mV and 6 mV were investigated. The DPV curve for 1µM PAP with varying step sizes is shown in *Figure 5.4.*.

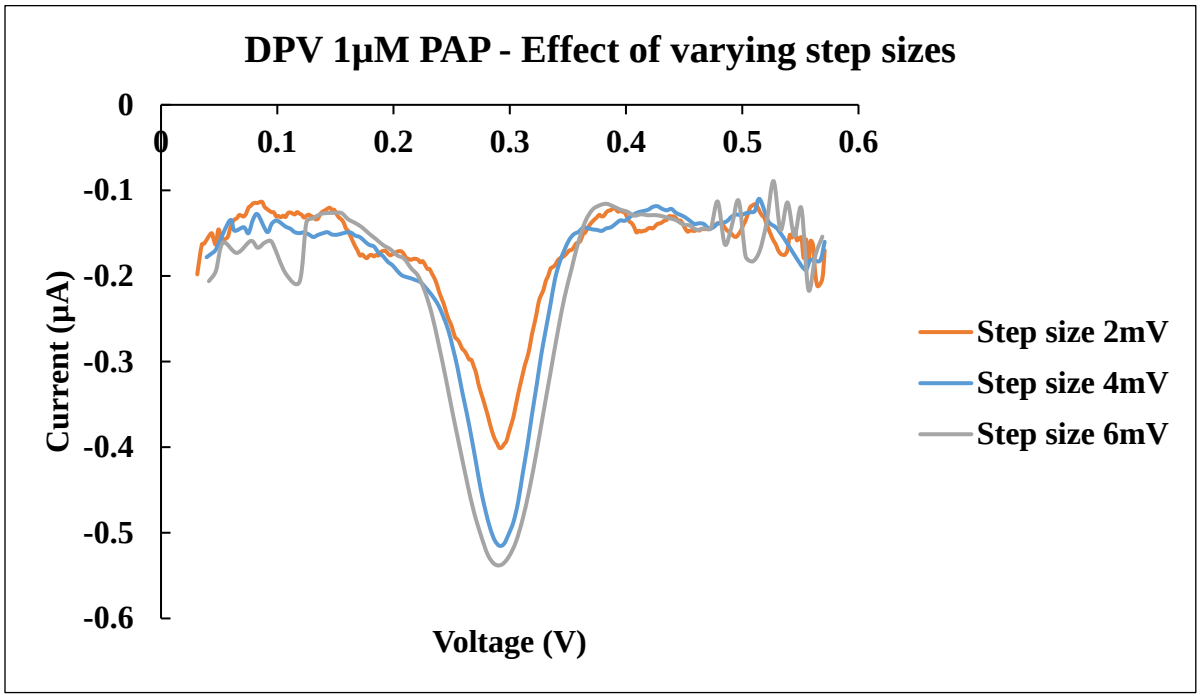

Figure 5.4. DPV of 1µM PAP for varying step sizes.

As seen from *Figure 5.4.*, the peak for 1 µM PAP at E_p=0.3 V became narrower with decreasing step size. The most well defined, narrow peak was obtained for 2 mV step size. Hence, the optimum parameter for step size was identified to be 2 mV.

5.1.2.1.2 Effect of step size variation

DPV was performed by scanning the system from an initial voltage of -0.3 V to a final voltage of 0.55 V by applying fixed magnitude pulses, each of 3s pulse time, 2mV step size and 5s sample

time and varying pulse sizes. The effect of varying pulse sizes was studied with respect to the optimized step size 2 mV. The effect of different pulse sizes on the DPV of 1 µM PAP is given in *Figure 5.5.*

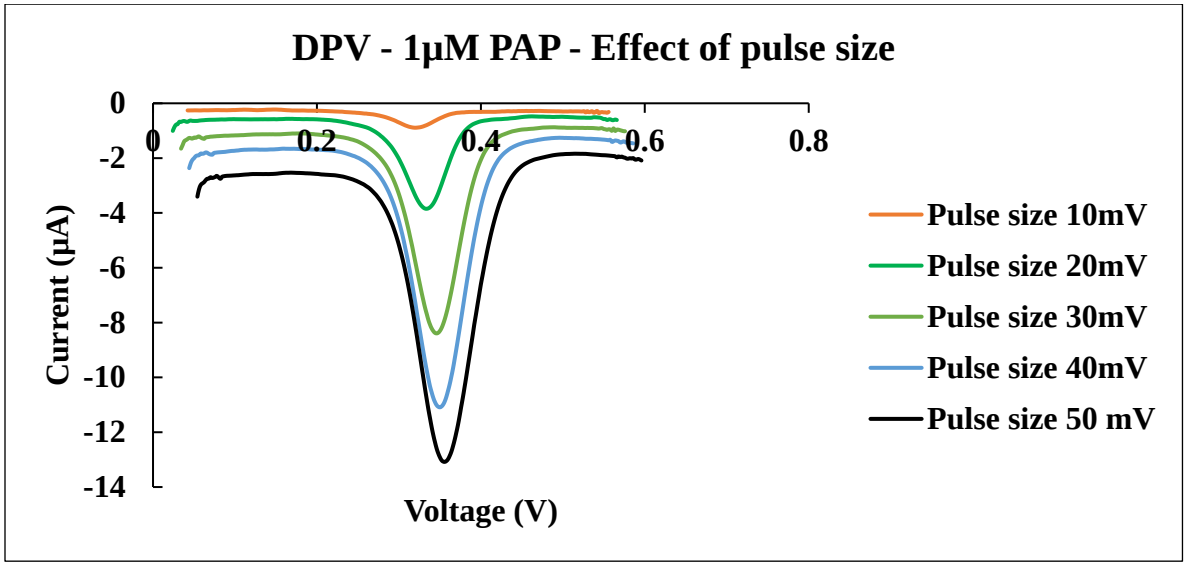

Figure 5.5. DPV of 1µM PAP for varying pulse sizes.

As seen from *Figure 5.5.*, the peak current at E_p = 0.3V for 1 µM PAP continuously increased with increasing pulse size. The values of peak current for various pulse sizes and 2mV step size is shown in *Table 5.1.*

Table 5.1. Values of 1 µM PAP DPV peak current for different pulse sizes

Pulse size (mV)	Faradaic current (uA)
10	0.597
20	3.117
30	7.505
40	9.907
50	11.15

From *Figure 5.5.*, the most well-defined, sharp, narrow peak with the largest peak current of was obtained for 2 mV step size. Hence, the optimum parameters for step size was identified to be 2 mV and pulse size of 50mV for studying the DPV of 1µM PAP using unmodified GCE.

5.1.2.2 Investigation with GCE modified by GQD

DPV was performed by scanning the PAP system from an initial voltage of -0.3 V to a final voltage of 0.55 V by applying fixed magnitude pulses, each of 25mV pulse size, 3s pulse time and 5s sample time and 2 mV step size. The DPV obtained for different concentrations of PAP using GCE modified by GQD is shown in *Figure 5.6.*

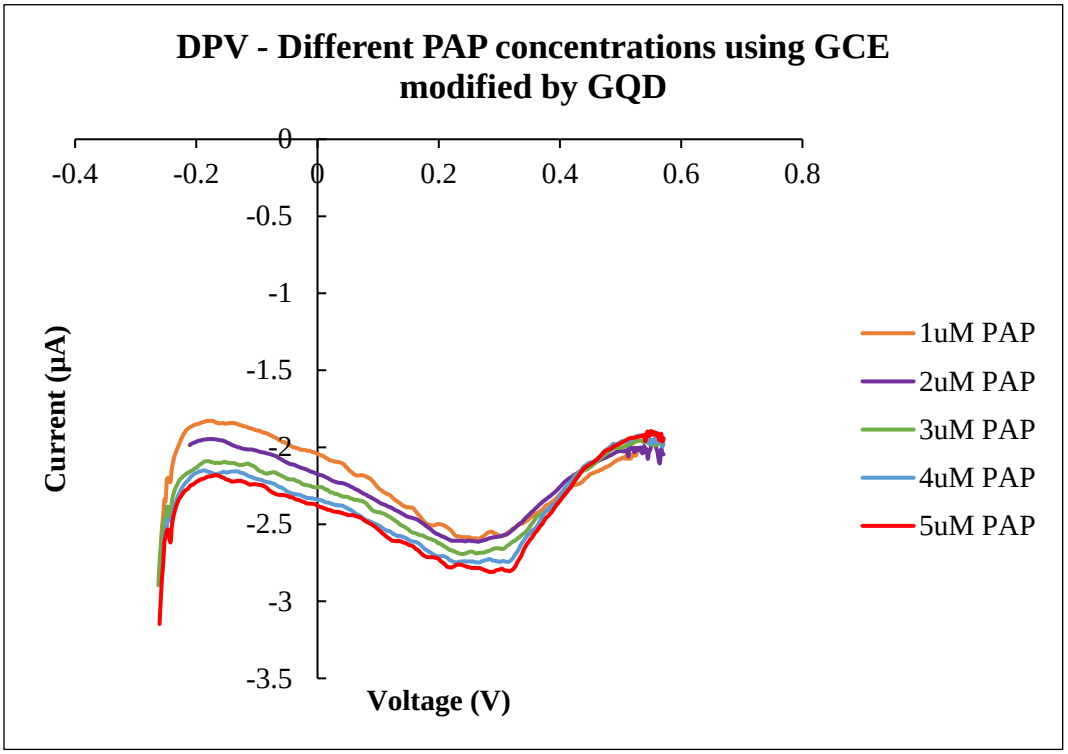

Figure 5.6. DPV for different PAP concentrations obtained by GCE modified by GQD.

From *Figure 5.6.*, no well-defined peak is obtained by GCE modified with GQD with the currently defined DPV parameters. The variation of DPV parameters and carrying out further

electrochemical investigation using unmodified GCE and GCE modified by GQD to clearly define the behavior of PAP to develop a sensor mechanism for PAP is a part of future work of this research.

The current research work and the above mentioned possible future work have a promising application of developing sensitive, portable and least expensive methods for sensing and estimating the concentration of antibiotics in the near future.

REFERENCES

1. I. Mechnikov and P. Ehrlich, The Nobel Prize in Physiology or Medicine **(1908)**, *Nobel Lectures, Physiology or Medicine 1901-1921, Elsevier Publishing Company, Amsterdam, 1967*. Available online: https://www.nobelprize.org/nobel_prizes/medicine/laureates/1908/ehrlich-lecture.pdf
2. S.Waksman, My Life with the Microbes, (*New York: Simon and Schuster*, (**1954**), p.3.
3. A. Fleming (**1929**). "On the antibacterial action of cultures of a penicillium, with special reference to their use in the isolation of B. influenzæ". *British Journal of Experimental Pathology*. 10(31): 226–236. PMC 2048009.
4. Z. Protich, P. Wong and K.S.V. Santhanam, *Journal of Power Sources* 332 (**2016**) 337e344.
5. Z. Protich, K.S.V. Santhanam, A. Jaikumar, S. Kandlikar and P. Wong *J. Electrochem. Soc.* 163 (6) (**2016**) E166eE172.
6. A. Jaikumar, K.S.V. Santhanam, S. Kandlikar, I.B.P. Raya and P. Raghupathi, *ECS Trans*. 66 (30) (**2015**) 55e64.
7. A.K. Geim and K.S. Novoselov, The rise of Graphene, *Nature Materials* 6, **(2007),**183-191.
8. Y. Hernandez, V. Nicolosi, M. Lotya, M.F. Blighe, Z. Sun, S. De, I. T. McGovern, B.Holland, M. Byrne, Y.K. Gun'Ko, J.J. Boland, P. Niraj, G. Duesberg, S. Krishnamurthy, R. Goodhue, J.Hutchison, V. Scardaci, A.C. Ferrari & J.N. Coleman, High-yield production of graphene by liquid-phase exfoliation, *Nature Nano.* 3, **(2008),** 563.

9. DA Dikin, S Stankovich, EJ Zimney, RD Piner, GH Dommett, G Evmenenko, ST Nguyen and RS Ruoff, Preparation and characterization of graphene oxide paper, *Nature* 448, **(2007),** 457.

10. C. Oshima and A. Nagashima, Ultra-thin epitaxial films of graphite and hexagonal boron nitride on solid surfaces, *J. Phys. Cond. Matt.* 9, **(1997),** 1.

11. A. H. C. Neto, F. Guinea, N. M. R. Peres, K. S. Novoselov, and A. K. Geim, The electronic properties of graphene, *Rev. Mod. Phys.* 81, 109 – Published 14 January **2009**.

12. Y. Zhang, , Y.W. Tan, H.L. Stormer, and P. Kim, Experimental observation of the quantum Hall effect and Berry's phase in graphene, *Nature* 438, **(2005),** 201.

13. L A Falkovsky, Optical properties of graphene, *Journal of Physics: Conference Series* 129 012004, **(2008)**.

14. E. Pop, V. Varshney and A.K. Roy, Thermal properties of graphene: Fundamentals and applications, *Materials Research Society*, Volume 37, Issue 12 (Graphene Fundamentals and Functionalities, **(2012)** pp. 1273-1281.

15. I.A. Ovid'ko, Mechanical properties of graphene, *Rev. Adv. Materials Science*, volume 34, **(2013)**, pp 1-11.

16. R.C Ashoori, "Electrons in artificial atoms", *Nature*, 379 (6564): 413–419, **(1996)**. Bibcode:1996, Nature.379..413A. doi:10.1038/379413a0.

17. Askari and M. Bagher, Quantum Dots Applications, *Sensors and Transducers*, 198, **(2016)** 37-43.

18. J. Shen, Y. Zhu, X. Yanga and C. Li, Graphene quantum dots: emergent nanolights for bioimaging, sensors, catalysis and photovoltaic devices, *Chem. Commun.*, 48, **(2012)** p. 3686-3699.

19. S. N. Baker and G. A. Baker, Luminescent carbon nanodots: emergent nanolights, Angew. *Chem., Int. Ed.*, 49, **(2010)** 6726–6744.

20. S. T. Yang, L. Cao, P. G. Luo, F. S. Lu, X. Wang, H. F. Wang, M. J. Meziani, Y. F. Liu, G. Qi and Y. P. Sun, *J. Am. Chem. Soc.*,131, **(2009)** 11308–11309.

21. S. Kellici, J. Acord, N.P. Power, D.J. Morgan, P. Coppo, T. Heilf and B. Saha, Rapid synthesis of graphene quantum dots using a continuous hydrothermal flow synthesis approach, *RSC Adv.*, 7, **(2017)** 14716.

22. S.H. Kang, S. Mhin, H. Han, K.M. Kim, J.L. Jones, J.H. Ryu, J.S. Kang, S.H. Kim & K.B. Shim, Ultrafast Method for Selective Design of Graphene Quantum Dots with Highly Efficient Blue Emission, *Nature, Scientific Reports*, 6:38423, DOI: 10.1038/srep38423.

23. S. L. Hu, K. Y. Niu, J. Sun, J. Yang, N. Q. Zhao and X. W. Du, One-step synthesis of fluorescent carbon nanoparticles by laser irradiation, *J. Mater. Chem.*, 19, **(2009)** 484–488.

24. J. G. Zhou, C. Booker, R. Y. Li, X. T. Zhou, T. K. Sham, X. L. Sun and Z. F. Ding, An Electrochemical Avenue to Blue Luminescent Nanocrystals from Multiwalled Carbon Nanotubes (MWCNTs), *J. Am. Chem. Soc.*, 129, **(2007)** 744–745.

25. J. G. Zhou, C. Booker, R. Y. Li, X. L. Sun, T. K. Sham and Z. F. Ding, An electrochemical avenue to blue luminescent nanocrystals from multiwalled carbon nanotubes (MWCNTs), *Chem. Phys. Lett.*, 493, **(2010)** 296–298.

26. D. Y. Pan, J. C. Zhang, Z. Li, C. Wu, X. M. Yan and M. H. Wu, Observation of pH-, solvent-, spin-, and excitation-dependent blue photoluminescence from carbon nanoparticles, *Chem. Commun.*, 46, **(2010)** 3681–3683.

27. H. Zhu, X. L. Wang, Y. L. Li, Z. J. Wang, F. Wang and X. R. Yang, Microwave synthesis of fluorescent carbon nanoparticles with electrochemiluminescence properties, *Chem. Commun.*, **(2009)**, 5118–5120.

28. L. Tang, R. Ji, X. Cao, J. Lin, H. Jiang, X. Li, K.S. Teng, C.M. Luk, S. Zeng, J. Hao, and S.P. Lau, Deep Ultraviolet Photoluminescence of Water-Soluble Self-Passivated Graphene Quantum Dots, *ACS Nano* 6 **(2012)** 5102.

29. X. Yan, X. Cui, B. Li and L. Li, Large, Solution-Processable Graphene Quantum Dots as Light Absorbers for Photovoltaics, *Nano Lett.* 10 **(2010)** 1869.

30. JJ Lu, YJ Cai and J Ding, Curcumin induces DNA damage and caffeine-insensitive cell cycle arrest in colorectal carcinoma HCT116 cells, *Nat. Nanotechnol*. 6 **(2011)** 247.

31. H. Sun, L. Wu, W. Wei and X. Qu, Recent advances in graphene quantum dots for sensing, Elsevier, *Materials Today* Volume 16, Number 11, November **2013**.

32. C. Neumann, C. Volk, S. Engels and C. Stampfer, Graphene-based charge sensors, *Mater. Today* 13 **(2010)** 44.

33. D. Wang, L. Wang, X. Dong, Z. Shi and J. Jin, Chemically tailoring graphene oxides into fluorescent nanosheets for Fe^{3+} ion detection, *Carbon* 50 **(2012)** 2147.

34. L. Wu, J. Wang, J. Ren, W. Liab and X. Qu, Highly sensitive electro-chemiluminescent cytosensing using carbon nanodot@Ag hybrid material and graphene for dual signal amplification, *Chem. Commun*. 49 **(2013)** 5675.

35. X. Feng, N. Gan, S. Lin, T. Li, Y. Cao, F. Hu, Q. Jiang and Y. Chen, "Ratiometric electrochemiluminescent aptasensor array for antibiotic based on internal standard method and spatial-resolved technique", *Sens. Actuators* B, 226 **(2016)**, pp. 305-311.

36. D.B. Shinde and V.K. Pillai, Electrochemical Resolution of Multiple Redox Events for Graphene Quantum Dots, Angew. *Chem. Int. Ed.* 52 **(2013)** 2482.

37. H. Razmi and R. Mohammad-Rezaei, Graphene quantum dots as a new substrate for immobilization and direct electrochemistry of glucose oxidase: application to sensitive glucose determination, *Biosens. Bioelectron.* 41 **(2013)** 498.

38. L. Surbhi, T.L. Christine, Edson and S.Randall, "General principles of antimicrobial therapy", *Mayo Clinic Proceedings*, 86 (2), **(2011)** 156–167.

39. SK. Yadav, B. Agrawal, P. Chandra and RN. Goyal, In vitro chloramphenicol detection in a Haemophilus influenza model using an aptamer-polymer based electrochemical biosensor, *Biosens, Bioelectron*, 55, **(2014)** 337-342.

40. P. Ball, "Quinolone generations: Natural history or natural selection?" *Journal of Antimicrobial Chemotherapy*, Volume 46, **(2000)** pp 17–24.

41. O.Cramariuc, T.Rog, M.Javanain, L.Monticelli, A.V.Polishchuk, Ilpo. Vattulainen, Mechanism for translocation of fluoroquinolones across lipid membranes, *Biochimica et Biophysica Acta (BBA) - Biomembranes*, Volume 1818, Issue 11, **(2012)**, Pages 2563-2571.

42. J. J. Heidelbaugh, and H. Holmstrom, "The perils of prescribing fluoroquinolones", *The Journal of family practice*, 62 (4), **(2013)** 191–7. PMID 23570031.

43. V. M. D'Costa, E. Griffiths & G. D. Wright, Expanding the soil antibiotic resistome: Exploring environmental diversity, *Current Opinion in Microbiology*, 10, **(2007)** 481–489.

44. A. Alonso, P. Sánchez & J. L. Martínez, Environmental selection of antibiotic resistance genes, *Environmental Microbiology*, 3, **(2001)** 1–9.

45. L. Fotouhi, and M. Alahyari, Electrochemical Behavior and Analytical Application of Ciprofloxacin Using a Multi-walled Nanotube Composite Film-Glassy Carbon Electrode, *Colloids Surf*, B 81, **(2010)** 110−114.

46. M. Otto **(2000)** Analytische Chemie. Wiley-VCH, Weinheim.

47. H. Y. Ji, D. W. Jeong, Y. H. Kim, H. Kim, D. Sohn and H. S. Lee, Hydrophilic Interaction Liquid Chromatography−Tandem Mass Spectrometry for the Determination of Levofloxacin in Human Plasma, *J. Pharm. Biomed Anal*, 41, **(2006)** 622−627.

48. V.F. Samanidou, C.E. Demetriou & Papadoyannis, Direct determination of four fluoroquinolones, enoxacin, norfloxacin, ofloxacin, and ciprofloxacin, in pharmaceuticals and blood serum by HPLC, *I.N. Anal Bioanal Chem*, 375, **(2003)** 623. https://doi.org/10.1007/s00216-003-1749-9

49. M. I. Pascual-Reguera, G.P. Parras, and A.M. Díaz, A Single Spectroscopic Flow-through Sensing Device for Determination of Ciprofloxacin. J. *Pharm. Biomed. Anal*, 35, **(2004)** 689−695.

50. A. Navalón, O. Ballesteros, R. Blanc, and J. L. Vílchez, Determination of Ciprofloxacin in Human Urine and Serum Samples by Solid-phase Spectrofluorimetry, *Talanta*, 52, **(2000)** 845−852.

51. M. Hernández, C. Aguilar, F. Borrull and M. Calull, Determination of ciprofloxacin, enrofloxacin and flumequine in pig plasma samples by capillary isotachophoresis–capillary zone electrophoresis, *Journal of Chromatography* B, Volume 772, Issue 1, **(2002)** Pages 163-172.

52. AC. Huet, C. Charlier, SA. Tittlemier, G. Singh, S. Benrejeb and P. Delahaut, Simultaneous Determination of (Fluoro)quinolone Antibiotics in Kidney, Marine Products,

Eggs, and Muscle by Enzyme-Linked Immunosorbent Assay (ELISA), *Journal of Agricultural and Food Chemistry*, 54 (8), **(2006)** 2822-2827.

53. HW. Sun, LQ. Li & XY. Chen, Flow-injection enhanced chemiluminescence method for determination of ciprofloxacin in pharmaceutical preparations and biological fluids, *Anal Bioanal Chem* **(2006)** 384: 1314.
54. P. Yan, L. Xu, D. Jiang, H. Li, J. Xia, Q. Zhang, M. Hua and H. Li, Photoelectrochemical monitoring of ciprofloxacin based on metallic Bi self-doping BiOBr nanocomposites, *Electrochimica Acta*, Volume 259, **(2018)** Pages 873-881.
55. X. Zhang, Y. Wei and Y. Ding, Electrocatalytic oxidation and voltammetric determination of ciprofloxacin employing poly(alizarin red)/graphene composite film in the presence of ascorbic acid, uric acid and dopamine, *Analytica Chimica Acta*, Volume 835, **(2014)**, Pages 29-36.
56. AA. Ensafi, AR. Allafchian and R. Mohammadzadeh, Characterization of MgFe2O4 Nanoparticles as a Novel Electrochemical Sensor: Application for the Voltammetric Determination of Ciprofloxacin, *Anal Sci*, 28(7), **(2012)** 705-10.
57. N. Diab, I. Abu-Shqair, R. Salim and M. Al-Subu, The Behavior of Ciprofloxacin at a DNA Modified Glassy Carbon Electrodes, *Int. J. Electrochem*. Sci., 9 **(2014)** 1771 - 1783.
58. P. Gayen, BP. Chaplin, Selective Electrochemical detection of ciprofloxacin with a porous nafion/multiwalled carbon nanotube composite film electrode, *ACS Appl Mater Interfaces.*, **(2016)**, 8(3):1615-26.
59. K.S.V. Santhanam, S. Kandlikar, M. Valentina and Y. Yang, Electrochemical process for producing graphene, graphene oxide, metal composites and coated substrates, *US Patent*

2016/0017502A1 **(2016)**; WO2015US40615 2015071.5; US9,840,782B2, December 12, 2017.

60. D.A. Skoog, F.J. Holler and S.R. Crouch, Principles of instrumental analysis, sixth edition, *J. Chem. Educ*, **(2006)**.
61. Z. Protich, K. S. V. Santhanam, A. Jaikumar, S. G. Kandlikar and P. Wong, Electrochemical Deposition of Copper in Graphene Quantum Dot Bath: Pool Boiling Enhancement, *Journal of The Electrochemical Society*, 163 (6), **(2016),** E166-E172.
62. A.J. Bard and L.R. Faulkner, Electrochemical methods - Fundamentals and Applications, second edition, *John Wiley and sons*, **(2012)**.
63. K. Aoki, J. Osteryoung and R.A. Osteryoung, Differential normal pulse voltammetry-theory, *J. Electroanal. Chem. Interfacial Electrochem.*, 110, **(1980)** 1-18.
64. D. Merlia , A. Profumo and C. Dossib, J. Pharmaceutical Analysis 2 (6), 450 (2012).
65. N.N.N. Ahamed, W. Fan, M. Schrlau and K.S.V. Santhanam, A New Graphene Quantum Dot Sensor for Estimating an Antibiotic Concentration, *MRS Advances Nanomaterials*, 3 (15), 825 **(2018)**, DOI:10.1557/adv.2018.29.
66. B. Bhongade, S. Talath and S. Dhaneswar, A Validated Method for the Quantitation of Ciprofloxacin Hydrochloride Using Diffuse Reflectance Infrared Fourier Transform Spectroscopy, *Int. J. Spectroscopy*, 294612 **(2014)**.